Model-based estimation of arterial diameter from x-ray angiograms

by

Raymond C. Chan

Submitted to the Department of Electrical Engineering and Computer Science
in partial fulfillment of the requirements for the degree of

Master of Science in Electrical Engineering

at the

MASSACHUSETTS INSTITUTE OF TECHNOLOGY

February 1996

Author ....
Department of Electrical Engineering and Computer Science
Jan 19, 1996

Certified by ....
Robert S. Lees
Professor of Health Sciences and Technology
Thesis Supervisor

Certified by ....
W. Clem Karl
Research Affiliate, Laboratory for Information and Decision Systems
Thesis Supervisor

Accepted by ....
Frederic R. Morgenthaler
Chairman, Departmental Committee on Graduate Theses

Model-based estimation of arterial diameter from x-ray angiograms

by

Raymond C. Chan

Submitted to the Department of Electrical Engineering and Computer Science
on Jan 19, 1996, in partial fulfillment of the
requirements for the degree of
Master of Science in Electrical Engineering

Abstract

X-ray coronary angiography is a widely used imaging technique for visualizing the presence of coronary artery disease (CAD). The measurement of arterial diameter from these images reflects disease burden, and provides an assessment of treatment benefit from existing and experimental therapies. Unfortunately, existing derivative-based and model-based measurement methods provide poor estimates for small vessel diameters — precisely the range that is associated with the presence of clinically significant stenoses.

We have found that because of blurring and noise, the apparent widths of small vessels in angiographic images contain little information about the real diameters, leading to poor estimation performance by existing techniques. Information about vessel diameter does remain available in the intensity height, but this has not, until now, been exploited to improve diameter estimation. The use of intensity information is complicated by a variable, non-linear relationship between intensity and vessel diameter. Separate x-ray calibration procedures might be used to experimentally determine crude approximations to this non-linear relationship. However to date, such procedures are clinically impractical to perform. To overcome this limitation, we have used a more accurate description of x-ray imaging function to pose this problem within a model-based estimation framework. With this approach, we can estimate the unknown imaging model parameters directly from an angiographic image, without the need for additional x-ray experiments. The intensity relationship thus determined forms the basis for a novel model-based estimator which uses the combined intensity and width information within an angiogram to measure arterial diameter.

We have used computer simulation to analyze the performance and sensitivity of this method to imaging noise, blurring, angiographic backgrounds, imaging system operating points and estimation initial conditions. These simulations have shown that this approach is robust to variations in each of the conditions studied. Finally we have compared the diameter estimates from our technique against those from existing methods, using simulated arterial vessel images and real x-ray images of vessel phantoms. Our results suggest that diameter estimation using our new approach is significantly improved over estimation using the current forms of diameter measurement.

Thesis Supervisor: Robert S. Lees
Title: Professor of Health Sciences and Technology

Thesis Supervisor: W. Clem Karl
Title: Research Affiliate, Laboratory for Information and Decision Systems

Acknowledgments

Concede mihi, misericors Deus,
quae tibi sunt placita,
ardenter concupiscere,
prudenter investigare,
veraciter agnoscere,
et perfecte adimplere,
ad laudem et gloriam nominis tui.

— St. Thomas Aquinas

This work would not have been possible without the guidance and support of my thesis supervisors, Clem Karl and Robert Lees. Their insight, character, and enthusiasm for research have profoundly influenced my own thinking and approach to problem solving. I would like to thank Robert Dinsmore and Fred Holmvang, whose help in acquiring the x-ray images at the MGH cath labs was invaluable. Furthermore, I would like to thank the crew at the Boston Heart Foundation for making the lab a great place to work and share ideas. I would especially like to acknowledge my friends Rob Stadler, Anibal Arjona (whose supply of candy kept me going), and Sherrif Ibrahim. Finally, special thanks must go to my family, and to my fiancee, Jean Lin, for their love and encouragement.

Contents

Chapter 1

Introduction

1.1 Overview

This thesis addresses the problem of high-precision atherosclerotic lesion measurement in coronary x-ray angiograms. We shall describe a rational approach to obtaining practical, model-based diameter estimates of focal lesions from angiographic images. X-ray angiography is the current 'gold-standard' for visualizing occlusive coronary artery disease (CAD). This disease cuts off the blood supply to the heart and is the leading cause of death in the developed world. In the United States alone, it is responsible for an estimated 260,000 deaths per year. Approximately 1.5 million diagnostic procedures are performed annually in the U.S., which result in over 265,000 coronary bypass operations and 331,000 coronary balloon angioplasties [14].

The accurate analysis of coronary disease burden is essential for diagnosing whether a patient requires intervention, for deciding what form of treatment will be used, and for assessing the efficacy of antiatherosclerotic medications. Traditionally, the treatment of atherosclerosis requires either reopening the blocked artery or replacing it with another conduit which takes over normal arterial function (e.g. a bypass graft). These interventions are invasive and costly, yet they demonstrate only limited effectiveness; vein bypass grafts last on average 8–10 years, while about 30% of angioplastied lesions restenose within 6 months of therapy. The disappointing performance of these procedures, as well as the pain and suffering from a potentially fatal heart attack, have led to the increased use of drug therapy to prevent atherosclerosis. Prevention may have greater cost-effectiveness as well. Such preventative therapy can retard or even reverse the effects of atherosclerosis.

The successful evolution of an experimental therapy into a mainstream clinical treatment depends in part on drug efficacy assessments with quantitative coronary angiography (QCA). This technique aims to quantify the severity and extent of atherosclerotic lesions with a high degree of precision. Unfortunately, QCA as currently practiced, does not achieve these goals for a critical subset of coronary vessel sizes. Over the past two years, our involvement with the Quinapril Ischemic Event Trial (QUIET)[1] has provided strong incentive for lowering the high variability and bias observed in QCA diameter estimates over a range of vessel sizes. These shortcomings in measurement quality blunt the ability of this and other intervention studies to analyze the influence of treatment on arterial structure as visualized by x-ray angiography.

X-ray angiography is one of the highest resolution imaging techniques available for visualizing coronary lumen structure. It is an invasive contrast-enhanced projection imaging technique which requires contrast agent to be injected directly into the coronary circulation. This significantly increases the x-ray attenuation within the blood vessels above that of the surrounding tissue, so that the blood vessels can be visualized as bright structures over a relatively darker background. During imaging, x-rays emitted by an x-ray source are attenuated as they pass through the patient. The exiting x-rays impinge upon the face of an image intensifier that amplifies the input. This produces an intensified output image that is recorded onto 35mm ciné-film. With a ciné-film projector, the frame images are projected onto a digitizing camera which provides an image intensity matrix for quantitative analysis. The resultant angiographic image is degraded by process noise and blur which are responsible for the difficulties in obtaining accurate and reproducible arterial measurements.

QCA measures the cross-sectional arterial diameter in nonoverlapping and nonbranching segments lying parallel to the imaging plane. Under physiological perfusion pressure, arterial cross-sections are typically circular. A vessel's diameter in a given projection is an indication of its luminal patency and provides information about the degree of arterial stenosis. Other physiologically relevant measures of disease such as vessel cross-sectional area and hemodynamic resistance can be derived from the arterial diameter. The extent to which these derived parameters reflect reality is limited by the quality of the original diameter measurement. As disease progresses, lesion encroachment into the lumen reduces

---

[1] QUIET is a large atherosclerosis regression trial which is using QCA to evaluate the effects of angiotensin-converting enzyme inhibition on coronary atherosclerosis.

arterial diameter and cross-sectional area, and elevates hemodynamic resistance to the flow of blood to the heart muscle served by the vessel.

Angiographic studies of drug therapy or of arterial revascularization rely upon diameter-based statistical measures of efficacy. In particular, the minimum lumen diameter is often used because of its strong correlation with clinical cardiac events. Unfortunately, QCA cannot currently measure vessels that are smaller than or comparable in size to the process point spread function (typically 1.0–1.5 mm) with any great accuracy or reproducibility. This presents a problem since normal proximal vessels are on the order of 3.0 mm in diameter and CAD is a generalized disease whose symptoms begin after about a 70% reduction in local arterial diameter. A typical symptomatic patient may have several coronary stenoses that lie in this size range. Within the QUIET angiographic study data, an estimated 30% of the available segments were 1.0 mm or smaller, while about 50% were 1.5 mm or smaller. These figures emphasize the need for improved dimension estimates in small caliber vessels.

We propose a rational, model-based, approach to the vessel measurement problem that is practical to implement and makes more efficient use of the available angiographic information than previously reported schemes. The concept of applying a model to improve diameter estimates is not new. However, existing techniques are based on simple modelling assumptions that do not significantly improve diameter measurement in small vessels. They are also impractical since they require additional calibration experiments during angiography to be used effectively. These schemes rely only on apparent vessel width to provide information about the true arterial diameter and produce estimates of unacceptible quality when measuring vessels smaller than 1.0mm in diameter.

An angiographic vessel image contains information about the true vessel diameter not only in the apparent width of the vessel intensity profile, but also in the intensity profile height. Since arterial cross-sections are usually circular in vivo, the intensity profile height, like the apparent width, is a function of the true vessel diameter. By more accurately modelling the response of the x-ray imaging chain, we can exploit this image intensity as an additional source of information to further improve diameter estimation. Measurements using this approach should demonstrate lower bias and higher reproducibility over those from existing schemes. A more accurate model of the imaging system response should also allow practical clinical implementation by eliminating the need for additional calibration experiments performed during angiography.

1.2 Thesis goals and contributions

The goals of this thesis are to:

- analyze the failure of the existing methods for QCA.
- design a practical model-based diameter estimator which performs well for small as well as for large arterial widths.

To make our goals tractable, we will consider only single, isolated vessels with circular lumen lying parallel to the imaging plane. The extension of this research for quantifying branching, overlapping, non-planar or non-circular vessel segments is an area of further investigation. This limitation in the vessels we will work with is reasonable since QCA is currently only used to quantify vessels meeting the stated criteria. We will further assume that the segment of interest has been pre-selected by an experienced angiographer and that its centerline has already been extracted by using a robust vessel centerline detector.

The immediate benefit of this work will be in providing high-precision quantitative measures of arterial diameter which in turn improves the quality of other important physiological parameters derived from this quantity. Increasing the measurement quality of quantifiable CAD information from a single projection image will enhance the diagnostic ability of the clinician dealing with atherosclerosis. Improved estimator robustness to image noise may mean that lower x-ray doses will be required for angiography, lowering the health risk due to radiation exposure faced by both the patient and clinical staff.

This work should optimize the predictive value of x-ray coronary angiograms not only for individual patients, but also for intervention studies such as QUIET. The required patient population size in these studies is proportional to the measurement error variance. Therefore, improved estimation quality can lead either to substantial cost savings due to reduced population sample size requirements, or to increased statistical power of studies over others employing the existing QCA methods. This may ultimately result in lower healthcare cost and more effective therapy of CAD.

1.3 Organization

This thesis is organized in the following manner. Chapter 2 provides the reader with background on the disease process and current methods of imaging coronary disease. Chapter 3 describes the diameter estimation problem, and analyzes the existing approaches for addressing it. In Chapter 4 we introduce an improved model of the x-ray imaging chain which we use in our development of a diameter estimator that exploits both the profile intensity and width information in an angiographic image, and that can be practically implemented in a clinical setting. We then present simulation results relating to this estimator. In these experiments, synthetic data sets are generated for use in Monte-Carlo simulations which interrogate the performance and sensitivity of this method under a variety of imaging conditions and under varying scenarios of *a priori* knowledge. Finally, we demonstrate its estimation quality by measuring arterial phantom diameters from real x-ray images. Chapter 5 concludes this thesis with a discussion of the overall work and issues for future exploration.

Chapter 2

Medical Background

2.1 Objective

The goal of this chapter is to review the medical background needed to put into perspective the research presented in this thesis. We begin with a description of the disease-induced changes in arterial structure, and then proceed with a description of the main imaging modalities for visualizing coronary disease, focusing in particular on x-ray ciné-angiography.

2.2 Occlusive coronary disease

An understanding of the underlying disease process is necessary for planning a rational approach to the quantification of coronary atherosclerosis. The coronary circulation may be divided into the left and right coronary trees which begin at the aorta and branch out to encircle the heart. These arteries supply the heart muscle (myocardium) with oxygen- and nutrient-rich blood necessary for normal heart function. Healthy vessels are on the order of 4.0mm and smaller, with circular lumen cross-sections and diameters along their lengths that are approximately constant or linearly tapering towards the distal end.

The pathogenesis of coronary disease is not well understood in part because the disease remains clinically silent until late in its course. It is hypothesized that arterial injury (due to hypercholesterolemia, hypertension, smoking, diabetes and so on) initiates a pathological process which eventually leads to the formation of fibrofatty and fibrous lesions that impinge on the vessel lumen.

From a biochemical standpoint, vessel wall injury leads to increased trapping of lipoprotein within the artery and specific adhesive glycoproteins appear on the surfaces of the endothelial cells. Monocytes and T lymphocytes attach to the adhesion proteins and migrate between the endothelial cells under the influence of growth regulatory molecules and chemoattractants released by the altered endothelium, the adherent leukocytes and the underlying smooth muscle cells. As the migrating cells penetrate the endothelium, the monocytes become macrophages, accumulate lipids, become foam cells and, with the accompanying lymphocytes, form a fatty streak (the earliest recognizable lesion of atherosclerosis). Continued cell influx and proliferation lead to the more advanced lesions, which are more fibrous in character, and ultimately to the fibrous plaque. Each stage of lesion formation is potentially reversible if the injurious agents are removed, or if protective factors intervene to reverse the inflammatory and fibroproliferative processes.

From an anatomical perspective, the growing lesion threatens arterial patency, but the lytic enzymes activated by the process produce a structural response which preserves the normal lumen area. Enzymatic destruction of its elastic fibers allows the artery to dilate and increase its lumen diameter above normal at the lesion site. After the lesion exceeds about 40% of the area inside the internal elastic lamina, this compensatory mechanism is overwhelmed [3]. Plaque intrusion into the vessel lumen results, compromising the vessel's ability to provide adequate blood flow to the dependent myocardium. Clinical symptoms begin to appear after about a 70% reduction in normal lumen diameter. The symptom-producing stenoses are often on the order of 1.0mm or smaller — precisely the size range in which existing QCA methods are unsatisfactory. Further CAD progression can produce plaque rupture or severely constricted (high-grade) stenoses. In the absence of treatment, total occlusion can occur, often leading to myocardial infarction or sudden cardiac death.

Because the rate of progression of CAD is variable even in a single vessel, a given vessel segment may have sections that are normal, that are dilated by early disease, or that show constriction because of more advanced disease. The diameters along the length of a diseased vessel length therefore do not taper linearly as is the case for a healthy artery. Vessel walls in the diseased artery may also appear rough because of focal differences in rate of disease progression, in marked contrast to normal arterial walls which have smooth boundaries. As progression continues, lesions grow to encircle the artery and also spread out along the length of the vessel so that a greater portion of the segment becomes abnormal. The normally round shape of the lumen cross-section may be altered by the presence of mural lesions; a lesion occupying less than 50% of the wall cross-sectional area can produce an eccentric lumen which often returns to a round, concentric form after it grows to occupy greater than 75% of the arterial wall area [3]. Lesions are biochemically more active than healthy tissue, exhibiting marked cholesterol accumulation, smooth muscle cell proliferation, matrix synthesis, and calcification. The tissue composition in the diseased arterial wall is therefore strikingly different from that in the healthy wall; the diseased wall will not only contain smooth muscle and endothelial cells, but also a high concentration of macrophages, foam cells, lymphocytes, lipids, calcium and connective tissue.

The differences we have outlined in both arterial structure and biochemical function between the healthy and diseased vessel wall provide quantifiable indices of disease progression. Currently, our ability to image, quantify and interpret parameters based on arterial lumen anatomy outweighs our ability to interrogate those based on the biochemical function of the vessel wall. For this reason, clinical diagnoses and studies of experimental therapies for CAD rely largely upon accurate and reproducible measurement of vascular structure.

2.3 Imaging coronary disease

2.3.1 Nuclear imaging

Nuclear imaging using intravenously injected radio-labelled LDL (Low Density Lipoprotein) can be used to visualize the biochemical activity of the arterial wall. Arterial plaques have a higher rate of LDL uptake than normal tissue and accumulate a greater concentration of radionuclide. Areas of bright intensity within the nuclear image indicate the presence of coronary atherosclerosis. This form of functional imaging is inexpensive, minimally invasive, and is sensitive to earlier stages of coronary disease than other methods. However, the intrinsic spatial resolution of nuclear imaging is poor, limiting its usefulness for diagnostic imaging based on anatomical structure.

2.3.2 Magnetic resonance imaging

Magnetic resonance (MR) imaging is a non-invasive method which visualizes the blood-filled lumen and the vessel wall. Motion artifacts from the patient's heartbeat and respiratory movement complicate MR imaging. Moreover, the complex three-dimensional structure and motion of the coronary tree preclude consistent acquisitions in a fixed imaging plane. The available spatial resolution is a function of scan-time and magnetic field strength. Longer scan-times increase motion artifacts while higher field strengths lead to problems with field homogeneity. The spatial resolution of MR in coronary artery imaging is relatively low (greater than 1.0mm per pixel), making MR angiography a poor choice for quantifying anatomical structure.

2.3.3 Intravascular ultrasound

Intravascular ultrasound (IVUS) requires coronary artery catheterization. An ultrasound probe passed into the vessel lumen provides image slices through the arterial cross-section. This technique provides high spatial resolution and limited information about tissue composition. However, the probe size and relative rigidity prevent interrogation of narrow lumens and have the potential to injure the vessel endothelium (which by itself may initiate new lesion formation). IVUS is a promising approach to coronary imaging, but it is relatively new. Further validation must be performed on IVUS before it becomes a generally useful diagnostic tool.

2.3.4 X-ray angiography

Film-based or ciné-angiography using x-ray projection imaging is the 'gold standard' for imaging CAD. This form of coronary artery imaging is well established and is the most widely used tool for assessing atherosclerotic changes in coronary anatomy. It is invasive and insensitive to disease processes that do not affect luminal patency. Yet, x-ray angiography is one of the best modalities for high-resolution imaging of occlusive CAD, since it is well suited to clinical diagnoses which depend on arterial narrowing. The high dynamic range and resolution of film combined with contrast-enhancement using a dye injection provides images with good spatial resolution and signal-to-noise for large- and medium-sized opacified arteries (relative to the diameter of the imaging system point spread function). Film-based recording also allows the arterial image to be optically magnified for analysis of fine structure

An alternative to conventional film-based recording is digital subtraction angiography (DSA) in which digital images are acquired directly from the image intensifier. A pre-injection thorax image is subtracted from subsequent post-injection images to increase the SNR and remove structured noise from background tissue such as bone, liver or lungs. Since subtraction improves SNR, this technique requires a lower concentration of contrast medium. The latter can be introduced either by local injection at time of catheterization, as in conventional x-ray angiography, or by intravenous injection into an arm vein, which is less invasive. Accurate registration of pre- and post-injection images may be hampered by motion effects, but it is usually quite adequate for visualizing the arteries without background clutter. The entire thorax field of view is digitized into a 512×512 matrix using 8-bit quantization, providing lower spatial resolution than ciné-film images. Largely because of its low resolution, DSA is rarely used for coronary angiography.

2.4 X-ray projection imaging

The x-ray attenuation coefficients of the arterial wall and the blood within the lumen are similar to those of the surrounding soft tissue. This means that the coronary tree cannot be visualized by x-ray without first injecting contrast medium into the coronary circulation by catheterization. The invasive nature of cardiac angiography, in addition to human exposure to x-rays and the uncertain health of the catheterized patients, contributes to the intense time-pressure constraints of this procedure.

During catheterization, a cardiac catheter is inserted through an incision in the femoral or brachial artery and is fed through the arterial system into the left or right coronary ostium. X-ray opaque contrast medium is injected into the left or right coronary artery during ciné x-ray exposure to produce a projection image of the opacified arterial tree which is recorded on 35mm film at a typical rate of 30 frames per second. Figure 2-1 shows an example ciné-film frame and several typical angiographic sub-images (these are magnified and cropped regions of interest within an angiographic frame).

The contrast material is injected at a steady rate with sufficient pressure to ensure a high dye concentration with uniform distribution throughout the blood-filled lumen. The injection is typically sustained over three cardiac cycles at any given projection angle. The projection angulation used in single-plane angiography is chosen to ensure that the artery of interest lies parallel to the image acquisition plane, with minimal or no vessel overlap. Multiple simultaneous projections requiring several image-intensifiers and x-ray sources can be used in cases where 3D reconstructions of the coronary lumen structure are desired.

X-ray angiograms, whether from single- or multi-plane ciné-angiography or from DSA, are degraded by process noise and blur which depend on x-ray scatter, body size, imaging

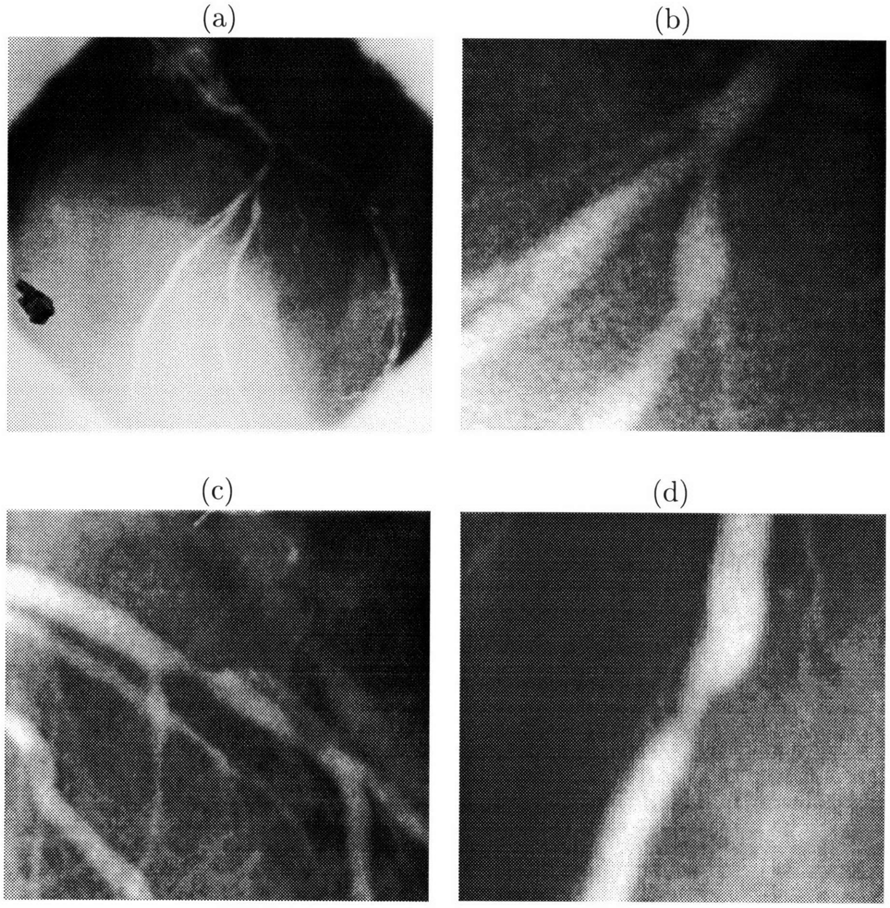

Figure 2-1: (a) Example ciné-film frame, (b)-(d) Typical angiographic subimages.

geometry, and other conditions which are variable within and between angiographic acquisitions. Despite these shortcomings, x-ray projection imaging is likely to remain one of the best modalities for visualizing the coronary arterial lumen.

The work presented in this thesis considers only single-plane ciné-angiography. The modification of our research for application in DSA or multi-plane coronary angiography is straightforward, and will be left as a subject for further study.

Chapter 3

The Diameter Estimation Problem

3.1 Objective

The accurate measurement of arterial diameter is limited by the x-ray imaging chains in current use. Blurring, in part because x-ray tubes are not ideal i.e. point sources, and noise, which can be attributed mainly to the random nature of x-ray scatter, degrade the image quality of the coronary angiograms used for vessel quantitation. These factors reduce image signal-to-noise ratio and make unacceptable the quality of small vessel measurements by current QCA methodology. This chapter describes the approach taken by existing estimators in solving the diameter estimation problem.

There are two approaches to arterial width measurement: derivative-based estimation (DBE) and model-based estimation (MBE). These estimators can operate on the image either by analyzing the available two-dimensional information or by using only one-dimensional scanlines through the intensity image. Because 2D processors offer slight improvement in measurement quality over computationally simpler (and faster) 1D processing, we will consider only estimation in image scanlines within this thesis.

For estimation in one dimension, the angiographic image of a tortuous artery is typically first sampled along scanlines perpendicular to the vessel centerline, producing a matrix of image intensities in which the arterial centerline lies along a single central column [11]. This matrix is essentially a stack of one-dimensional intensity sections through the original arterial image. Moving down these rows corresponds to marching from the proximal to the distal end of the tortuous artery in the original angiogram. One-dimensional processing of each row provides measures of arterial width as a function of centerline location.

We will begin by describing derivative-based arterial width estimation, the rationale for using this approach, and its shortcomings. We will then describe a general framework for model-based estimation in quantitative coronary angiography. Finally, we will detail the existing approach to model-based QCA and compare its performance with that of the derivative-based estimator.

3.2 Derivative-based estimation (DBE)

The measurement of vessel width using derivative-based edge-detection is the most common approach in use. Its advantages lie in its computational simplicity, speed and reliance on minimal assumptions about the image to be analyzed. The key requirement for using derivative-based vessel border detection is that the edge strength of the arterial image is strong and is dominant over the effects of noise and blurring.

In the absence of process noise and blurring, the derivatives of the arterial projection profiles will be discontinuous and infinite in magnitude at the projected edges of the arterial wall. In ideal images therefore, derivative-based edge-detection would produce perfect detection of the boundaries and diameter estimation based on this approach would be exact in addition to being fast. The availability of undegraded coronary angiograms would obviate the need for any diameter estimation method more complex than simple derivative-based edge-detection. However, such images cannot be obtained from real-world imaging systems. Real angiograms are degraded by blur and noise whose effects, when comparable in significance to the vessel edge strength, result in sub-optimal diameter estimation performance by edge-detection.

Imaging chain blur occurs when the system point spread function (p.s.f.) is non-ideal. Instead of producing an infinitesimal point or impulse in the output image in response to imaging an infinitesimal point source, the system produces an impulse response with a large region of support relative to the input. In the case of x-ray projection imaging, the non-ideal point spread function can be attributed mainly to the x-ray focal spot being of finite size (0.6–1.0mm) instead of being an ideal point source, x-ray scatter within the imaged structure, receptor unsharpness (resulting from the response and the finite size of the image intensifier phosphor and the ciné-film grains), and blurring by the projection-digitization stage of the imaging chain.

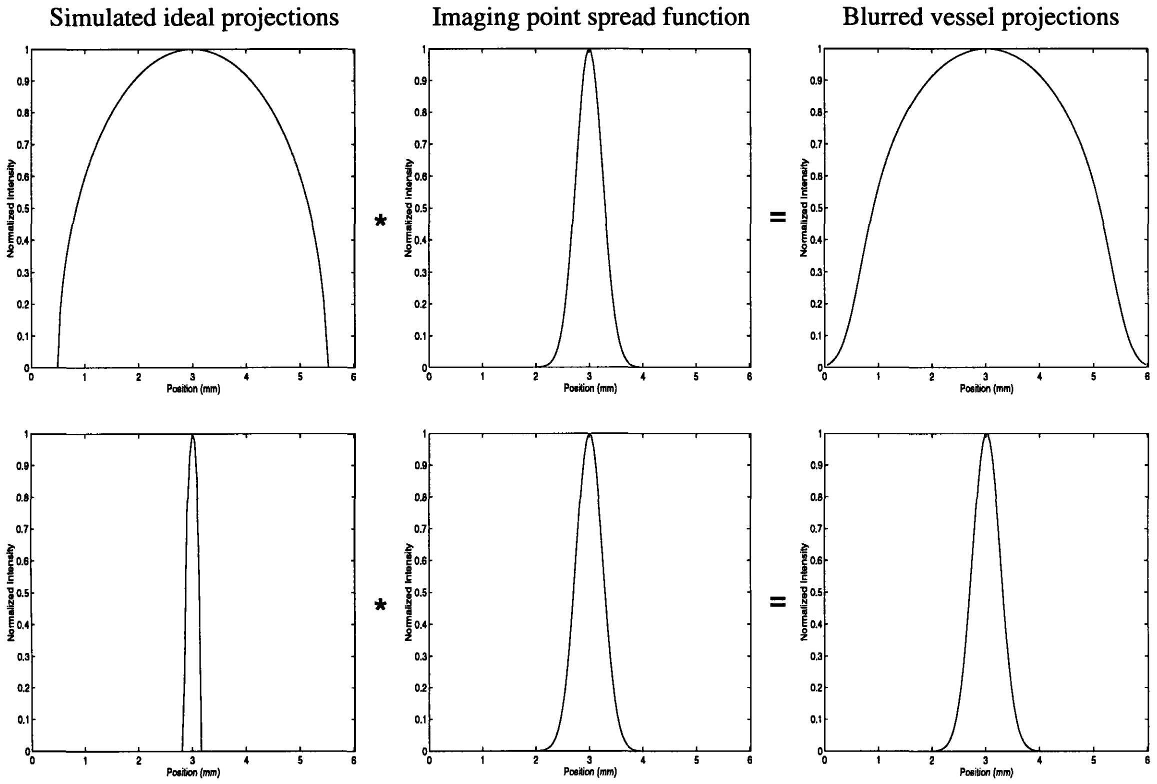

Simulated ideal projections

Imaging point spread function

Blurred vessel projections

Figure 3-1: Effect of blurring on 1D intensity scanlines through simulated arterial projections that are wide and narrow respectively, relatively to the system point spread function width.

The effect of the system point spread function on the resultant angiogram is evident when we model the imaging chain as a linear system whose output is the product of convolving the p.s.f. with the ideal projection image that one would expect in the absence of blurring. Figure 3-1 shows the effect of blurring on 1D scanlines through simulated large and small arterial projections relative to p.s.f. size. Imaging an arterial projection whose width is large relative to the p.s.f. produces a blurred arterial image whose shape and width are determined primarily by the width of the ideal vessel projection. From the standpoint of signal convolution, the p.s.f. is significantly narrower than the vessel projection and behaves like an impulse with respect to the much larger vessel "signal". Convolution of any signal with an impulse produces the original signal, explaining why the projections of large vessels appear to be unaffected by blurring. The influence of the p.s.f. on the blurred arterial image increases as the size of the ideal vessel projection decreases relative to point spread function. In the limit, as the projected vessel becomes much narrower than the p.s.f., the size and shape of blurred arterial images are determined almost entirely by the imaging chain point spread function. Once again looking at this from a convolution perspective, the ideal vessel projection is narrow and looks like an impulse relative to the p.s.f. Convolution in narrow vessels therefore produces outputs that look very similar in width to the system point spread function. This effect produces measurement bias in small vessel measurement since the edge-detected width tends toward the width of the point spread function as vessel diameter decreases.

Since blurring smooths the ideal vessel profile, it removes the edge discontinuities that would be present in the ideal profile derivative, changing the available derivative information. Diameter estimation of medium and large vessels based on the first derivative of the intensity profile alone underestimates the true vessel diameter, whereas the second derivative overestimates the width [12]. Practical edge-detectors for QCA therefore employ both the first and second derivatives so that underestimation by the first derivative can be offset by the overestimation of the second derivative. Using this approach, vessel edges are detected by locating the two largest values of the cost function:

$$C = \omega |f'| + (1 - \omega) f'' \tag{3.1}$$

where ω is an empirically derived weighting, f is the intensity cross-section, while f' and

f'' are the normalized first and second derivatives respectively. Evaluating C for each row of the resampled arterial image and selecting the two largest values per row gives the edge locations of the vessel projection. The distance between these points as a function of row position is taken to be the arterial diameter as a function of vessel centerline position.

Since the influence of imaging blur on vessel shape is dependent upon arterial width, there is no weighting of the first and second derivatives that provides accurate width estimates over the entire range of vessel sizes that need to be reliably quantified (approx. 0.4–5.0mm). The experimentally determined value of ω will be correct only for the imaging conditions under which it was found. However, these conditions are difficult to reproduce and are typically different for each angiographic session. Arterial diameter measurements, based upon fixed weighting of the intensity profile derivatives, will be sensitive to the variability of factors which include x-ray source voltages, imaging geometry, contrast dye concentration, calibration structure size, signal-to-noise conditions, background intensity levels, and thorax thickness. Optimal weights are not determined for all possible angiographic conditions. Rather, for any given angiographic system, a fixed weighting value is used (typically within the range, $0.5 \leq \omega \leq 0.8$) which gives satisfactory results over a wide range of large vessel sizes ≥ 2.0mm.

Imaging noise from random photon emission and incidence, x-ray scatter, quantum mottle, as well as electronic noise, further complicates diameter estimation. It is the presence of noise that makes the use of simple deconvolution algorithms for blur inversion difficult [8]. The effects of noise are more significant in small vessels since their projections are of lower intensity than those from large vessels. At a constant noise level, the signal-to-noise ratio (SNR) for a given arterial image will drop as the vessel of interest decreases in size. Diameter estimation becomes increasingly difficult with decreasing SNR. Random noise introduces numerous peak artifacts into the first and second derivatives of the vessel intensity profile; the magnitude of such peaks may exceed that of derivatives at the real arterial boundaries. This confuses derivative-based estimators and as a result, the estimation error variance markedly increases as a function of decreasing vessel diameter. To reduce noise sensitivity, smoothing can be performed on the noisy intensity profiles prior to estimation. However, this cannot fully eliminate noise and it further blurs the image, contributing to the measurement bias. Figure 3-2 compares edge detection performed on 1D scanlines through real angiograms of a wide vs. a relatively narrower diameter vessel (the weighting ω was 0.5).

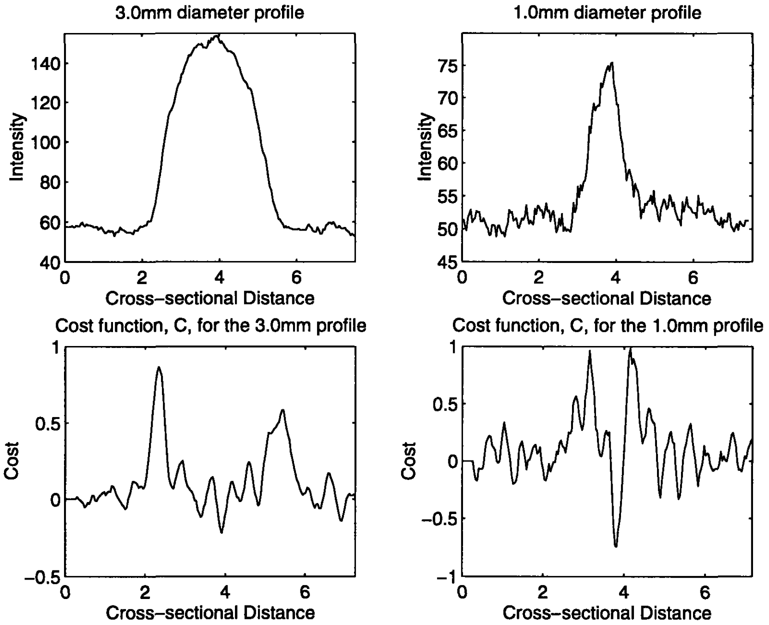

Figure 3-2: Intensity profiles through a 3.0mm and a 1.0mm diameter vessel, along with their corresponding cost functions evaluation using the equation $C = \omega|f'| + (1 - \omega)f''$, where f denotes the profile intensity and $\omega = 0.5$.

This figure shows the greater difficulty of small vessel measurement because of numerous peak artifacts in the cost function C that are comparable in magnitude to the peaks at the true vessel edges.

The combined effects of noise and blur on the quality of diameter estimates are illustrated in Figure 3-3. This figure shows the performance of a typical derivative-based QCA program when used to analyze the x-ray projection image of a vessel phantom placed over a simulated thorax (approximating the x-ray attenuation by a typical patient's chest). The vessel phantom consists of contrast-filled, cylindrical bores of known diameter, drilled into an x-ray translucent block of lucite, simulating blood vessels that have been injected with contrast dye. The mean and standard deviation of the normalized error magnitudes were calculated using the differences between the measured widths and known diameters in 100 scanlines through each of the opacified "vessels", and were then normalized by the real bore diameter. From the figure, we see that large vessels can be measured more reliably than small vessels as reflected by the lower estimation bias and variance. As diameter falls, the quality of the estimates degrade significantly; the bias and variance increase to such an extent that diameter estimates below about 1.0mm are essentially meaningless.

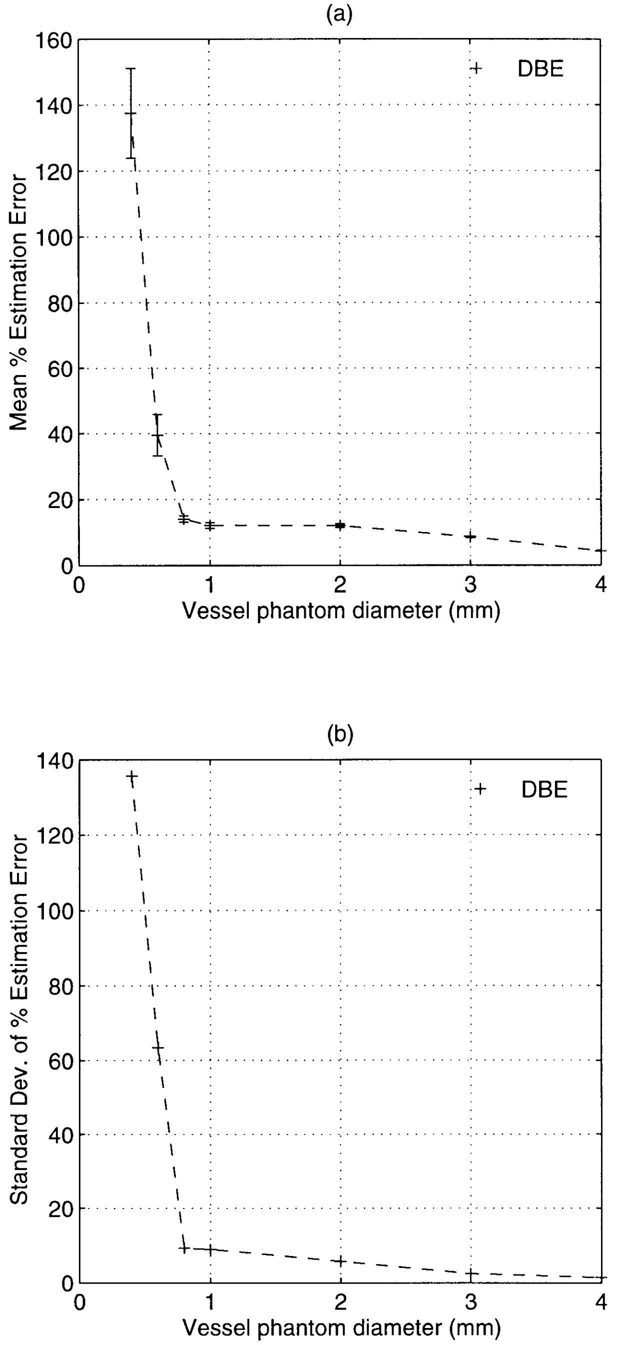

Figure 3-3: Diameter measurements using a typical derivative-based QCA system. (a) Mean normalized magnitude of the estimation error. (b) Standard deviation of the normalized error magnitude.

Noisy extracted diameters and vessel borders from individual intensity scanlines are typically smoothed by first fitting low-order polynomial regression curves through the raw data and then replacing each of the noisy values with the corresponding points on the best-fit curves, to give the final smoothed vessel borders and diameter function. Smoothing in this manner takes advantage of the known spatial continuity of the arterial walls, slightly improving estimation performance. Other methods for improving derivative-based width measurement include pre-processing the raw angiogram to reduce blur and noise by edge-preserving smoothing using a simulated annealing method [5], and multi-stage border detection, which adapts the derivative weighting according to the estimated size range in which the vessel of interest falls [17]. These extensions to conventional derivative-based estimation demonstrate limited improvement in measurement bias and variance. It is evident that the simplicity of ad hoc edge-detection in vessel measurement is its greatest limitation. As we will review in the next section, more rational and physically-based methods outperform experimentally-based, ad-hoc approaches to estimation.

3.3 A general framework for model-based estimation

Edge-detection algorithms are computationally simple, easily implemented and require little specialized background knowledge about the problem. However, the assumptions implicit in these algorithms are valid only under specific imaging conditions. A more complex, model-based, approach can be robust even under varying conditions if the model captures the salient features of the problem.

Model-based estimation uses the underlying physical principles which generate the noisy data observations to measure the parameters of interest. The more *a priori* information about the data that can be incorporated into the model-based algorithm, the smaller will be the resulting estimation error variance and bias. For this reason, a well-designed model-based scheme will outperform other empirically-based methods in most applications.

Figure 3-4 is a flow diagram of a generic model-based signal processing system which incorporates process and measurement device models to improve estimation from noisy data. Within the first stage, the process model, $a(\cdot)$, produces the quantities of interest, $\mathbf{P}_{true}$. The second stage includes a model of the ideal behavior, $C(\cdot)$, of the measurement device, and a model of the measurement degradation by unknown deterministic and ran-

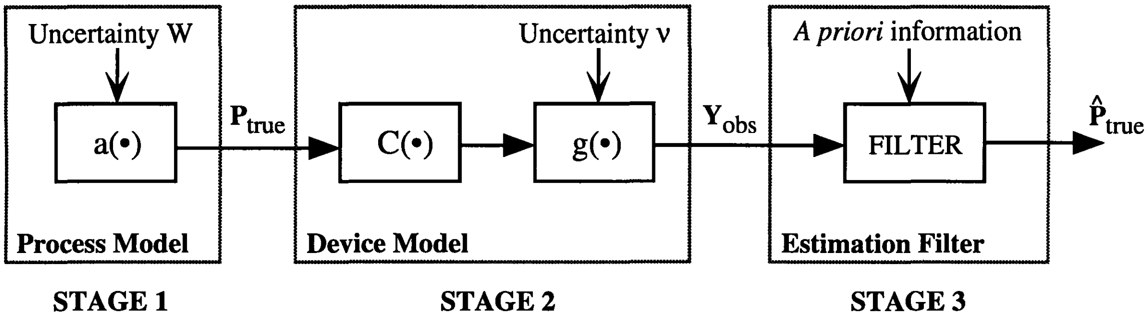

Figure 3-4: Flow diagram illustrating the function of a generic model-based signal processing system.

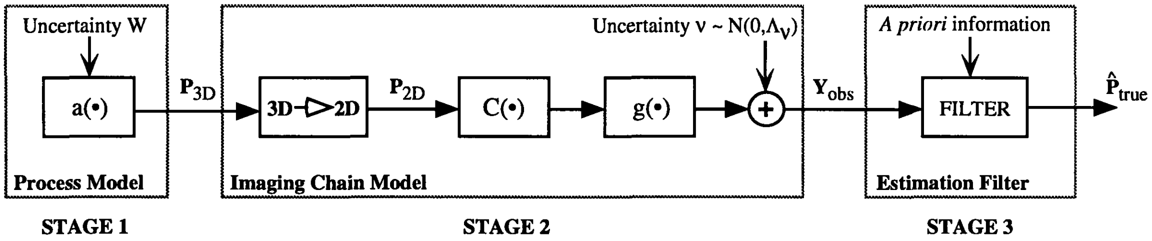

Figure 3-5: Flow diagram illustrating a general framework for model-based estimation in QCA.

dom factors which influence the device operation. The output vector, $\mathbf{Y}_{observed}$, is the noisy measurement data. The estimation filter in the final stage is designed to extract the original parameter vector, $\mathbf{P}_{true}$, from these noisy observations using prior information about the process and measurement device behavior. The details of the process and measurement models determine the criteria that the estimation filter must satisfy in order to achieve the 'optimal' estimates, $\hat{\mathbf{P}}_{estimated}$, given the modelling assumptions. Model-based estimation has been applied to quantitative coronary angiography [2, 6, 10, 16], and the general estimation framework for this is shown in the flow diagram of Figure 3-5.

Stage 1: The Process Model

The function, $a(\cdot)$, in model-based QCA represents the patient's anatomy and the CAD process which alters the normal coronary arterial structure. The variation in 'normal' anatomy between patients, as well as the intrinsic variability of CAD are captured in the process model by the uncertainty, W. The disease process itself is not directly quantifiable in QCA. Rather, it is the indirect effect that CAD has on coronary vessel structure that is measured.

The key component of the process model is a three-dimensional model of the patient's anatomy which provides a vector of quantifiable parameters, $\mathbf{P}_{3D}$, that is related to the presence and extent of coronary disease. The anatomic model is composed of two components: a vessel model, which describes the shape of the coronary arteries, and the background model, which simulates the characteristics of the non-arterial tissue surrounding the coronary arteries. The anatomic parameter vector, $\mathbf{P}_{3D}$, can therefore be subdivided into a set of arterial vessel parameters, $\mathbf{v}_{3D}$, and a set of non-arterial background parameters, $\mathbf{b}_{3D}$.

$$\mathbf{P}_{3D} = \begin{bmatrix} \mathbf{v}_{3D} \\ \mathbf{b}_{3D} \end{bmatrix} \tag{3.2}$$

We will discuss the details of the background and vessel models in the following sections.

The Background Model, $B(\cdot)$

The non-arterial tissues which appear in an angiogram include the lungs, liver, muscle, and bone. One approach to describing them would be to derive a 3D parametric model of their structure and position. However, while each of these components contributes significantly to the final image, the precise estimation of their structural detail is not necessary for QCA. Since the only parameters of interest in QCA analysis are the projected coronary vessel widths, the creation of a realistic non-arterial model in the object domain is unnecessary, and can be bypassed if the background model is developed directly in the projected image domain.

The 2D projected intensity is a continuous function of both the x-ray path through the non-arterial tissues, and their x-ray attenuation properties. Since the details of path-length and attenuation in each of the background structures are irrelevent, a low-order two-dimensional polynomial function is sufficiently accurate to predict the image background intensity. For a second-degree two dimensional polynomial,

$$B(x, y; \mathbf{b}_{2D}) = b_5 x^2 + b_4 x + b_3 xy + b_2 y + b_1 y^2 + b_0 \tag{3.3}$$

where x and y are the positions coordinates in the imaging plane and the non-arterial background parameter vector is

$$\mathbf{b}_{2D} = \begin{bmatrix} b_5 \\ \vdots \\ b_0 \end{bmatrix} \tag{3.4}$$

Stage 2: The Imaging Chain Model

Within a typical imaging chain, x-rays emitted from the source are attenuated as they pass through the body. The exiting x-rays strike the input screen of an image intensifier which releases multiple electrons for each x-ray photon. These electrons are accelerated across a voltage gradient and excite an output phosphor screen which in turn emits multiple visible-light photons for each of the incident x-ray photons. The output phosphor intensity is recorded onto 35mm film using a ciné-camera. A ciné-projector is then used to visualize the final ciné-angiogram.

The overall output from the imaging chain is a 2D intensity projection produced from a three-dimensional input in the object domain. Conceptually then, one can imagine the first block of the imaging chain to be a projection of the object domain input onto the image plane, resulting in an equivalent 2D input. Subsequent operations by the ideal imaging function and the image degradation can then be modelled entirely within the image domain, as illustrated in Stage 2 of Figure 3.5.

The image domain input is a scaled x-ray line-integral projection of the 3D object model. It is parameterized by the vector, $\mathbf{P}_{2D}$, whose components are functions of the object model parameters in $\mathbf{P}_{3D}$. It is typically impossible to recover the 3D model parameters from a single projection (particularly when the object domain model has a large number of unknown parameters). As a result, the projection parameters, $\mathbf{P}_{2D}$, are estimated instead of the object parameters, $\mathbf{P}_{3D}$, to measure CAD.

The imaging function, $C(\cdot)$, in the second block models the ideal, overall behavior of the separate imaging chain components. $C(\cdot)$ is generally derived under the following assumptions:

- the x-ray source is a mono-energetic point source,
- the imaging components do not introduce spatial distortion,
- the contrast-medium concentration injected into the vessel is uniformally distributed

throughout the lumen.

We shall return later to discuss the details of $C(\cdot)$.

The final block of the imaging chain describes the predicted behavior of image degradation. The model for the non-ideal characteristics of the imaging components includes a deterministic image degradation function, $g(\cdot)$, and an additive random noise process, $\nu(\cdot)$. The deterministic component, $g(\cdot)$, models the system point spread function which is convolved with the ideal intensity image to simulate imaging blur. A Gaussian distributed point spread function has been found to be a good approximation to the overall blurring caused by the finite focal-spot size of the x-ray source, image magnification, x-ray scatter and detector unsharpness. The random component, $\nu(\cdot)$, simulates the unpredictable behavior of photon interactions, film-grain and electronic noise. An additive, zero-mean, white Gaussian noise process with intensity Λ_ν has generally been used as a good approximation to reality [2].

Stage 3: Parameter Estimation

The general observation equation describing the recorded data at the imaging system output is

$$y(\mathbf{p};\mathbf{v}_{2D},\mathbf{b}_{2D},\sigma,\Lambda_\nu) = C\left[V(\mathbf{p};\mathbf{v}_{2D}),B(\mathbf{p};\mathbf{b}_{2D})\right] * g(\mathbf{p};\sigma) + \nu(\mathbf{p};\Lambda_\nu\delta(\mathbf{p}-\mathbf{p}')) \tag{3.5}$$

where $\mathbf{p}$ is the continuous image coordinate pair (x,y). $V(\mathbf{p};\mathbf{v}_{2D})$ is the vessel model characterized by vessel parameter vector, $\mathbf{v}_{2D}$, and $B(\mathbf{p};\mathbf{b}_{2D})$ is the background model with parameters, $\mathbf{b}_{2D}$. $g(\mathbf{p};\sigma)$ is a two-dimensional Gaussian point spread function whose spreading effect is characterized by σ. $\nu(\mathbf{p};\Lambda_\nu\delta(\mathbf{p}-\mathbf{p}'))$ is a zero-mean, white Gaussian noise process with an autocorrelation function of $E(\nu(\mathbf{p})\nu(\mathbf{p}')) = \Lambda_\nu\delta(\mathbf{p}-\mathbf{p}')$.

Parameter estimation in the presence of white Gaussian noise is a well-known problem whose solution we shall very briefly review. We combine the unknown deterministic parameters into a single parameter vector, $\mathbf{a}$, and let f_0 represent the deterministic component of the observations y to get

$$y(\mathbf{p};\mathbf{a}) = f_0(\mathbf{p},\mathbf{a}) + \nu(\mathbf{p},\Lambda_\nu\delta(\mathbf{p}-\mathbf{p}')) \tag{3.6}$$

The conditional probability distribution of these observations, given the parameters $\mathbf{a}$, is a Gaussian with a mean of $f_0(\mathbf{p}, \mathbf{a})$ and a variance of Λ_ν

$$p_{y|\mathbf{a}}(y|\mathbf{a}) \sim N(f_0(\mathbf{p}, \mathbf{a}), \Lambda_\nu \delta(\mathbf{p} - \mathbf{p}')) \tag{3.7}$$

For a white Gaussian noise model the maximum-likelihood estimates, $\hat{\mathbf{a}}_{ML}$, can be found by maximizing the likelihood function

$$-\frac{1}{\Lambda_\nu} \int_{\mathbf{p}} \{y(\mathbf{p}) - f_0(\mathbf{p}; \mathbf{a})\}^2 \, d\mathbf{p} \tag{3.8}$$

which is equivalent to minimizing the total square error between the noisy observation function, y, and the parametric function, f_0. This gives

$$\hat{\mathbf{a}}_{ML} = \underset{\mathbf{a}}{argmin} \int_{\mathbf{p}} \{y(\mathbf{p}) - f_0(\mathbf{p}; \mathbf{a})\}^2 \, d\mathbf{p} \tag{3.9}$$

This is a non-linear equation which cannot be solved analytically. Iterative numerical methods are required to determine the ML estimates.

So far, we have assumed that the intensity observations are continuous. In reality, the continuous angiogram is digitized prior to quantification. The observation equation in discrete form becomes

$$y[n, m; \mathbf{v}_{2D}, \mathbf{b}_{2D}, \sigma, \Lambda_\nu] = C\{V[n, m; \mathbf{v}_{2D}], B[n, m; \mathbf{b}_{2D}]\} * g[n, m; \sigma] + \nu[n, m; \Lambda_\nu I] \tag{3.10}$$

where I is the identity matrix and [n,m] are the discrete column and row coordinates of the digitized image. The integral within the total square error criterion of equation 3.9 becomes a summation over the image sample coordinates $\mathbf{p} = [n, m]$,

$$\hat{\mathbf{a}}_{ML} = \underset{\mathbf{a}}{argmin} \sum_{\mathbf{p}} \{y[\mathbf{p}] - f_0[\mathbf{p}; \mathbf{a}]\}^2 \tag{3.11}$$

This two-dimensional estimation is further broken into multiple 1D estimation steps. The digitized projection can be considered to be a stack of one-dimensional projections of consecutive, finite-width, thorax slices (from this perspective, the continuous angiogram is a stack of an infinite number of consecutive slices with infinitesimal width). For a digitized image whose central column is aligned with the arterial centerline, the 1D observation equation describing the ith row is

$$y_i[n; \mathbf{v}_i, \mathbf{b}_i, \sigma, \Lambda_\nu] = C_i\left\{V_i[n; \mathbf{v}_i], B_i[n; \mathbf{b}_i]\right\} * g[n; \sigma] + \nu[n; \Lambda_\nu] \tag{3.12}$$

where n is the column position across the 1D intensity profile, and $\mathbf{v}_i$ and $\mathbf{b}_i$ respectively represent the 1D vessel and background profile parameters. Blurring confined to one-dimension in the 1D observation model has been found to be an adequate approximation to the full two-dimensional blurring [9]. The vessel and background parameters in the ith row are extracted by minimizing the total square error between the parametric profile model, $f_0[n; \mathbf{a}_i]$ and the noisy intensity data, $y[n]$, so that

$$\hat{\mathbf{a}}_{ML_i} = \underset{\mathbf{a}_i}{argmin} \sum_n \left\{y_i[n] - f_{0_i}[n; \mathbf{a}_i]\right\}^2 \tag{3.13}$$

Proceeding in this manner through successive rows of a digitized image, we obtain information about vessel evolution and background intensity behavior as a function of the vessel length.

3.4 Width-dependent model-based estimation (W-MBE)

For reasons to be explained in the following section, we will refer to parameter estimation using the existing approach to model-based QCA as width-dependent model-based estimation (W-MBE). Recall that in the general estimation framework, the 1D observation equation is

$$y_i[n; \mathbf{v}_i, \mathbf{b}_i, \sigma, \Lambda_\nu] = C_i\left\{V_i[n; \mathbf{v}_i], B_i[n; \mathbf{b}_i]\right\} * g[n; \sigma] + \nu[n; \Lambda_\nu] \tag{3.14}$$

where the background, $B[n; \mathbf{b}_i]$, blurring, $g[n; \sigma]$, and noise model, $\nu[n; \Lambda_\nu]$, are as described earlier. The details of the vessel model, $V[n; \mathbf{v}_i]$, and the ideal imaging chain function, $C\{\cdot\}$, were lacking previously, and are presented now for this particular estimation approach.

3.4.1 The vessel model, $V\{\cdot\}$

The vessel segment is represented by a continuous generalized cylinder (GC), whose cross-sections are elliptic [10, 6] (Figure 3-6). GC shape is characterized by the vessel parameter

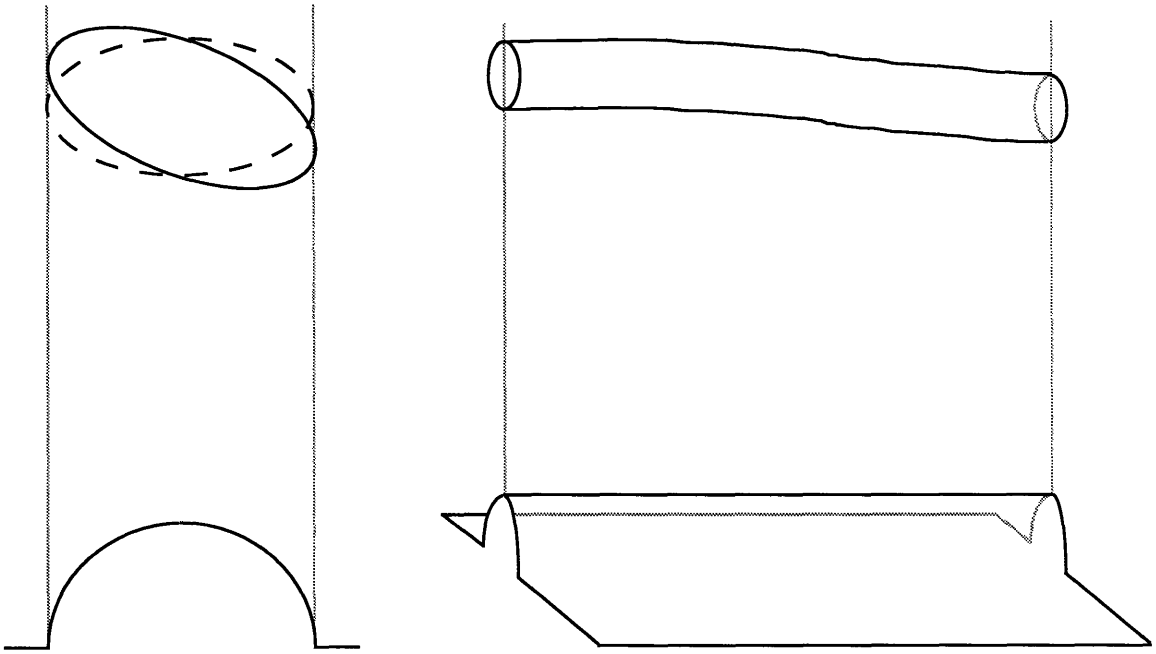

(a)

(b)

Figure 3-6: Generalized cylinder (GC) model for a coronary vessel segment. (a) 2D cross-section of this vessel model and corresponding 1D projection. (b) 2D intensity map corresponding to the projection of the 3D GC vessel model.

vector, $\mathbf{v}_{3D}$, which varies slowly and continuously as a function of axial position along the cylinder. These parameters specify, in three-dimensions, the coordinates of the central axis and the structure of the GC cross-sections.

For projection imaging and digitization, in the xy plane, of a GC axially aligned along the y-axis, the shape of the ith two-dimensional slice perpendicular to imaging plane (parallel to the z-axis) is described by

$$\frac{\{[z - c_{z_i}]\cos\theta_i + [x - c_{x_i}]\sin\theta_i\}^2}{a_i^2} - \frac{\{[z - c_{z_i}]\sin\theta_i - [x - c_{x_i}]\cos\theta_i\}^2}{b_i^2} = 1 \tag{3.15}$$

where a_i and b_i are the major and minor axes of the ith elliptical section, θ_i is its angle of rotation, and (c_{x_i}, c_{z_i}) specify the center position in the xz plane. The parameter vector characterizing the discrete model is

$$\mathbf{v}_{3D_i} = \begin{bmatrix} a_i \\ b_i \\ \theta_i \\ c_{x_i} \\ c_{z_i} \end{bmatrix} \tag{3.16}$$

where i is the slice position along the GC axis. The line-integral projection of the ith slice describes the x-ray pathlength for each point through the vessel cross-section. This is the vessel model, $V_i[n;\mathbf{v}_i]$, that is used in this estimation approach.

$$V_i[n;\mathbf{v}_i] = \begin{cases} \eta_i r_i \sqrt{1 - \frac{1}{{r_i}^2}(n - c_{n_i})^2} & \text{, if } |n - c_{n_i}| \leq r \\ 0 & \text{, otherwise} \end{cases} \tag{3.17}$$

where,

$$\mathbf{v}_i = \begin{bmatrix} \eta_i \\ r_i \\ c_{n_i} \end{bmatrix} \tag{3.18}$$

are the projected vessel parameters and n represents the discrete x-axis position along the projection profile. In these equations, $r_i = \sqrt{b_i^2 \cos^2\theta_i + a_i^2 \sin^2\theta_i}$, which is half the projected width of the vessel cross-section. The 3D vessel model parameters a_i, b_i, and θ_i which described the object domain vessel shape cannot be recovered from the projection. The scaling parameter $\eta_i = 2a_i b_i/{r_i}^2$, and the product $\eta_i r_i$ is the maximum x-ray pathlength through the ith vessel slice.

3.4.2 The ideal imaging function, $C\{\cdot\}$

X-ray attenuation by a semi-opaque medium is governed by the Lambert-Beer Law [19]. For mono-energetic x-ray photons, an input intensity, I_o, propagating through a distance, d, of homogeneous material will produce an output intensity, I, of

$$I = I_o e^{-\mu d} \tag{3.19}$$

μ is the attenuation coefficient of the medium, which is dependent on the x-ray beam energy and the material properties. The overall behavior of the image intensifier, ciné-film and projector components is assumed to be log-linear in this model, which results in an ideal imaging function of [9]

$$C = -k' \ln \frac{I}{I_o} = \mu k' d \tag{3.20}$$

In this equation, k' is an unknown system gain, and d is the x-ray distance through the attenuating medium. For the case of imaging a vessel in free space (i.e. a non x-ray attenuating medium), μ is the attenuation coefficient of the contrast dye within the vessel lumen, and $d = V(\cdot)$, the vessel model presented earlier. For the case of imaging non-arterial anatomy, no contrast medium is present. The image domain coefficients of the background model, $B(\cdot)$, already capture the intrinsic attenuation by the non-arterial tissue, while the unknown gain, k, can be absorbed into the model by appropriate scaling of its coefficients. Thus, for imaging arterial and non-arterial structures together, the ith ideal scanline predicted by the imaging function is

$$C_i[n; \mathbf{v}_i, \mathbf{b}_i] = \mu k' V_i(n; \mathbf{v}_i) + B_i(n; \mathbf{b}_i) = k V_i(n; \mathbf{v}_i) + B_i(n; \mathbf{b}_i) \tag{3.21}$$

which shows a linear dependence of the ideal intensity profile on the image domain input.

3.4.3 Parameter estimation using W-MBE

The observation equation for W-MBE estimation is

$$y_i[n; \alpha_i, r_i, c_{n_i}, \mathbf{b}_i, \sigma, \Lambda_\nu] = \left\{ \alpha_i r_i \sqrt{1 - \frac{1}{r_i^2}(n - c_{n_i})^2} + B_i[n; \mathbf{b}_i] \right\} * g[n; \sigma] + \nu[n; \Lambda_\nu] \tag{3.22}$$

where $\alpha_i = k\eta_i$, and the other parameters are as previously defined. From this equation, it can be shown that the object domain parameters $[a_i \; b_i \; \theta_i \; c_{z_i}]$ of the ith elliptic cross-section are unobtainable from the projection. The parameter vector, $[\alpha_i \; r_i \; c_{n_i}]$, of the projected vessel is the only arterial information that can be recovered.

From the standpoint of quantifying coronary disease, only the vessel diameter, $2r_i$, is physiologically relevant. The other parameters in the observation equation are so-called 'nuisance' parameters which by themselves are uninteresting, but are important to accurate diameter measurement. If these parameters could be found *a priori*, the problem of extracting r_i from the data would be greatly simplified. However, these parameters are generally not known, and need to be jointly estimated with the arterial width. The estimation of these nuisance parameters along with the width parameter is difficult in small vessels due to degradation by blurring and noise, and results in high error variance and bias in the diameter estimates.

The effect of each of the modelling parameters on the predicted projection profile is shown in Figure 3-7. The scaling, α_i, affects only the profile height while the width parameter, r_i, affects both the width and the height of the projection. Parameter c_{n_i} specifies the center position of the vessel component of the thorax projection. The background coefficients in $\mathbf{b}_i$ determine the shape of the background intensity in the output contributed by non-arterial tissue. The blur parameter, σ, controls the spreading of the ideal profile by the Gaussian point spread function and the noise variance, Λ_ν, affects the observed noise intensity.

The blurring parameter, σ, is separately and experimentally determined at each angiographic procedure [1] for use in W-MBE. Maximum-likelihood estimates of the remaining parameters along the length of the vessel are found via non-linear least squares estimation in each scanline through the thorax projection. That is, for $\mathbf{a}_i = [\alpha_i \; r_i \; c_{n_i} \; \mathbf{b}_i]^T$, and $f_{0_i}[n; \mathbf{a}_i, \sigma] = C_i[n; \mathbf{a}_i] * g[n; \sigma]$,

$$\hat{\mathbf{a}}_{ML_i} = \underset{\mathbf{a}_i}{argmin} \sum_n \{y_i[n] - f_{0_i}[n; \mathbf{a}_i, \sigma]\}^2 \tag{3.23}$$

Iterative numerical methods for function minimization are used to solve this equation. The parameters associated with the background and the vessel can be accurately obtained using joint estimation, since the intensity characteristics of the vessel and background intensity projections are different; the non-arterial structures, being orders of magnitude larger in size than the coronary arteries, produce intensity variations in the background projection that are smooth and slow relative to the rapid intensity fluctuations associated with vessel projections.

The estimation procedure is initialized using a constant background intensity which approximates the DC level of the background observations, a crude derivative-based estimate of vessel width r_i (from which an initial value for α_i can be found), and a center position that matches the peak intensity location in the noisy data.

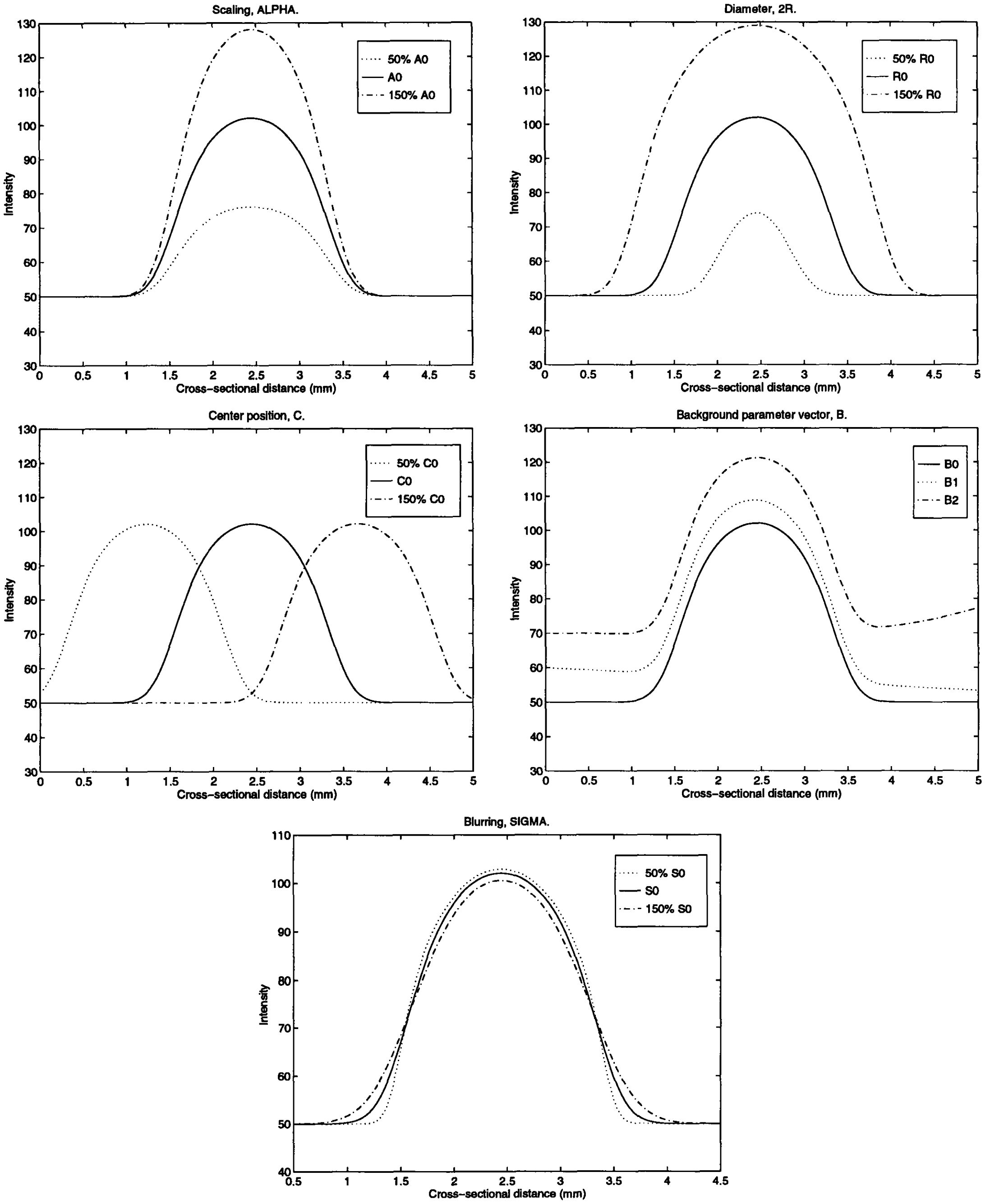

Figure 3-7: Effects of the W-MBE modelling parameters on the shape of the predicted intensity profile shape. Default vessel-related parameters were: A0 = 1, C0 = 2.4mm, R0 = 1.0mm, S0 = 0.2mm. The background parameter vectors (1D third-degree polynomial) were: B0 = [0 0 0 50], B1 = [0 0 -0.05 60] and B2 = [0.00001 -0.001 0.01 70].

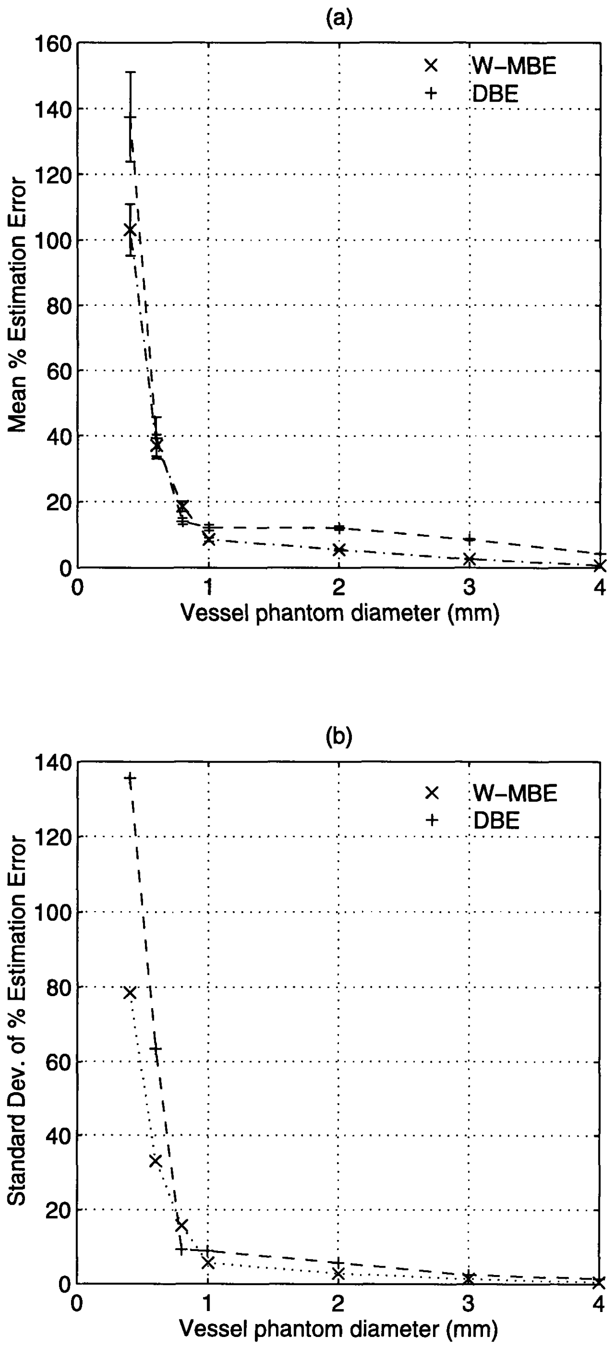

Figure 3-8: Results of diameter estimation by W-MBE versus DBE in an x-ray image of vessel phantoms with diameters ranging from 0.4mm to 4.0mm. (a) Mean normalized error magnitude. Error bars represent the size of one standard deviation in the measurements. (b) Standard deviation of the error magnitudes.

Figure 3-8 shows the results of vessel parameter estimation using this technique in an x-ray image of contrast-filled bores within a lucite block. The bores ranged in diameter from 0.4mm to 4.0mm and were filmed under typical radiographic conditions. Comparing the estimation bias and variance in W-MBE with those from derivative-based estimation (DBE), we see that the model-based approach performs better for vessels larger than 1.0mm in diameter. This improvement is not very significant in large vessels, since the measurement errors from both methods are relatively low to begin with. For vessels on the order of 1.0mm or smaller in diameter, W-MBE performance is generally better than that of DBE. However, the standard deviation of the measurements in small vessels is almost as large as the real diameters. The range of possible diameter estimates in quantifying narrow vessels is therefore too large for any meaningful interpretation of the measured diameter values. Width-dependent model-based QCA has not been popular clinically because of its impracticality of use and because the simpler DBE measurement method shows performance that is comparable to W-MBE for diameter sizes that can be reliably measured (i.e. the large vessels). The question of why the quality of these estimates is poor within the small vessel regime, despite the physical model, has so far been unresolved. We shall analyze the failure of this existing model-based approach in measuring clinically significant vessel narrowings, since this may provide insight into how quantitative coronary angiography can be improved.

3.5 An analysis of width-dependent model-based QCA

In order to study the performance of W-MBE, we first need to understand the behavior predicted by the vessel projection model as a function of arterial diameter. Let us consider the simulated shape of the intensity projection for a slice through a contrast-filled vessel embedded in homogeneous tissue. Arterial size information within the projection is contained in the profile width and in the profile height. The vessel intensity component has a height of

$$\alpha r b(r) \approx \alpha r \tag{3.24}$$

where α is the scaling parameter, r is the width parameter, and $b(r)$ is the effect of blurring on the profile height. For simplicity, we have made the approximation that $b(r) \approx 1$ so that the profile height becomes the product of the scaling, α, with the radius, r. The width of

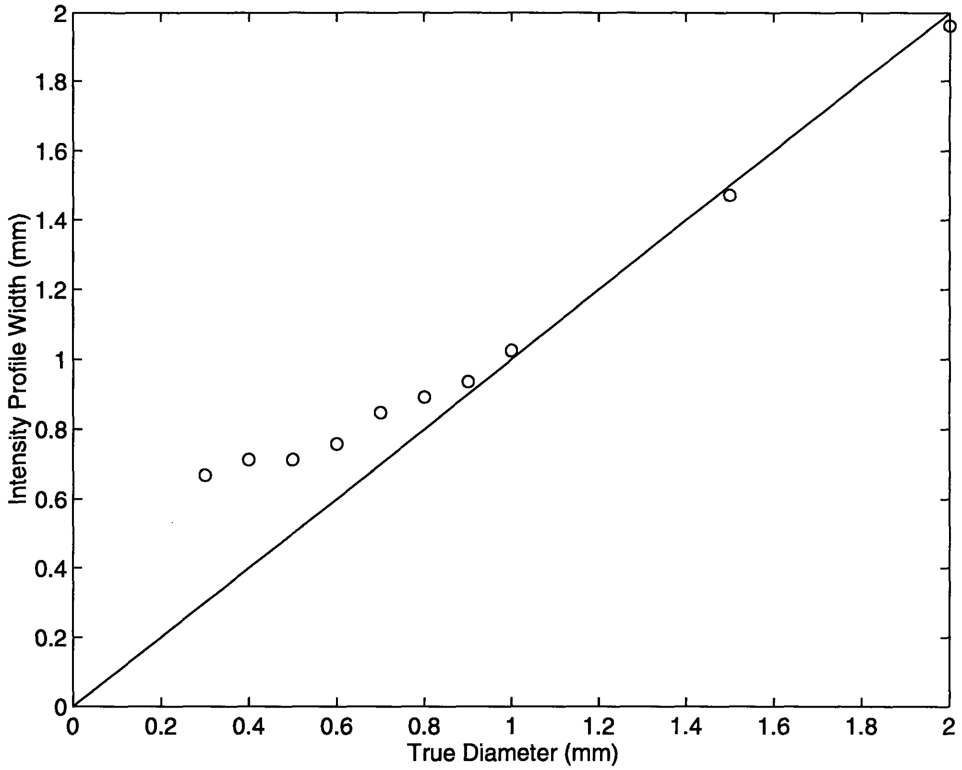

Figure 3-9: Variation in profile width as a function of vessel diameter change, when the system point spread function parameter σ = 0.2mm, and when no noise is present in the simulated profile. This figure illustrates how profile width decreases in sensitivity to the real vessel diameter, particularly for vessels sizes narrower than the point spread function.

the profile model is determined by convolution of the ideal profile with the system point spread function. Its behavior as a function of vessel diameter (in the absence of noise) is shown in Figure 3-9 (blurring parameter σ = 0.2mm). This plot shows that the width of the profile model (measured using derivative-based edge-detection) decreases in sensitivity to the vessel diameter as its size falls relative to that of the point spread function.

From Equation 3.24 and Figure 3-9, we can conclude that as vessel diameter decreases to become relatively smaller in size than the point spread function, the projection amplitude will fall approximately proportionally to diameter, while the blurred projection width will asymptotically approach a constant. Thus, in the presence of noise, the simulated projections of vessels in the small diameter regime will have very similar apparent widths and different predicted heights. This is illustrated clearly in Figure 3-10, where the noise-corrupted profile models are shown for the projected cross-sections through a 1.0mm and

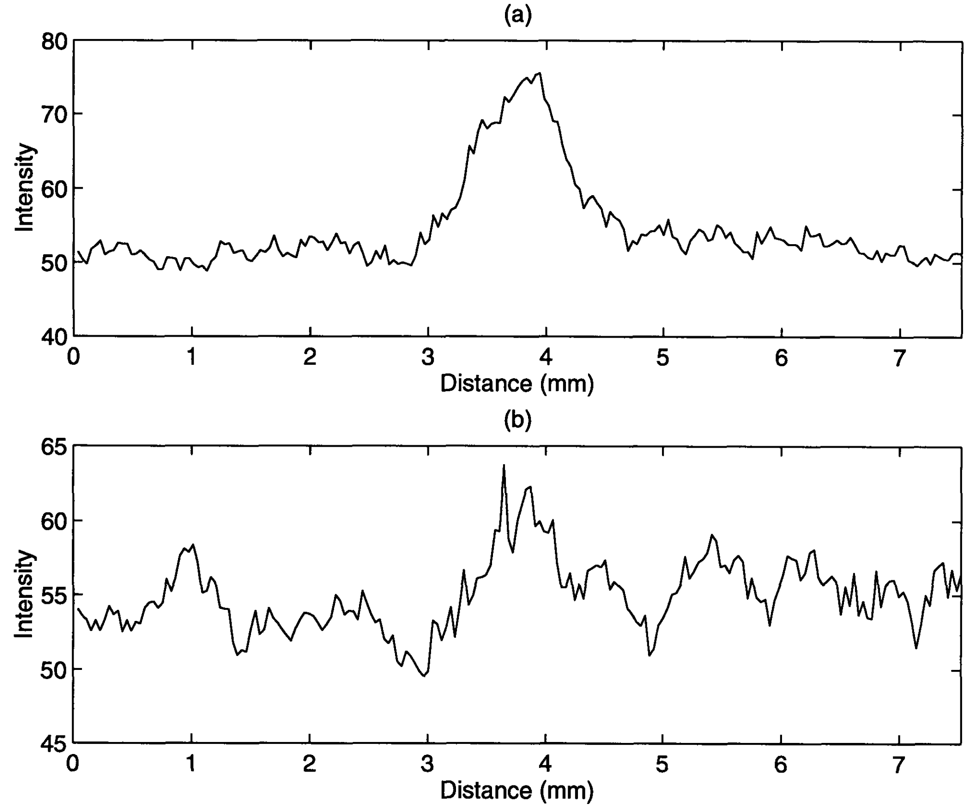

Figure 3-10: Noisy intensity profiles from actual x-ray data of (a) a 1.0mm diameter vessel phantom, and (b) a 0.6mm diameter vessel phantom.

a 0.6mm diameter vessel phantom. The apparent widths of these profiles are virtually identical, despite the fact that the actual vessel diameters differ by a factor of almost two.

Let us now consider parameter estimation using this model. We will assume that the intensity projections predicted in W-MBE occur in reality so that for a given projection, there is a 'correct' set of model parameters, $[\alpha \ r \ c_n \ \sigma \ \mathbf{b}]_{true}$, that precisely characterizes it. Furthermore, we will assume that the nuisance parameters $[c_n \ \sigma \ \mathbf{b} \ ]_{true}$ are known *a priori*, leaving a simplified problem in which α and r are the only unknowns.

Under these hypothetical conditions, the estimation of $\mathbf{a}_{true} = [\alpha \ r]_{true}$ is performed by searching over a two-dimensional parameter space to find a parameter vector $\hat{\mathbf{a}}_{ML} = [\hat{\alpha} \ \hat{r}]_{ML}$ which minimizes the cost function

$$J(\hat{\alpha}, \hat{r}) = \sum_{n} \{y[n] - f_0[n; \hat{\alpha}, \hat{r}]\}^2 \tag{3.25}$$

where f_0 is the parametric profile model and y is the noisy profile observation. For a generic ML estimation problem using a Gaussian noise model, the shape of J determines the ease of parameter estimation. Estimation is easiest when the cost surface is convex and has a single well-defined minimum (a sharp global minimum) at the true parameter location $\mathbf{a}_{true}$. The difficulty of the problem grows if the curvature of the surface falls, if the global minimum location is shifted away (by noise) from the real parameter values, or if the presence and size of local minima on the cost surface increase (these minima depend on the parametric model f_0 that is used, and on the noise characteristics). In the limit of extremely low curvature, J will be flat in the neighborhood of $\mathbf{a}_{true}$. This implies that the cost associated with $\hat{\mathbf{a}}_{ML} \neq \mathbf{a}_{true}$ in this neighborhood will be the same as the cost at the correct parameters. Any parameter values within this flat region can potentially be chosen by the estimation algorithm since they are equally appealing from a cost standpoint. The addition of local minima in J further complicates the problem, since it increases the likelihood of convergence to minima that are different from that corresponding to the real parameters. In general, the performance of parameter estimation falls as the local minima grow in number and in size.

Projections of vessels that are large relative to the point spread function are associated with favorable signal-to-noise characteristics and are less affected by blurring. The projection width and amplitude are sensitive to slight changes in vessel diameter in this size range. Thus, intensity profiles of large vessels differing slightly in diameter are distinguishable (the ability to resolve slight diameter differences is of course limited by the signal-to-noise characteristics and by blurring), and the cost surface associated with diameter estimation in these projections will be a convex function of α and r. Diameter estimation will therefore be relatively easy and the quality of estimates in this regime will be high, though imperfect because of random shifts of the global minimum (away from $\mathbf{a}_{true}$) that depend upon the noise sample path.

In vessels that are narrow relative to the point spread function, the situation is very different. These projections have poor signal-to-noise characteristics, and blurring dominates the apparent width as indicated by Figure 3-9. What little diameter information there is in the projected width is obscured by the noise. As Equation 3.24 shows, the projected amplitude remains sensitive to diameter differences even in narrow vessels, but this factor is modelled as the product of the unknown values of α and r. In general, it is impossible to uniquely determine two numbers given only observations of their product. So, the observed height of a vessel scanline can at best constrain the estimates of $\hat{\alpha}$ and $\hat{r}$ to the trajectory $\hat{\alpha}\hat{r} = c$, where c is a constant reflecting the profile height. Ordinarily, the width information would fix the value of $\hat{r}$, which in turn uniquely determines $\hat{\alpha}$. However, this information is unavailable in the small vessel regime. The dependence of this approach on the apparent profile width is the basis for our naming convention (i.e. *width-dependent* model-based estimation).

Unlike in large-vessel diameter estimation, the cost surface associated with small vessels will have a long narrow valley along this trajectory within which the cost values will be similar. The location of a global minimum within this region will be relatively more sensitive to the particular noise realization rather than to the real values of α and r. This occurs because the flatness of the cost surface valley makes its shape particularly sensitive to these noise effects, and this suggests that parameter estimation will be an ill-posed problem. Furthermore, additional local minima may be present because of noise. These factors all contribute significantly to the poor quality of the parameter estimates $\hat{\mathbf{a}}$ in narrow diameter vessels.

To verify this analysis, we simulated diameter and scaling parameter estimation from an intensity profile associated with a narrow vessel. Figure 3-11 illustrates that shape of a typical cost contour that we observed from such simulation. This was generated by first using the W-MBE imaging model to synthesize a vessel profile that was 4 pixels in radius, when the blurring parameter σ was 8 pixels. The vessel width was therefore half the point spread function width (measured as twice the standard dev. of the Gaussian p.s.f.). Sufficient white Gaussian noise was then added to approximate that in an actual x-ray intensity profile. From this simulated noisy profile, the cost surface was found by calculating the total square error between the noisy data and a modelled profile, whose scaling and radius parameters were tweaked according to the values shown on the x- and y-axes of the contour plot. The background and position parameter values were fixed at the correct values for these cost calculations.

Ideally, the cost surface should have shown a distinct minimum at the true vessel radius of 4 pixels and scaling of 1. However, we see instead that there is a long, flat 'valley' in this cost contour, as predicted by our earlier qualitative analysis. The ML radius and scaling estimates for this particular noisy profile were determined to be respectively 9 and 0.17.

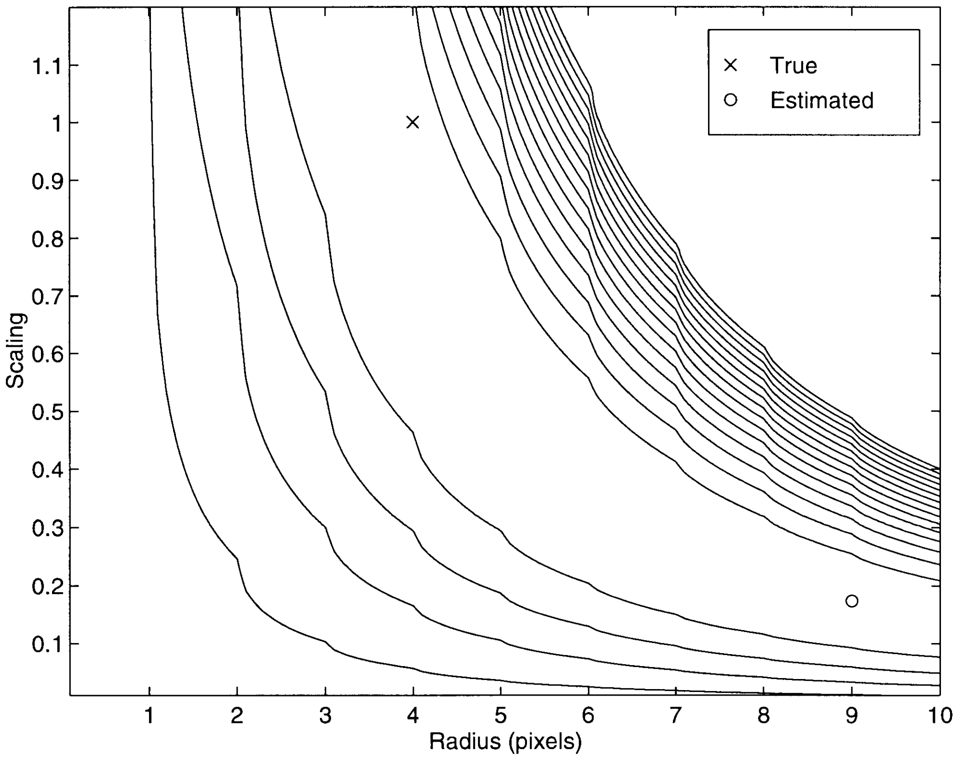

Figure 3-11: A typical cost contour associated with diameter estimation in a simulated narrow vessel profile (true radius of 4 pixels, blurring parameter value of 8 pixels, and a scaling value of 1). Cost contours are shown for the region around the minimum cost values. Both the real and estimated parameter locations are indicated.

These ML estimates, were located within the valley of the cost surface. However they were significantly different from the actual radius value of 4 and scaling value of 1, resulting in a large diameter estimation error. Examining ML estimates from several noise realizations, we found that the cost surface associated with each had a similar long flat valley structure, within which the estimated parameter values were located. In the absence of a well-defined global minimum in these cost-surfaces, parameter estimation was highly sensitive to the noise sample path — the average normalized error magnitude (in the radius estimates) (for 200 noise samples paths) was calculated to be 74% (relative to the actual radius), and the sample standard deviation of the normalized error magnitudes was 69% ! These large errors even for a seemingly simple (and idealized) problem of estimating 2 unknowns, are reflective of the problem that W-MBE has in estimating vessel widths narrower than the system blur.

In practice, W-MBE can be expected to behave even more poorly than suggested by this simplistic analysis — we would not realistically expect our imaging models to exactly match reality, nor would we know exactly the position, blurring and background parameter values. The benefit of this analysis is in our discovery that even when a significant degree of complexity has been abstracted away from the estimation problem, W-MBE has great difficulty in reliably estimating vessel diameters that are either similar in size, or smaller than the imaging point spread function width. This analysis shows that W-MBE has problems because of the lack of information about the real vessel diameter in the apparent width of an intensity profile, and because of its inability utilize the profile intensity height in estimation. We make use of this insight in our development of a new diameter estimation approach in the following chapter.

Chapter 4

Estimation using Intensity and Width Information

4.1 Objective: advancing the state-of-the-art

In Chapter 3, we found that the breakdown in width-dependent model-based estimation for vessels similar in size or smaller than the system point spread function arises because the apparent widths of their intensity projections become decreasingly sensitive to the actual arterial diameters (Figure 3-9). However, we also discovered that while the apparent widths of such vessel projections become virtually identical, their intensity profile amplitudes continue to change as vessel diameter decreases (Figure 3-10, Equation 3.24). This intensity amplitude dependence on vessel size represents a potential source of arterial diameter information that has not previously been exploited to improve estimation performance. It would therefore seem likely that a new estimator which can take advantage of the combined intensity amplitude and profile width information, should perform not only better than the existing estimators, but also better than any ad-hoc methods for improving their performance. By this reasoning we decided upon this novel approach for improving the state-of-the-art in arterial diameter measurement.

4.2 Challenges in exploiting vessel profile intensity

In W-MBE, an elliptic vessel cross-section is assumed for purposes of determining the projected width and lumen area from a single angiogram. This, coupled with the assumption that the imaging system function is an unknown linear gain, leads to an output intensity projection for which the amplitude of the vessel component is determined by the product of 3 unknowns: a width parameter r, a height parameter η associated with the projection of an elliptic lumen cross-section, and a gain parameter k associated with the imaging function (the product of η and k has previously been denoted by α). As we saw in Chapter 3, the W-MBE method of diameter measurement cannot use the profile intensity amplitude alone to determine these unknowns uniquely. Since this is the only source of arterial diameter information for small vessel projections in noise, the resulting performance is very poor. Estimation from a single projection angiogram using an elliptic projection model leads to an over-parameterized problem.

If the arterial information available is limited to a single angiographic projection, diameter estimation using the combined intensity and width information must incorporate some sort of model in which the output intensity is uniquely related to the unknown width r that is of interest. To reduce the number of unknowns which determine the arterial profile intensity in one projection image, we assume a circular cross-section for the vessel model (this is no worse than W-MBE since the parameters of the full elliptic cross-sectional model are not obtained — the only estimated parameters are those of the projected ellipse). This lumen shape is representative of a significant proportion of coronary stenoses and this will be the subset of vessel segments that we will focus on in this work. The use of intensity and width information can be applied to non-circular vessel lumen by extension of our estimator to use multiple simultaneous angiographic images acquired from different projection angles (e.g. from bi-plane angiography).

The arterial component of the projected circular vessel model is characterized by a single unknown – the width parameter, r. While this reduces the number of parameters by one over the elliptic model in W-MBE, it does not completely solve the over-parameterization problem. The imaging gain parameter is still an unknown which also determines the intensity profile amplitude. The *a priori* determination of this function is therefore a crucial first step in exploiting profile intensity for diameter estimation. However this process is complicated by the variability and non-linearity of the relationship between output image intensity and tissue attenuation (the product of the x-ray pathlength and the x-ray attenuation coefficient through tissue). This relationship depends on several factors, including the x-ray imaging conditions, the imaging system equipment and a number of patient-dependent factors such as attenuation by non-arterial structures.

At present, the methods for determining this relationship are experimentally-based, requiring additional x-ray calibration procedures during the angiographic session. An example of such a procedure involves imaging a linear wedge phantom over a patient's body during angiography [4]. This approach is problematic — the phantom obscures the angiographic image, and results in a poor approximation to the intensity function since the wedge overlies multiple regions in space with varying x-ray attenuation due to the non-uniformity of tissue thickness and x-ray attenuation characteristics within the body. Imaging the wedge alone also leads to erroneous results, since the intensity relation depends on x-ray imaging conditions which are patient-dependent and cannot be easily reproduced.

A more elaborate arrangement, by which the rotation of a circular step wedge around the rim of the image intensifier input face is synchronized with angiographic film exposure, can be used so that the wedge rotates one step per frame [18]. Inclusion of a lung segment within the angiographic imaging field provides a motionless region of temporally constant tissue thickness over which each wedge step can be sequentially superimposed and imaged. If these technical requirements are satisfied, successive angiographic frames will show the recorded image intensity as a function of the known thickness of each wedge step, superimposed over an unknown but constant lung field. In this manner, an approximation to the image intensity and tissue attenuation relationship can be obtained which avoids some of the limitations associated with using a linear wedge phantom.

In general, calibration procedures such as these are impractical to implement, particularly within clinical environments. The resulting approximations to the intensity relation may also be inadequate for diameter estimation in small vessels which must rely primarily on a quantitatively accurate description of the output intensity and arterial vessel width relation in that regime.

In order to overcome the limitations associated with calibration experiments, we reasoned that it may be possible to use model-based estimation to determine accurately the intensity function directly from the angiogram. This 'intrinsic' calibration represents a new approach to characterizing the imaging system behavior that has three key requirements:

- There must be a structure of known size and cross-sectional shape (this must be circular if only one angiographic projection is provided) whose position can be easily determined with each angiographic image.
- The contrast-medium concentration is approximately uniform and constant within the coronary arteries.
- An accurate physical model of the imaging system must be available to form the basis for model-based estimation. The parameters which characterize this model must be obtainable from the available angiographic information.

The first of these requirements is automatically met since each angiogram contains a segment of the cardiac catheter which is used for injection of contrast-medium into the coronary circulation. Cardiac catheters have circular cross-sections of known diameter. These catheters are also sufficiently large that the catheter image is associated with good signal-to-noise conditions. This allows for reliable determination of its centerline position within an angiogram using a robust centerline estimator. The second requirement of uniform contrast concentration is also satisfactorily met in all angiograms for the x-ray images obtained within the steady-state portion of contrast-medium injection into the coronary circulation. The final requirement however, requires more thought. The linear imaging system model assumed in W-MBE is obviously inadequate as a basis for model-based estimation of the image intensity function. If a simple linear relationship is assumed, the actual non-linear system function must be linearized around an operating point determined by the background intensity level and by the size of the calibration structure (cardiac catheter) that is used. The imaging gain thus obtained will be operating point dependent, and the use of a single linearized gain to estimate a range of vessel diameters in a typical angiogram with varying background intensities will inevitably lead to large estimation errors. Therefore, a more realistic non-linear imaging system model must be derived for practical exploitation of the vessel profile amplitude as an additional source of arterial diameter information. This non-linear imaging model and the resulting intensity-width dependent model-based estimator (IW-MBE) that we have developed are the topics of the following section.

4.3 Intensity- and width-dependent model-based estimation (IW-MBE)

The framework for estimation using IW-MBE is similar to that for W-MBE. Diameter estimation is performed on intensity scanlines perpendicular to the arterial centerline and, as derived in Chapter 3, the 1D observation equation for the projection of the ith vessel cross-section is

$$y_i[n; \mathbf{v}_i, \mathbf{b}_i, \sigma, \Lambda_\nu] = C_i\left\{V_i[n; \mathbf{v}_i], B_i[n; \mathbf{b}_i]\right\} * g[n; \sigma] + \nu[n; \Lambda_\nu] \tag{4.1}$$

where n is the position index along the intensity profile, $C_i\{\cdot\}$ is the imaging function, $V_i[n; \mathbf{v}_i]$ is the vessel model, $B_i[n; \mathbf{b}_i]$ is the background model, $g[n; \sigma]$ is the point spread function, and $\nu[n; \Lambda_\nu]$ is the noise process. The components of this equation that differ when using intensity and width dependent estimation are the vessel model, $V_i\{\cdot\}$, and the imaging function $C_i\{\cdot\}$.

4.3.1 The vessel model, $V\{\cdot\}$

The vessel model differs only slightly in that the cross-section is circular instead of elliptic. In this case, the ith vessel slice is given by

$$\frac{\{x - c_{x_i}\}^2}{r_i^2} - \frac{\{z - c_{z_i}\}^2}{r_i^2} = 1 \tag{4.2}$$

for a section in the xz plane, where c_x and c_z specify the center position of the lumen and r specifies its radius. The line integral projection of this slice onto the imaging plane gives the appropriate vessel model

$$V_i[n; \mathbf{v}_i] = \begin{cases} 2r_i\sqrt{1 - \frac{1}{{r_i}^2}(n - c_{n_i})^2} & \text{, if } |n - c_{n_i}| \leq r \\ 0 & \text{, otherwise} \end{cases} \tag{4.3}$$

where

$$\mathbf{v}_i = \begin{bmatrix} r_i \\ c_{n_i} \end{bmatrix} \tag{4.4}$$

are the vessel projection width and position parameters, and n represents the discrete cross-sectional position along the projection profile.

In contrast to this, the model of the imaging function differs significantly from that used in W-MBE — the linear assumption for the imaging chain operation has been abandoned in favor of a more realistic non-linear relation as derived below.

4.3.2 The non-linear imaging function, $C\{\cdot\}$

Recall that in the linear imaging model, the imaging function was

$$C_i[n; \mathbf{v}_i, \mathbf{b}_i] = \mu k' V_i(n; \mathbf{v}_i) + B_i(n; \mathbf{b}_i) = k V_i(n; \mathbf{v}_i) + B_i(n; \mathbf{b}_i) \tag{4.5}$$

where $kV_i(n; \mathbf{v}_i)$ and $B_i(n; \mathbf{b}_i)$ represent tissue attenuation by the input vessel and background models. This imaging function predicts that as the input projection, $V_i(n; \mathbf{v}_i)$ grows in size, the output image intensity will grow proportionally — there is no upper limit on the input for which further increases in magnitude produce no further change in the output intensity. This predicted behavior does not occur in a practical imaging chain, since its response is physically constrained by the characteristics of its imaging components.

As shown in Figure 4-1, the three key components of an angiographic imaging chain are the image formation block, the image recording block, and the image projection block. The image formation block represents x-ray attenuation by the opacified coronary arteries and non-arterial structures in the body, while the recording block captures the combined behavior of the image intensifier and ciné-film exposure. The image projection block describes the ciné-projector response, whose output is the final angiographic image which is analyzed.

Each of these components is a non-linear function of its corresponding input. For example, the sensitivity of the image intensifier output decreases with increasing input x-ray intensity. The ciné-film darkening response to light exposure also demonstrates saturation effects which depend on the size and density of silver-halide crystalline granules packed within the angiographic film. Finally, the ciné projector output intensity has a response that also falls off in sensitivity as a function of increasing ciné-film opacity. It is not surprising therefore, that the overall intensity response from cascading these imaging blocks likewise demonstrates decreasing sensitivity to increasing input tissue attenuation, and sat-

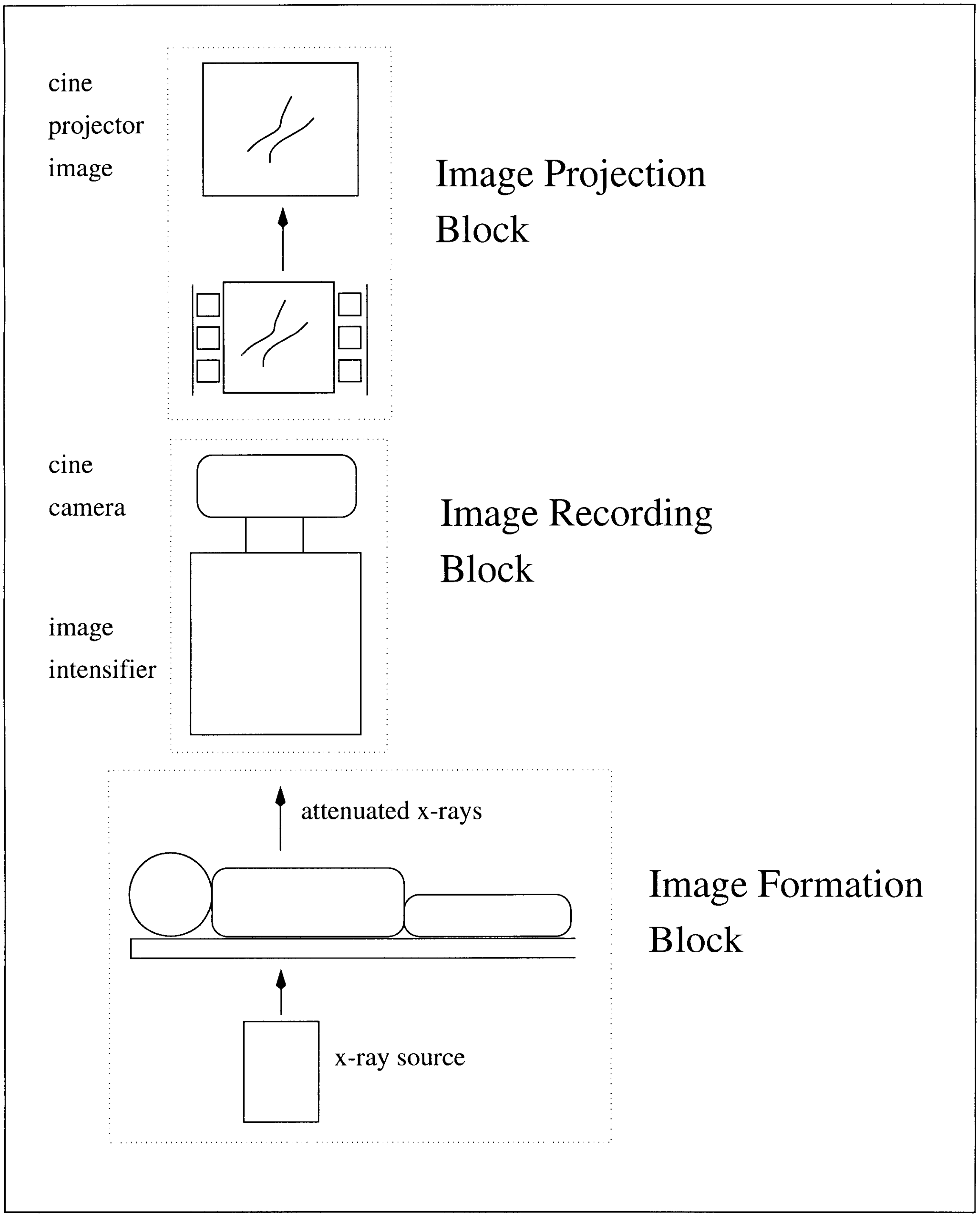

Figure 4-1: Components of a typical angiographic imaging system.

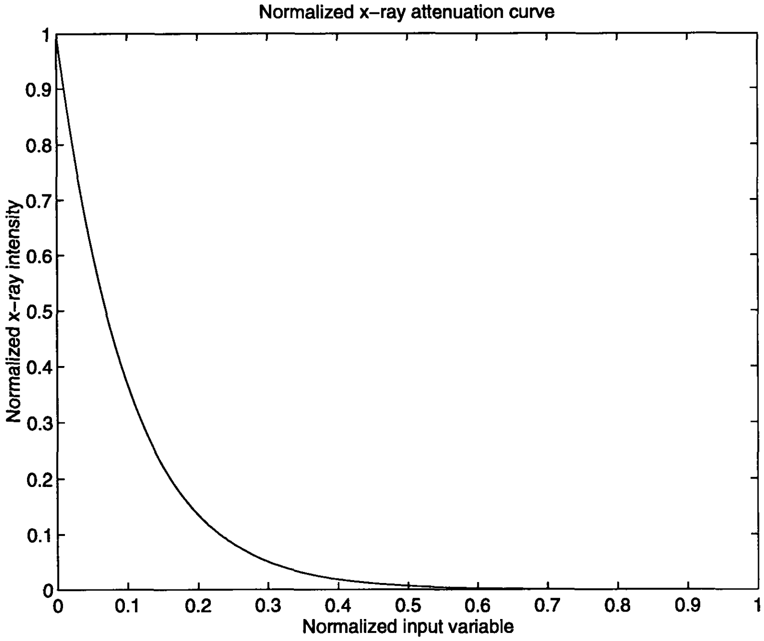

Figure 4-2: Beer-Lambert x-ray attenuation response, normalized to indicate its qualitative behavior

uration at large input levels. This behavior can be quantitatively described, assuming a monoenergetic x-ray point source and uniform intra-luminal contrast concentration, while ignoring higher-order x-ray imaging effects such as vignetting, beam hardening, and spatial distortion.

The function of the image formation block is captured by the Lambert-Beer Law which relates x-ray attenuation to the incident x-ray intensity, the x-ray pathlength, and the tissue x-ray attenuation properties. For a single intensity scanline,

$$I = I_o e^{-\{\mu V_i(n;\mathbf{v}_i)+B_i(n;\mathbf{b}_i)\}} \tag{4.6}$$

where, I_o is the incident intensity, and $\{\mu V_i(n;\mathbf{v}_i) + B_i(n;\mathbf{b}_i)\}$ is the input into this imaging block, representing tissue attenuation by structures in the x-ray path. Figure 4-2 shows the normalized shape of this curve.

The image recording block has a response given by [19]

$$D = D_o(1 - e^{-\beta I}) \tag{4.7}$$

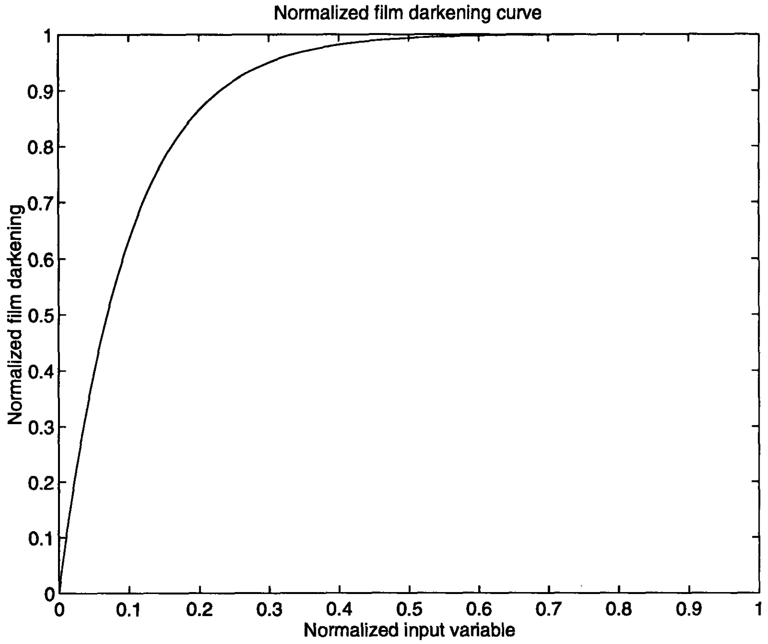

Figure 4-3: Film darkening response, normalized to show its qualitative behavior.

Here, I is the input x-ray intensity coming from the image formation block, D represents the darkening of the ciné-film recording medium, D_o is the maximum opacification of the ciné-film, and β controls the rate of response. The normalized curve shape of the darkening response is shown in Figure 4-3.

The image projection block is given by [13]

$$\rho = \rho_o 10^{-\gamma D} \tag{4.8}$$

where D is the input film opacity, ρ is the brightness of the projected image and ρ_o is the maximum output intensity. The parameter γ controls the rate at which the output intensity changes in response to the ciné-film opacity. The characteristic shape of this relation is given in Figure 4-4.

By combining the imaging component models and by making some simplifying approximations, we obtain the overall imaging function

$$C_i[n; \mathbf{v}_i, \mathbf{b}_i] = \Gamma 10^{\exp\{-\exp\{-\mu V_i(n;\mathbf{v}_i) - B_i(n;\mathbf{b}_i)\}\}} \tag{4.9}$$

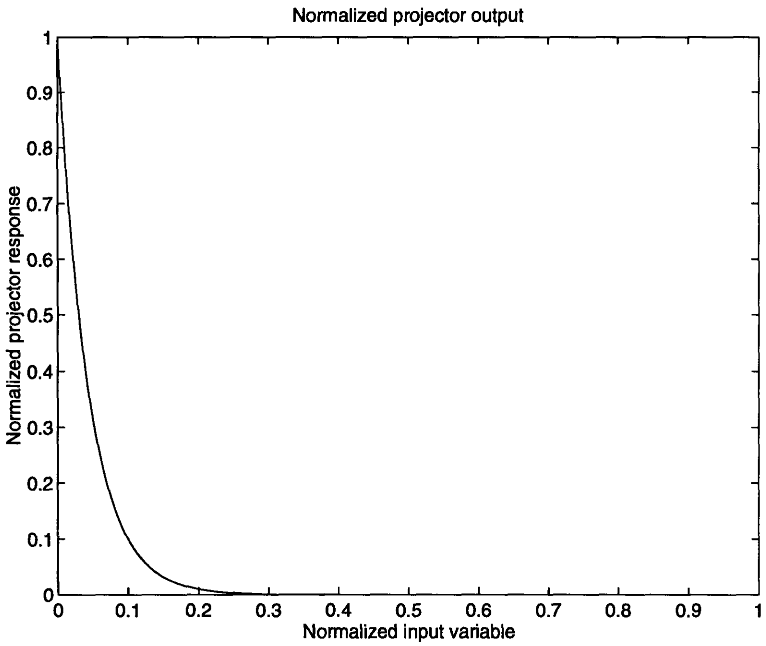

Figure 4-4: Ciné-projector response, normalized to show its qualitative behavior.

where scaling parameter $\Gamma = \rho_o 10^{-\gamma D_o}$ and the attenuation parameter μ are the unknown imaging parameters which characterize the non-linear system operation. Adjusting the predicted background intensity to zero for zero input conditions ($V_i(n; \mathbf{v}_i) = 0$ and $B_i(n; \mathbf{b}_i) = 0$) results in

$$C_i[n; \mathbf{v}_i, \mathbf{b}_i] = \Gamma \left(10^{\exp\{-\exp\{-\mu V_i(n;\mathbf{v}_i) - B_i(n;\mathbf{b}_i)\}\}} - 10^{\exp(-1)} \right) \tag{4.10}$$

The difference between this function derivation and that for the linear imaging equation lies in the fact that realistic models of the image recording and projection blocks have been used. We have avoided the assumptions that the film response is confined to the log-linear region of operation, and that the projector response is a simple linear gain. As shown in Figure 4-5, this non-linear model captures the saturation characteristics and the varying sensitivity to the input tissue attenuation that are observed using clinical angiographic imaging systems.

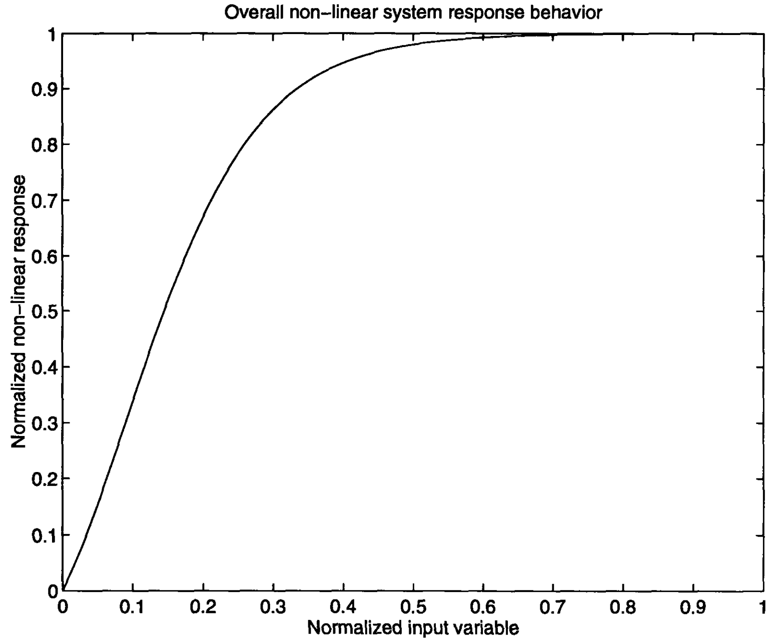

Figure 4-5: Overall shape of the non-linear imaging system response

4.3.3 Parameter estimation using IW-MBE

The 1D observation equation for scanline i used for the intensity and width-dependent approach to diameter estimation is

$$y_i[n; \mathbf{v}_i, \mathbf{b}_i, \mathbf{I}, \Lambda_\nu] = \Gamma \left(10^{\exp\left\{-\exp\left\{-\mu\sqrt{r_i^2+(n-c_{n_i})^2} - B_i(n;\mathbf{b}_i)\right\}\right\}} - 10^{\exp(-1)} \right) * g[n;\sigma] + \nu[n;\Lambda_\nu] \tag{4.11}$$

which is characterized by a set of vessel parameters, $\mathbf{v}_i = [r_i \; c_{n_i}]^T$, background parameters, $\mathbf{b}_i$, and a set of spatially invariant imaging system parameters $\mathbf{I} = [\Gamma \; \mu \; \sigma]^T$. As in W-MBE, the quantity of interest is the width measure, r_i, while the remaining variables constitute unknown 'nuisance' parameters which must be determined before accurate estimates of arterial diameter can be made.

The effects of these parameters on the predicted intensity projection of a 2D arterial cross-section are shown in Figure 4-6. The imaging gain Γ affects the amplitude and the background level of the projection, while the imaging system attenuation μ affects the amplitude and the curvature of the predicted profile. The parameters for width r_i, background $\mathbf{b}_i$, position c_{n_i}, blurring σ, and noise intensity Λ_ν are common to both estimation

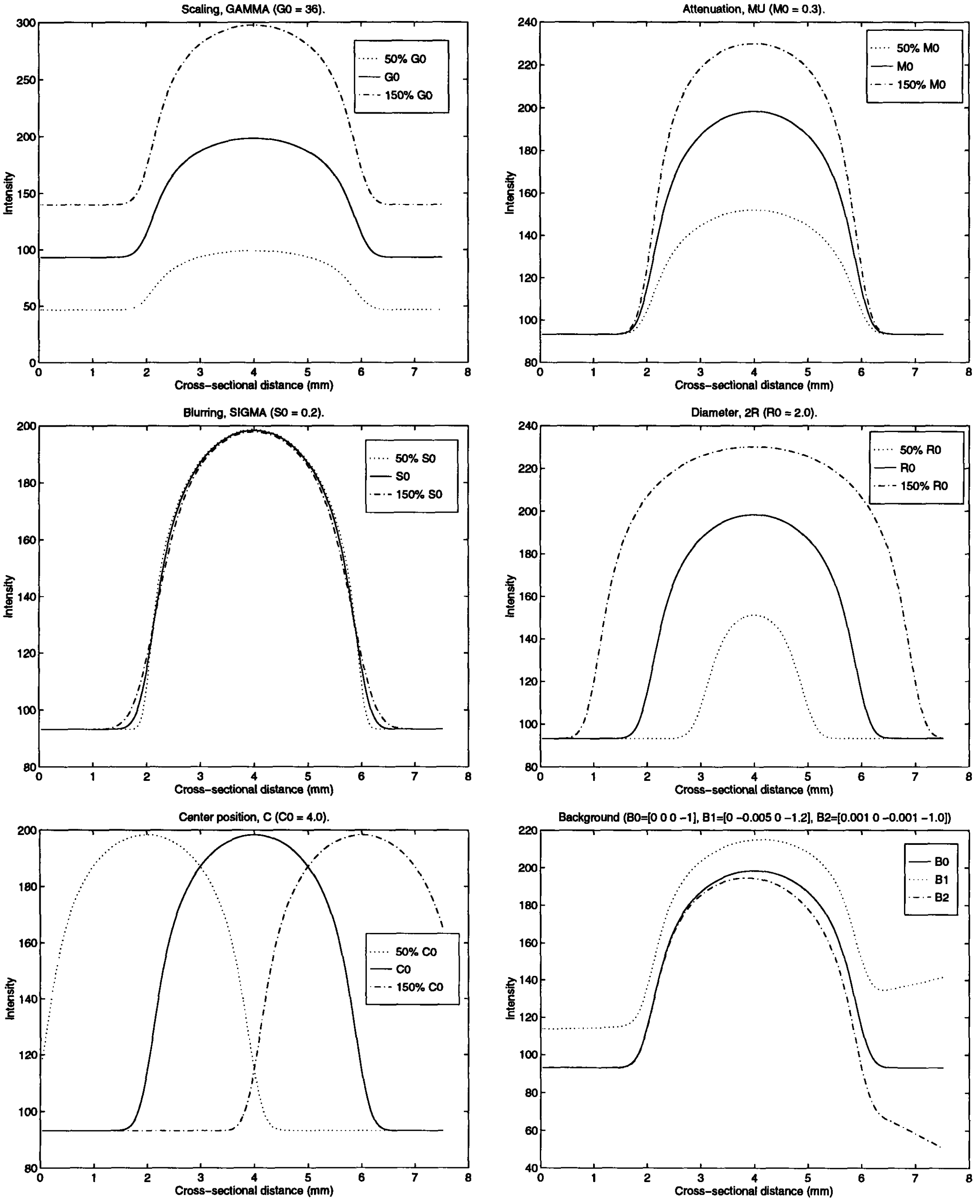

Figure 4-6: Effect of key modelling parameters on a projection profile simulated using the imaging model for IW-MBE.

using profile width alone (W-MBE), and to that which additionally uses the intensity profile amplitude (IW-MBE). These parameters have qualitatively similar effects under both schemes. There is, however, an important difference which is evident in the effect of width and background on profile shape. As either the width or the background level is increased in IW-MBE (for constant imaging system gain and attenuation), the curvature of the resulting profile flattens out near its peak, reflecting the saturation of output intensity in the non-linear model. By comparison with Figure 3-7, it is clear that this behavior is absent in W-MBE.

Joint parameter estimation over all the unknowns in IW-MBE will be difficult because of the high-dimensionality of the cost-surface. Moreover, these parameters interact in a highly non-linear fashion due to the more realistic imaging system model that is used. In order to avoid the potential pitfalls of convergence to local minima when searching the resulting non-linear and non-convex cost-surface over all its possible dimensions, we will separate this problem into two components as diagrammed in Figure 4-7. The solution to each of these steps involves solving a lower dimensional and therefore easier estimation problem. In the first step of this procedure, the least-squares estimates of the imaging system parameters are obtained from a structure of known size and cross-section that is already present within the angiographic image (e.g. a cardiac catheter). Once the ML estimates of the imaging system parameters have been determined, they are used in the second step of this procedure to estimate the unknown projection parameters associated with the arterial segment of interest.

Imaging Parameter Estimation

This is the crucial component of our intensity-width dependent approach that allows the image intensity and tissue attenuation relationship to be determined from a model-based estimator standpoint, thereby avoiding the impracticality associated with x-ray experimentation. In this step, a length of cardiac catheter (or potentially even a large cylindrical artery whose diameter can be accurately determined) of known circular cross-section and size within the angiogram is used for estimating the unknown imaging system parameters of the non-linear imaging model. The image of this cylindrical structure is first resampled along its centerline (determined using a reliable centerline estimator) to create a calibration image in which the axis of the cylinder is aligned along the center column. As shown in

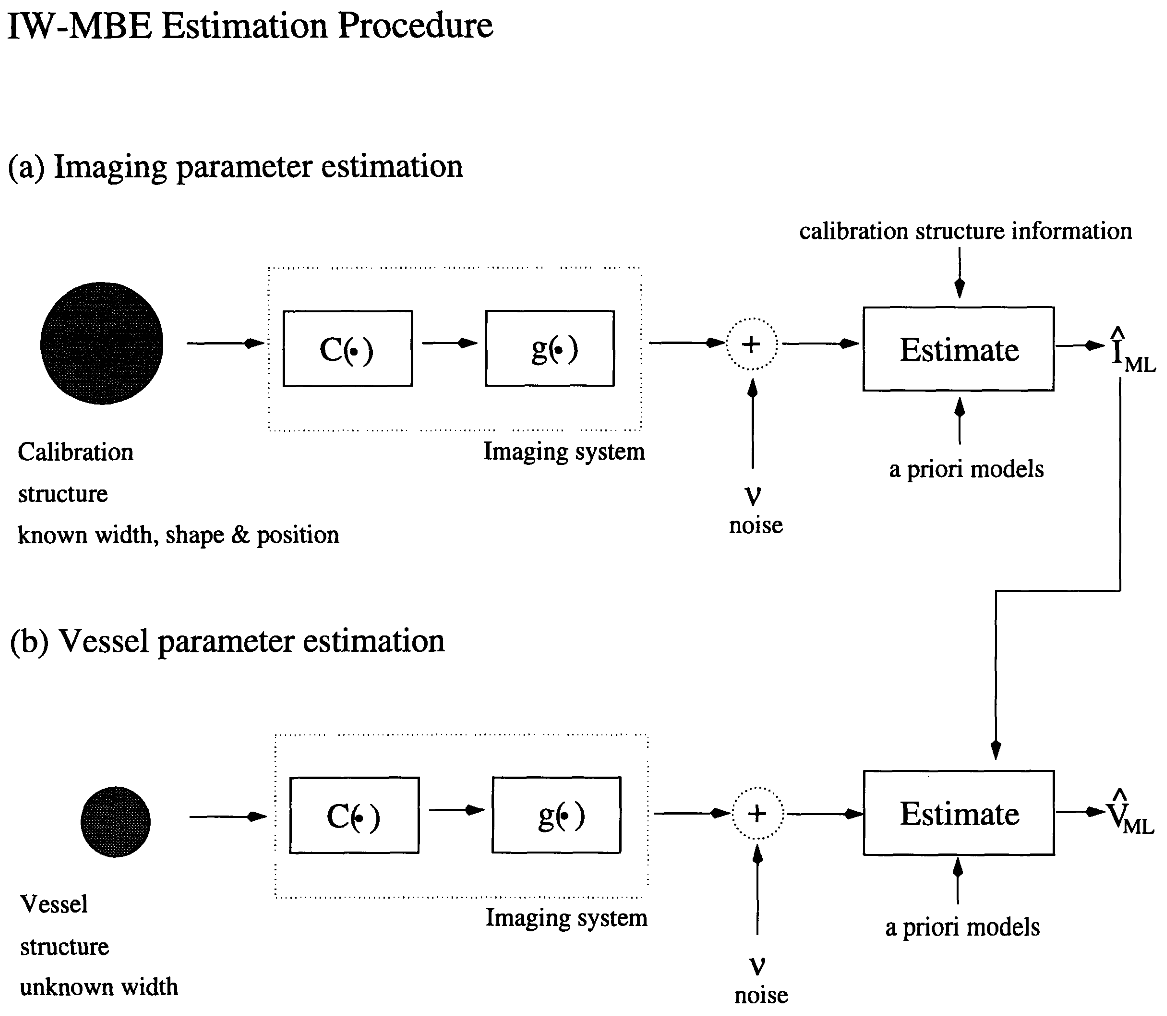

IW-MBE Estimation Procedure

(a) Imaging parameter estimation

(b) Vessel parameter estimation

Figure 4-7: Block diagram of the IW-MBE estimation procedure. (a) Imaging parameter estimation from a calibration structure already present in the image. $\hat{I}_{ML}$ is the resulting vector of imaging parameter ML estimates. (b) Vessel parameter estimation from an artery of interest. $\hat{V}_{ML}$ is the resulting vector of vessel parameter ML estimates.

Figure 4-7a, the known width and position of the cylindrical structure in the calibration image is provided to the estimation filter which determines the maximum likelihood values of the desired imaging parameters and a set of 'nuisance' background parameters. These ML estimates satisfy

$$[\hat{\mathbf{I}}\ \hat{\mathbf{b}}]_{ML} = \underset{[\mathbf{I}\ \mathbf{b}]}{argmin} \sum_i \sum_n \{y_i[n] - f_{0_i}[n; [\mathbf{I}\ \mathbf{b}]]\}^2 \tag{4.12}$$

where i represents the ith row (or intensity profile) within the calibration image, n is the column position within an intensity profile, and the parametric equation

$$f_{0_i}[n; \mathbf{I}, \mathbf{b}] = \Gamma\left(10^{\exp\left\{-\exp\left\{-\mu\sqrt{r^2+(n-c_n)^2}-B(n;\mathbf{b})\right\}\right\}} - 10^{\exp(-1)}\right) * g[n;\sigma] \tag{4.13}$$

The parameters r and c_n in this equation are assumed known and correspond to the width and position of the cylindrical calibration structure. The projection of a large cylindrical calibration structure of known cross-section provides intensity information spanning a wide range of attenuator thicknesses. These range from the very narrow towards the edges of the projected structure within the calibration image, to the very wide along the central axis of the projection. This range of attenuator thickness provides a large amount of intensity information from which to estimate the imaging parameters. Also, because the imaging parameters are assumed to be spatially invariant, we can simultaneously use multiple intensity scanlines of this wide calibration structure in imaging parameter estimation. The use of multiple scanlines enlarges the calibration dataset provides more reliable parameter estimates than is possible when single intensity profiles are used. So long as the imaging model is accurate, the resulting estimation errors should be low.

Vessel Parameter Estimation

As shown in Figure 4-7b, the estimated imaging parameters are used to extract the unknown vessel-related parameters for the arterial region of interest, which is been sampled, in the same manner as noted for the calibration structure, so that the vessel centerline is straight. In general, this vessel is narrower than the calibration structure. Estimation is performed on individual scanlines within the vessel image. The estimation filter determines the maximum likelihood values of the unknown parameters of the 1D vessel and background profiles. For the assumed Gaussian noise process, these estimates are

$$[\hat{\mathbf{v}}_i \ \hat{\mathbf{b}}_i]_{ML} = \underset{[\mathbf{v}_i \ \mathbf{b}_i]}{argmin} \sum_n \{y_i[n] - f_{0_i}[n; [\mathbf{v}_i \ \mathbf{b}_i]]\}^2 \tag{4.14}$$

where i represents the ith cross-sectional projection, and the parametric equation

$$f_{0_i}[n; \mathbf{v}_i, \mathbf{b}_i] = \Gamma\left(10^{\exp\{-\exp\{-\mu\sqrt{r_i^2+(n-c_{n_i})^2}-B_i(n;\mathbf{b}_i)\}\}} - 10^{\exp(-1)}\right) * g[n;\sigma] \tag{4.15}$$

Initialization

The iterative Nelder-Mead simplex cost minimization algorithm is used in our implementation of IW-MBE. This has the advantage of being robust to cost-surface discontinuities, but is a slow algorithm since it requires numerous cost-function evaluations for each iteration. In this work, we are not concerned with speed or computational issues in our implementation. Rather, we are interested solely in the degree of estimation performance improvement when using the profile intensity as an additional source of arterial diameter information. As with all iterative numerical algorithms, initial conditions must be supplied for the unknowns. We use the arterial width derived from derivative-based edge-detection [12, 17] as the initial guess for the width parameter, and the result from centerline estimation [15] to initialize the center position of the vessel in each scanline. The background parameters are initialized to correspond to the DC level of the observed intensity data in the non-arterial component of the angiographic image. The imaging parameters are physically bounded by the real-world behavior of a practical imaging chain. We initialize these parameters by using typical values which also correspond to the mid-points in the range of values that are physically possible.

4.4 Assessment of IW-MBE using simulation experiments

In this section, we use computer simulation to examine the performance of IW-MBE, and to compare it with that of existing W-MBE and DBE approaches. Simulations in this manner are of course limited by the accuracy with which they model reality, and as such, the results obtained cannot be expected to match exactly those obtained clinically. This approach does however provide a relatively quick and inexpensive method of running numerous scenarios for which precise control of the experimental variables is available. The effects of a single parameter, such as imaging noise, on estimation performance can be studied in isolation, since all other factors can be held constant in simulation. This contrasts with actual x-ray experimentation in which several variables may be simultaneously changing along with the parameter of interest being investigated. While the results from simulation are artificial, they do offer valuable insight into the performance of our estimator, relative to that of other schemes, under idealized conditions in which the assumed models match perfectly with reality. The behavior thus determined represents an upper-bound on estimation quality from IW-MBE, since its operation will likely be worse under conditions for which there is modelling mismatch.

4.4.1 Experimental Overview

Synthetic data

Starting with real x-ray images of contrast-filled cylindrical bores of known diameter lying over a homogeneous attenuator, we estimated 'typical' values for the imaging system parameters. One such set of imaging parameters is $\Gamma = 36$ for the scaling parameter, $\mu = 0.3$ for the attenuation, and $\sigma = 0.2$mm for the system blur. The corresponding characteristic curve shape for these values of Γ and μ is shown in Figure 4-8. In reality, each of these parameters is bounded by the physical behavior of the imaging chain. The blurring by the system always exceeds some minimum value (or diameter estimates of narrow vessels would not level off at the width of the point spread function), and it is lower than some maximum blurring (or the system would not have passed quality controls). The x-ray attenuation cannot exceed the x-ray attenuation coefficient of pure iodine, and it must be higher than some minimum threshold required for making the coronary arteries stand out above the non-arterial tissue in an angiographic image. The gain of the x-ray imaging chain is also bounded because of analogous design constraints.

The synthetic image data used in our simulation experiments are simulated based on our model. The desired vessel and background parameters for the image to be synthesized are taken, along with the imaging parameters Γ and μ, as inputs into the image formation block. This generates an uncorrupted image that represents the output of the non-linear imaging chain in the absence of blur and noise. This image is then blurred using a Gaussian point spread function characterized by the imaging parameter σ. Finally, spatially white Gaussian noise of intensity Λ_ν is added to the blurred image. A typical example of a noisy synthetic

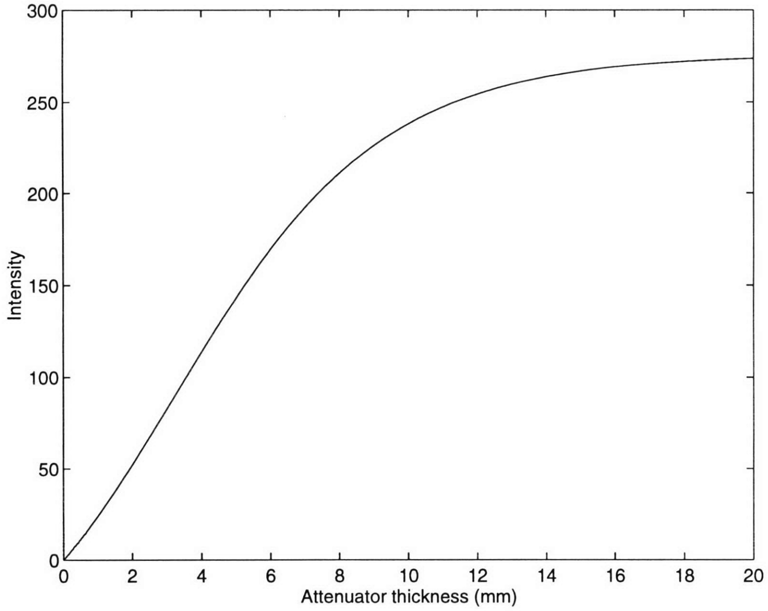

Figure 4-8: Characteristic curve shape for imaging parameters Γ=36, μ=0.3, as a function of attenuator thickness.

vessel projection image is shown in Figure 4-9. A typical intensity profile through this image is shown in Figure 4-10. The simulated vessel in this image has a diameter of 2.0mm (r = 1.0mm) and has a vessel centerline position c_n of 4.0mm. The imaging parameters for this simulation are $\Gamma = 36$, $\mu = 0.3$, and $\sigma = 0.2$mm. The noise intensity level $\Lambda_\nu = 9$. These parameters approximate those typical of real x-ray coronary angiograms.

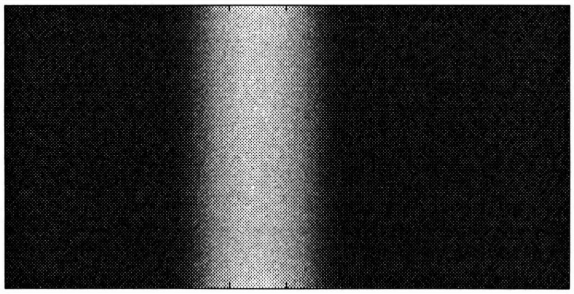

Figure 4-9: A typical simulated x-ray image of a 2.0mm diameter vessel.

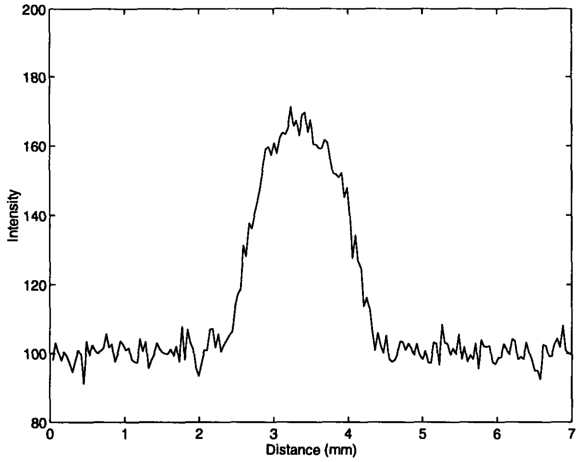

Figure 4-10: A noisy intensity profile of a simulated 2.0mm diameter vessel.

4.4.2 Procedure

Since there are two estimation steps involved in the intensity-width method, it is important to characterize the behavior of each component in response to variations in modelling conditions. In our first set of simulations, we assume that we have perfect knowledge of the imaging system parameters, so that we are dealing only with estimation of the unknown vessel and background characteristics in the presence of noise. The results of these simulations give us insight into the best possible performance of IW-MBE when we do not have to factor in the additional complications of estimating the imaging system parameters. If, even under these greatly idealized conditions, we find that no improvement is made over existing schemes, then the use of profile intensity as an aid to arterial width measurement will not be very promising. We will analyze the performance of the vessel measurement step for different noise levels, for different vessel diameters, and for different simulated background projections. We will also study the effects of imaging parameter mismatch on the resulting estimation quality. Since vessel diameter measurements for these cases are performed on independent 1D intensity scanlines, the background model used in the estimation step for IW-MBE and W-MBE is a 1D third-degree polynomial.

In our second set of experiments, we will explore more realistic scenarios in which the imaging parameters are in fact unknown to begin with. We will analyze the quality of imaging parameter estimates when using two different calibration structure sizes, and when performing estimation under varying noise conditions, background projections, as well as imaging system operating points. We will examine the sensitivity of image parameter estimation to initial condition values perturbed away from the set of true image parameters used in the synthetic data generation. For these simulations, multiple consecutive image scanlines are used simultaneously to estimate the imaging parameters. As a consequence, we treat the background intensity as continuous across scanlines, and the background model used for the estimation procedure is a 2D second-degree polynomial function.

Finally, we shall combine the imaging parameter estimation step with vessel parameter estimation to study the overall variability and accuracy in diameter estimates obtained by carrying IW-MBE through from beginning to end. In each of our simulations, the modelling parameters which were not under investigation were held fixed (background, noise, r, c, Γ, μ, and σ). For imaging parameter estimation from multiple scanlines, the background model assumed for the estimation step was a two dimensional second-degree polynomial function, and for vessel parameter estimation in single scanlines, the background model was assumed to be a one dimensional third-degree polynomial function.

The specific details and performance metrics used for each experiment are presented below along with the observed results. The simulated image resolution for the scenarios investigated was 0.0446mm/pixel, which is typical of angiographic images. The derivative-based method implemented for comparison is a weighted average of the first and second derivatives of the intensity profiles where the weighting factor used is 0.79. This weighting was chosen in preference over the traditional value of 0.5, since a recent x-ray experimental study by Sonka et al. [17] showed good diameter estimates over a wide range of vessel sizes when using this weighting value. The first and second derivatives, at each point along a given projection profile, are computed by calculating the corresponding derivatives of a least-squares second order polynomial fit to a set of 7 adjacent points [10]. The vessel profile diameter is obtained as the distance between the two maxima in the weighted derivative sum that represent the two vessel borders within that scanline.

In our model-based estimation algorithms, the background parameters and the vessel parameters are estimated separately since we begin with reasonably good initial condition values for background and vessel. In this process, the output of the background estimation step is held fixed in the vessel parameter estimation step, and vice versa. Iteration between these steps is performed until the parameter values from successive iterations converge to values different by no more than 0.0001. The Nelder-Mead simplex searching algorithm is used for both the IW-MBE and W-MBE methods as described previously.

4.5 Estimation of vessel parameters given known imaging parameters

4.5.1 Effect of noise level

In this investigation, we studied the effect of increasing noise intensity on diameter estimation from the simulated vessel projections of a 3.0mm diameter (i.e. large) and a 0.5mm diameter artery (i.e. small). All simulation parameters aside from the noise intensity Λ_ν were held constant for the large and small vessel image datasets studied. The imaging parameters used were gain $\Gamma = 36$, attenuation $\mu = 0.3$, and the blurring $\sigma = 0.2$mm. The vessel centerline position was $c_n = 4.0$mm, and a uniform background corresponding to $b_0 = -1.0$ (with all other background coefficients set to zero) was used for simplicity. We added 5 different levels of noise intensity to the simulated images whose range encompasses the extremes of very low and very high noise conditions that may be found in x-ray angiography. These noise variances were $\Lambda_\nu = 1, 9, 25, 49$, and 81. We defined the signal-to-noise ratio as,

$$\text{SNR} = 10\log_{10}\left(\frac{\mathbf{v}^T\mathbf{v}}{\Lambda_\nu N}\right) \tag{4.16}$$

where $\mathbf{v}^T\mathbf{v}$ is the total signal power in the uncorrupted vessel profile component, $\mathbf{v}$, $\Lambda_\nu N$ is the total power in the noise and N is the vector length of the simulated image scanline. Using this definition, we calculated the corresponding SNR values for these experiments to be respectively 32.9dB, 23.4dB, 18.9dB, 16.0dB, and 13.8dB for the 3.0mm vessel images, and 8.3dB, -1.2dB, -5.7dB, -8.6dB, and -10.8dB for the 0.5mm vessel projections. In general, the SNR value decreases as the vessel diameter decreases (since the signal becomes smaller) for a constant noise intensity value for Λ_ν. For these simulations, we considered 100 different noisy realizations of image scanlines. For each of these sample paths, we estimated the vessel and background projection parameters, providing the IW-MBE estimation algorithm with the correct imaging parameters that were actually used in image synthesis. For W-MBE estimation, the actual imaging blur used in image generation was provided. Both the model-based estimators (IW-MBE and W-MBE) were initialized using the same initial guesses for vessel diameter (determined by edge-detection), the same initial values for vessel centerline position, and the same initial background intensity levels.

The diameter estimation performance for the ith realization was evaluated by using the magnitude of the normalized percent measurement error given by

$$\frac{|\hat{x}_i - x_i|}{|x_i|} \times 100 \tag{4.17}$$

where $\hat{x}$ is the estimated diameter and x is the true vessel diameter. The mean and standard deviation of this performance metric under varying conditions of signal-to-noise are shown in Figure 4-11 for the 3.0mm synthetic large vessel data, and in Figure 4-12 for the 0.5mm synthetic small vessel data. The normalized mean estimation error reflects the measurement accuracy or bias, whereas the normalized standard deviation indicates the variability or reproducibility of the measurements. In these figures, larger mean normalized error are associated with greater the estimation bias and higher normalized error standard deviations correspond to greater uncertainties in the estimated diameters. For this background level, the approximate range of typical SNR values for a true x-ray image of a 3.0mm diameter vessel lies between 23dB and 27dB whereas that for a 0.5mm vessel x-ray projection lies between -3dB and 3dB.

These data show that diameter estimation using any given approach is significantly better (demonstrating smaller bias, and lower error variance/standard deviation) for the large 3.0mm diameter vessel than for the small 0.5mm diameter vessel. This observation is expected since narrower vessels are associated with smaller signals, and the resulting projection images possess poorer signal-to-noise characteristics than those from larger vessels for the same intensity level of imaging noise. The estimation problem is therefore more difficult for narrow vessels, and so reduces estimation performance. The low values of SNR associated with these vessels are reflected in the abscissae of the plots for the 0.5mm diameter vessel data.

For the SNR conditions that were simulated, estimation using combined intensity and width information (IW-MBE) produced the highest quality estimates overall, showing the smallest bias and the lowest error variance for the noise intensity levels investigated. This was followed by model-based diameter measurement using only width information (W-MBE). The poorest overall estimates resulted from the simple derivative-based edge-detector for diameter extraction (DBE). These derivative-based estimates were slightly poorer than

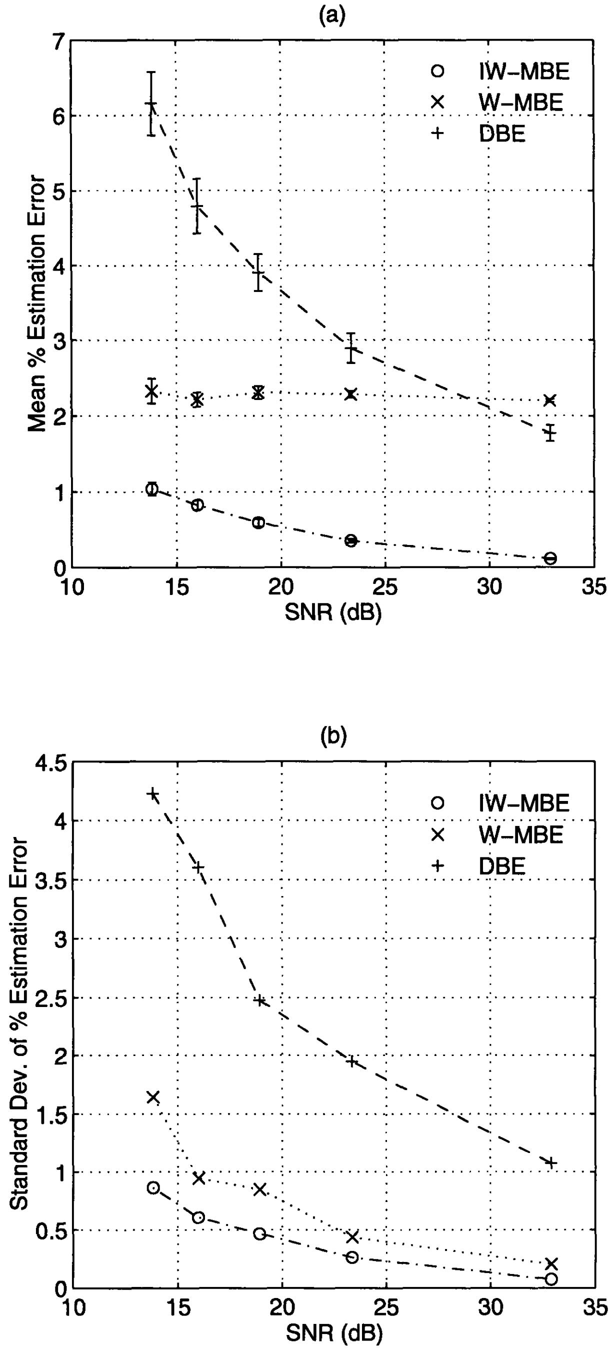

Figure 4-11: Results from measuring a large 3.0mm diameter vessel image corrupted by varying levels of noise intensity. The correct imaging system parameters were assumed to be known for these simulations. (a) Mean normalized diameter estimation error from IW-MBE, W-MBE and DBE under varying signal-to-noise conditions. Error bars represent one standard deviation in the mean error. (b) Standard deviation of the normalized diameter estimation errors as a function of signal-to-noise.

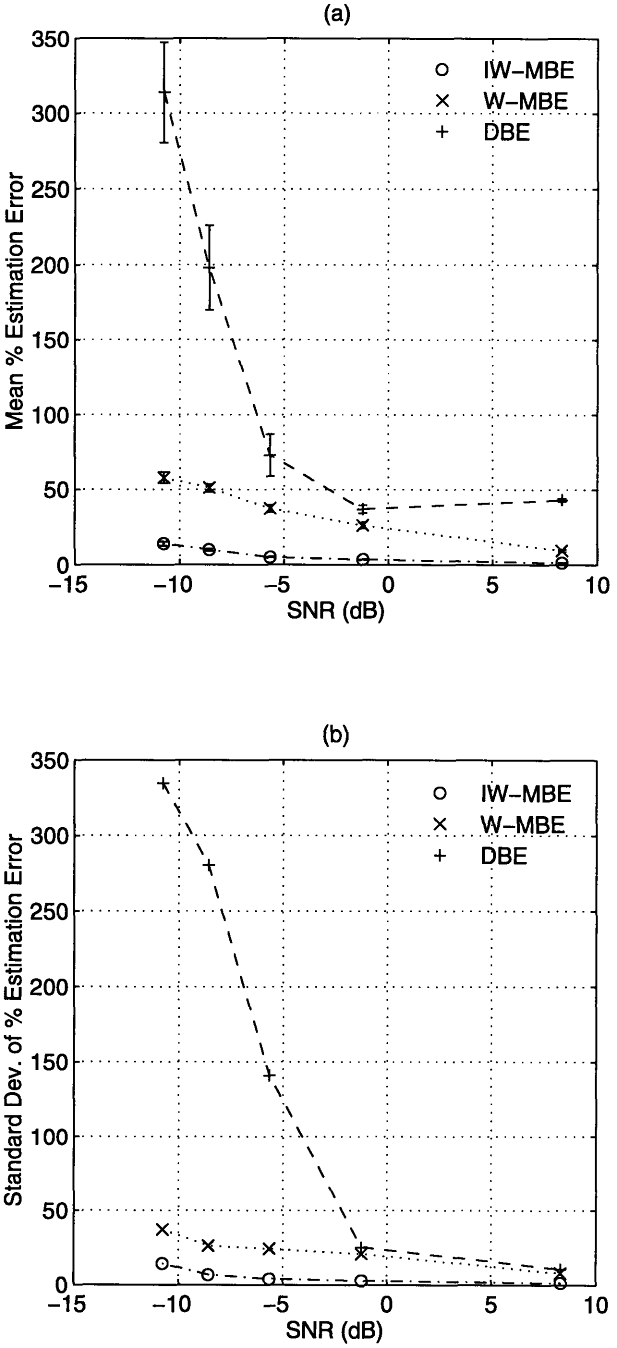

Figure 4-12: Results from measuring a small 0.5mm diameter vessel image corrupted by varying levels of noise intensity. The correct imaging system parameters were assumed to be known for these simulations. (a) Mean normalized diameter estimation error from IW-MBE, W-MBE and DBE under varying signal-to-noise conditions. Error bars represent one standard deviation in the mean error. (b) Standard deviation of the normalized diameter estimation errors as a function of signal-to-noise.

those reflected in other studies [7, 17], since no post-processing, such as diameter smoothing, was performed on the results, as would normally be used when DBE is employed. Derivative information from multiple scanlines was not used for smoothing diameter estimates to ensure that the three measurement schemes could be fairly compared, since our implementation of the model-based techniques treats estimation in separate scanlines completely independently. Alternatively, we could have chosen to use the same post-processing algorithm to obtain smoothed vessel diameter estimates for all three methods. However, since this would have had the same effect on the results from each of these estimators, it was simpler and equally informative to bypass this step, and to consider only estimation performance on the basis of independent image scanlines.

Our simulation results for the large 3.0mm diameter vessel image in Figure 4-11 show that estimation using the combined intensity and width information in an image produces the smallest measurement bias and lowest measurement variability of the three estimators tested, over the entire range of signal-to-noise conditions that were explored. The general trend in these curves is that bias and variability increase as SNR falls. The gradient of the standard deviation curve as a function of SNR for IW-MBE is smaller than those for W-MBE and DBE. Since curve steepness or curvature reflects estimator noise sensitivity, we can see that the reproducibility of IW-MBE is the least affected by imaging noise, followed by W-MBE and then by DBE which has the greatest noise sensitivity. It is interesting to note that the estimation bias produced by W-MBE and DBE are comparable at very high values of SNR ($>$ 28dB), while the bias from IW-MBE under the worst noise conditions is about half of that from W-MBE or DBE obtained under the most favorable noise conditions studied. It is important to note that the magnitudes of the normalized bias and standard deviations observed using these estimators are small fractions of the actual diameter in these simulations (even for the poorest signal-to-noise conditions). This of course reflects the relative ease with which large diameter vessel measurements can be made.

The improvement in estimation performance achievable by simultaneously exploiting profile width and intensity is most obvious in small diameter measurements. Figure 4-12 shows the normalized bias and standard deviations as functions of SNR for a narrow 0.5mm diameter simulated vessel image. Here, the same qualitative trends as for the large 3.0mm vessel image can be seen in the estimation performance of each estimator. However, the significance of the quantitative differences in estimation quality between them is much greater, and the measurement performance is poorer here for all three methods than in the large vessel simulations. Within the typical range of SNR values for a 0.5mm vessel, the estimation bias and variability from both W-MBE and DBE are significant fractions of the true vessel diameter. These characteristics emphasize the fact that accurate and precise diameter measurements cannot be made in narrow vessel constrictions using these existing estimators.

We observe that DBE estimation was extremely sensitive to increasing noise intensity. Estimation errors using this scheme rose sharply from a measurement bias of 40% and standard deviation of 11% at an SNR value of 8.3dB to a bias of 314% and a standard deviation of 335% at the lowest simulated SNR value of -10.8dB. W-MBE results from these small vessel measurements were less sensitive to noise and demonstrated lower bias and variability than DBE estimates. For this approach, the normalized bias and standard deviation rose from about 10% and 8% respectively for SNR=8.3dB, to about 58% and 37% respectively for SNR=-10.8dB. The best results were obtained from IW-MBE, which showed measurement bias rising from 1.4% to 14% and measurement standard deviation rising from 1.3% to 14%, as SNR values fell from 8.3dB to -10.8dB. Within the typical range of SNR values for a 0.5mm vessel ($-2\text{dB} \leq \text{SNR} \leq 3\text{dB}$), the curvature of the IW-MBE estimation bias and variability curves as a function of SNR are also the flattest of the estimators tested, indicating its low noise sensitivity relative to W-MBE and DBE. At an SNR value of -1.2dB (within the typical range of SNRs obtained from actual x-ray angiograms), the IW-MBE estimation bias was observed to be about 7 times smaller than that from W-MBE, and 10 times smaller than that from DBE. At this SNR, the normalized sample standard deviation for IW-MBE was smaller than that of W-MBE by a factor of 8, and smaller than that of DBE by a factor of 9.

These simulation results suggest that, of the three estimators implemented, IW-MBE offers the most reliable estimates under all the noise conditions that were studied, followed by W-MBE, and then by DBE. Of these estimators, only IW-MBE produces diameter estimates over a wide range of noise conditions which have sufficiently low bias and variance such that reliable and accurate (and therefore meaningful) measurement of small vessel diameters can be made.

4.5.2 Effect of vessel diameter

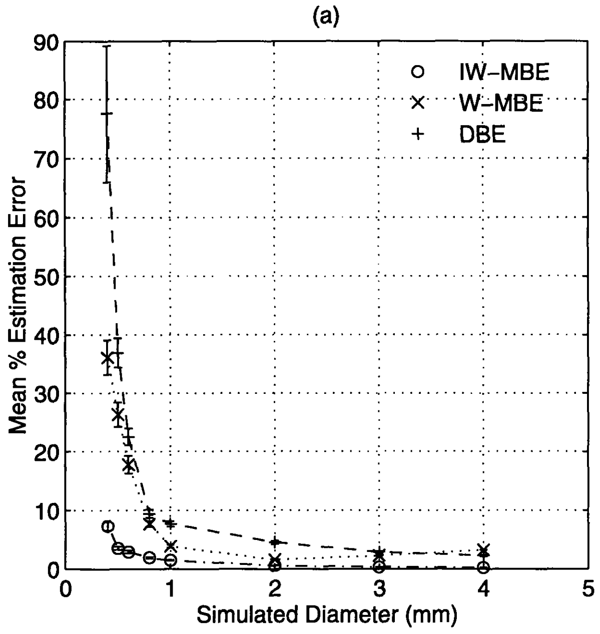

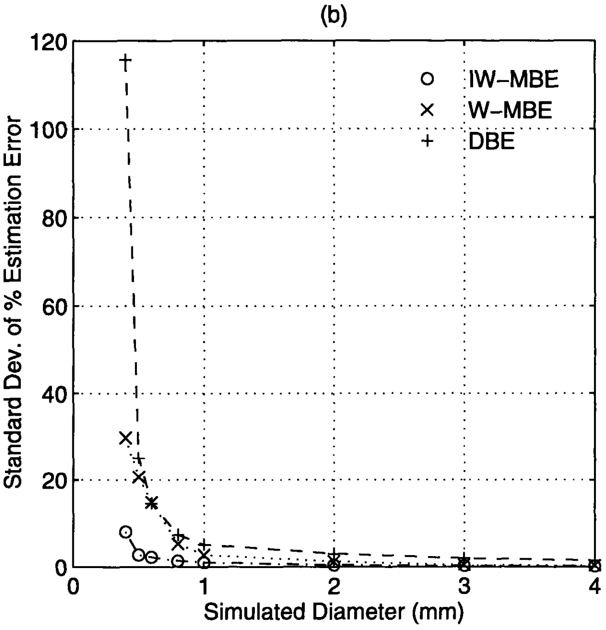

Figure 4-13: Diameter estimation results from IW-MBE, W-MBE and DBE for varying vessel size and fixed noise intensity. The imaging system parameters were assumed to be known and correct in these experiments. For the simulated noisy intensity Λ_ν of 9, the SNR values ranged from -4.8dB for the 0.4mm simulated vessel, to 27dB for the 4.0mm diameter vessel. (a) Mean normalized error as a function of vessel diameter. Error bars represent one standard deviation in the mean error. (b) Standard deviation of the normalized measurement error as a function of diameter.

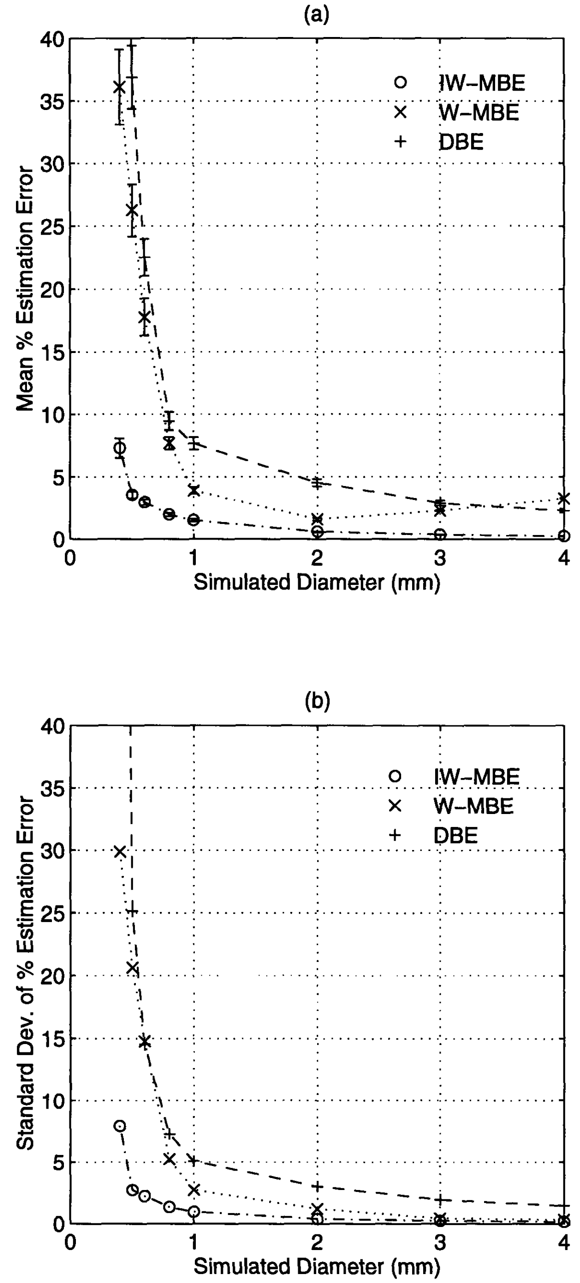

Figure 4-14: Close-up view of the results for diameter estimation of varying vessel size under fixed noise intensity. The imaging system parameters were assumed to be known and correct in these experiments. For the simulated noisy intensity Λ_ν of 9, the SNR values ranged from -4.8dB for the 0.4mm simulated vessel, to 27dB for the 4.0mm diameter vessel. (a) Mean normalized error as a function of vessel diameter. Error bars represent one standard deviation in the mean error. (b) Standard deviation of the normalized measurement error as a function of diameter.

In this experiment we studied parameter estimation from synthetic images of vessels ranging in diameter from 0.4mm to 4.0mm. The exact values of diameter used were 0.4mm, 0.5mm, 0.6mm, 0.8mm, 1.0mm, 2.0mm, 3.0mm, and 4.0mm. The imaging parameters were fixed at $\Gamma = 36$, $\mu = 0.3$, and $\sigma = 0.2$mm. The background intensities were flat and constant throughout these simulations ($b_0 = -1.0$ with the other background coefficients set to zero). The vessel centerline positions were fixed at 4.0mm for each image. The noise intensity used was $\Lambda_\nu = 9$, corresponding to an SNR of 23.4dB for the 3.0mm diameter vessel projection. Parameter estimation was performed in 100 noisy sample paths. The correct imaging system parameters were used for IW-MBE, and the correct blurring was used for W-MBE measurements. For both approaches the correct noise model was also used. The iterative algorithms for the model-based estimators were initialized to the same starting guesses for the vessel diameters, centerline positions, and backgrounds.

The normalized percent diameter measurement error given by Equation 4.17 was used to assess the performance of each estimator. The mean and standard deviation of this metric as functions of simulated vessel diameter are shown for IW-MBE, W-MBE and DBE in Figure 4-13. Figure 4-14 shows an expanded view of these data so that performance differences between IW-MBE and W-MBE can be seen in greater detail.

For vessel diameters larger than 1.0mm, the estimation bias and variability from each estimator were small relatively constant as a function of the simulated diameter. IW-MBE showed the best performance (though only slightly better than the other estimators), followed by W-MBE and then by DBE in this vessel size range. For vessel diameters smaller than or equal to 1.0mm, the bias and standard deviation of the estimation error for DBE rose the fastest out of these estimators as a function of falling vessel diameter. This is followed by W-MBE and then by IW-MBE which demonstrated the lowest performance sensitivity to vessel diameter and the smallest overall bias and variability. For the narrowest simulated vessel diameter of 0.4mm, the IW-MBE normalized bias was 7.3% of the true width, whereas the biases from W-MBE and DBE were respectively 36.1% and 77.6%. These IW-MBE bias values translate approximately into a factor of 4.9 improvement in measurement bias than W-MBE, and a factor of about 10.6 smaller bias than DBE. The error standard deviation of 7.9% for IW-MBE was almost 4 times smaller than that of W-MBE (29.9%), and was almost 15 times smaller than that of DBE (115.7%).

These simulation results therefore suggest that, of the schemes implemented, model-based measurement using both intensity and width information provides the best estimation quality over the range of vessel diameters explored. The performance improvement of IW-MBE over W-MBE and DBE, both of which exploit only profile width information, is particularly striking within the small vessel regime (diameters $\leq$ 1.0mm) where the width of the intensity profiles depends on the imaging blur rather than on the true diameter.

4.5.3 Effect of simulated angiographic backgrounds

For these simulations, the background parameters alone were varied to study their influence on diameter measurement using IW-MBE. Two sets of images corresponding to a large vessel (3.0mm diameter) and a small vessel (0.5mm diameter) were also used in order to distinguish any possible diameter dependent effects of background on estimation performance. The imaging parameters used were scaling $\Gamma = 36$, attenuation $\mu = 0.3$, and blurring $\sigma = 0.2$mm. The noise intensity in these simulations was fixed at $\Lambda_{\nu} = 9$, which translates into SNR values of 23.4dB for the 3.0mm vessel and -1.2dB for the 0.5mm vessel when the background model is homogeneous (corresponding to a constant background intensity) and characterized by $b_0 = -1.0$ with the higher-order background coefficients set to zero. The different backgrounds studied approximate those observed from actual angiographic profiles, and are shown in Figure 4-15. We performed diameter estimation in 100 different noisy profiles, using the known imaging system parameters for IW-MBE and the known imaging blur for W-MBE. The initial values for diameter, centerline position, and background coefficients were the same for both IW-MBE and W-MBE. These were determined as previously described.

The mean and standard deviation of the normalized diameter estimation error (Equation 4.17) are shown in Figure 4-16 for a large 3.0mm diameter simulated vessel, and in Figure 4-17 for a small 0.5mm diameter vessel image. Figure 4-18 is a close-up view of the 0.5mm diameter vessel results to show greater detail.

The measurement results for the 3.0mm vessel show that the bias and standard deviation were relatively small relative to the true diameter for all three estimators across the background profiles studied. The IW-MBE estimates showed the smallest bias ($\sim 0.5\%$) and variability ($\sim 0.5\%$), as well as the least sensitivity to background profile shape. The W-MBE estimates showed higher bias and lower reproducibility than IW-MBE. The measurement bias was also more sensitive to changes in the background profile intensity, although

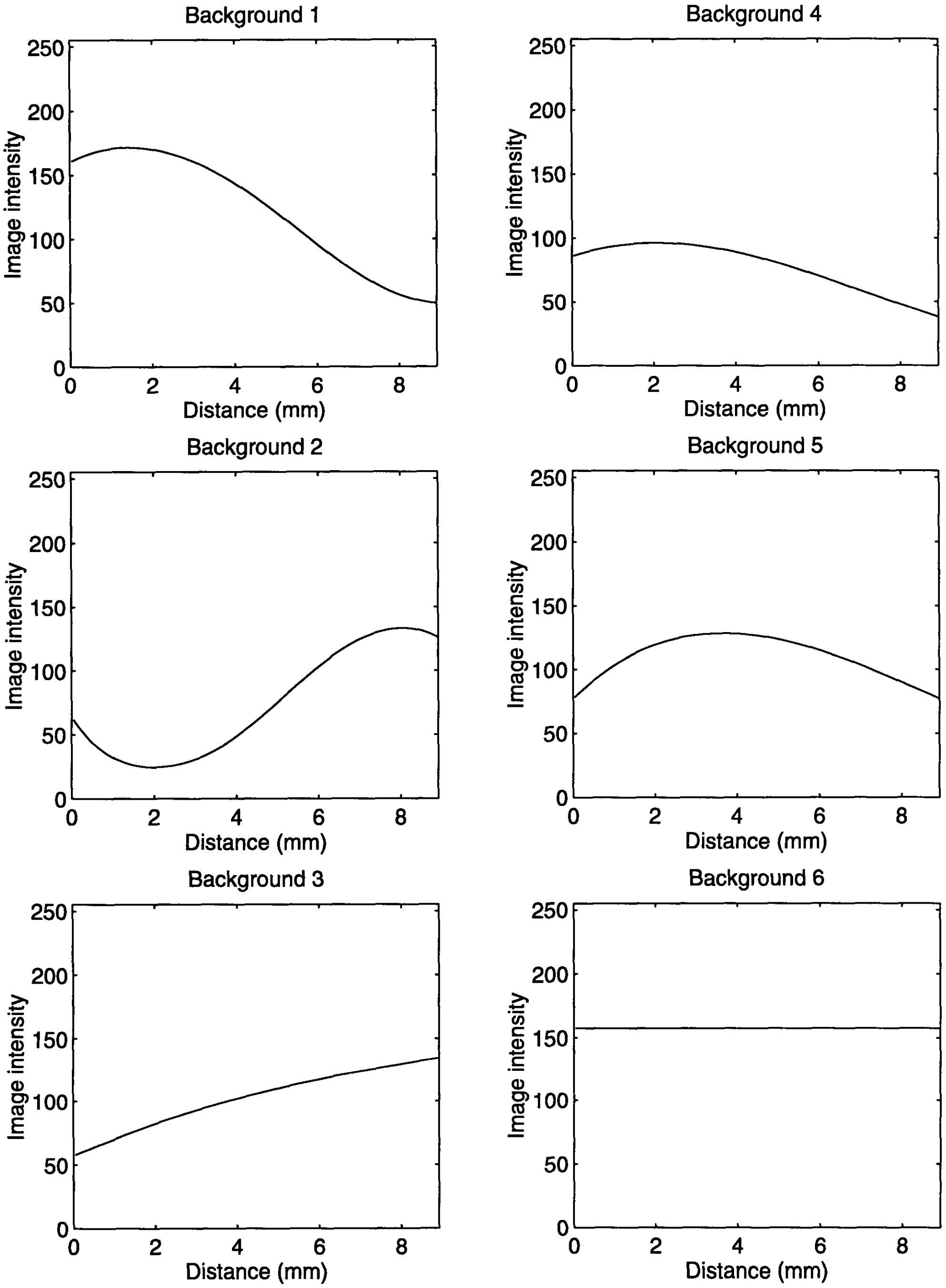

Figure 4-15: Simulated angiographic background profiles used to investigate the effect of background intensity on diameter estimation when the imaging system parameters are known.

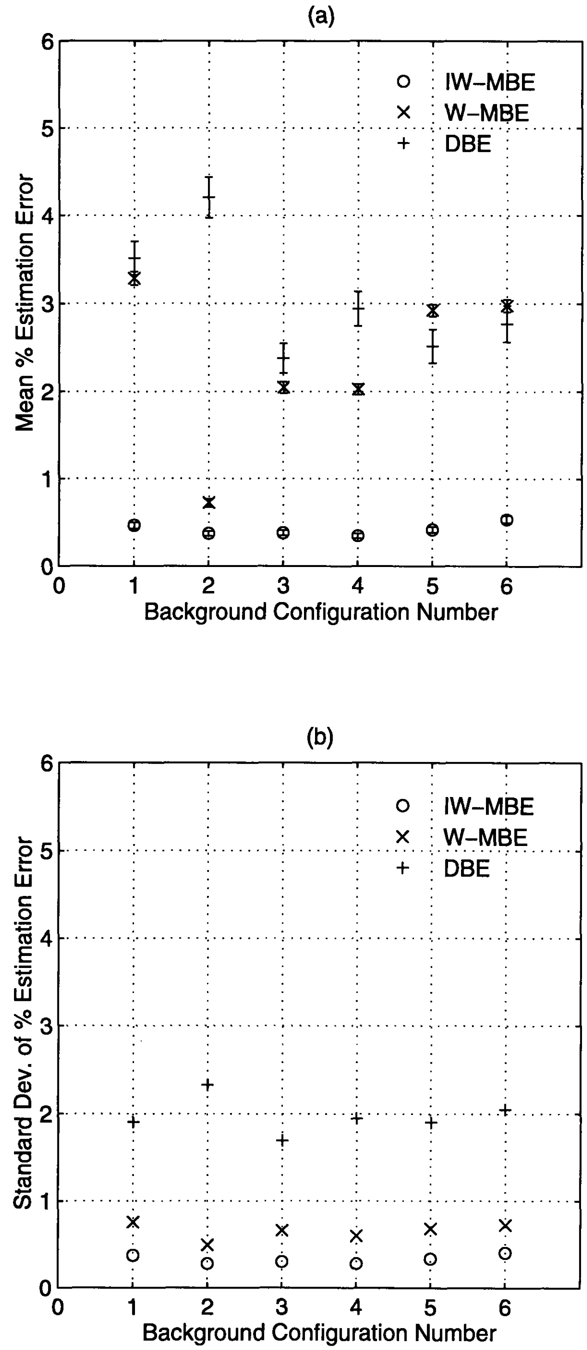

Figure 4-16: Results from measuring a large 3.0mm diameter vessel image under varying background intensity projections. The correct imaging system parameters were assumed to be known for these simulations, and the simulated backgrounds approximated those observed clinically. The background intensity profiles associated with each background configuration number are shown in Figure 4-15. (a) Mean normalized diameter estimation error from IW-MBE, W-MBE and DBE for different backgrounds. (b) Standard deviation of the normalized diameter estimation errors under varying background conditions.

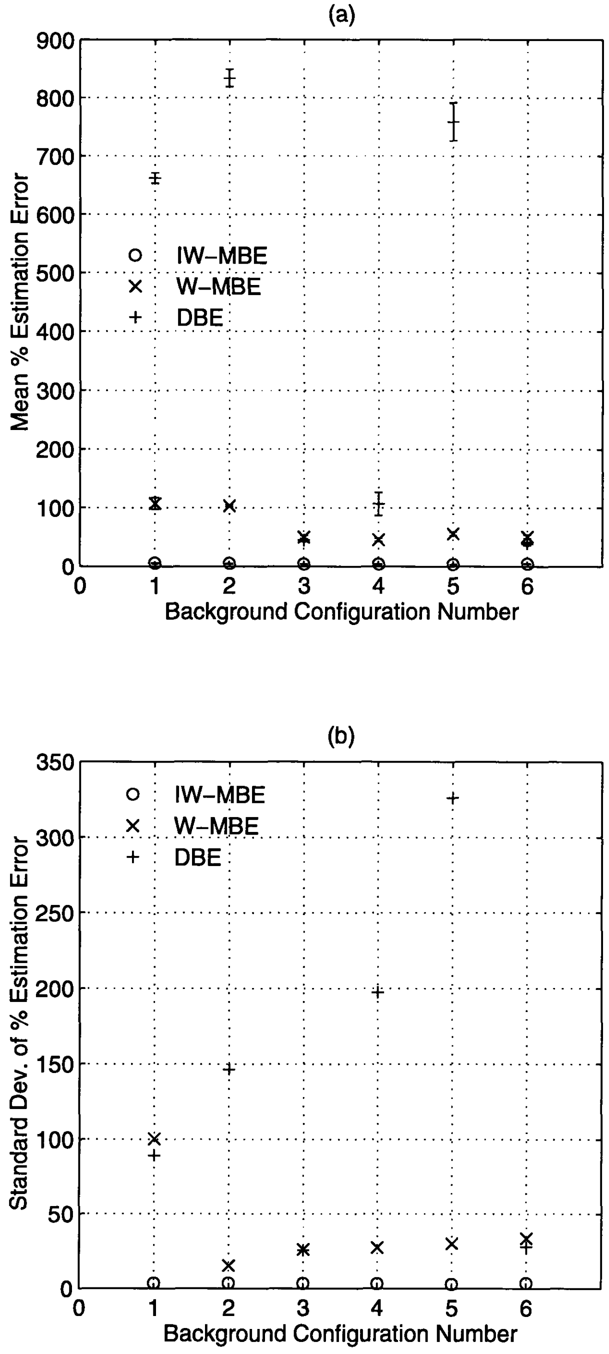

Figure 4-17: Results from measuring a small 0.5mm diameter vessel image under varying background intensity projections. The correct imaging system parameters were assumed to be known for these simulations, and the simulated backgrounds approximated those observed clinically. The background intensity profiles associated with each background configuration number are shown in Figure 4-15. (a) Mean normalized diameter estimation error from IW-MBE, W-MBE and DBE for different backgrounds. (b) Standard deviation of the normalized diameter estimation errors under varying background conditions.

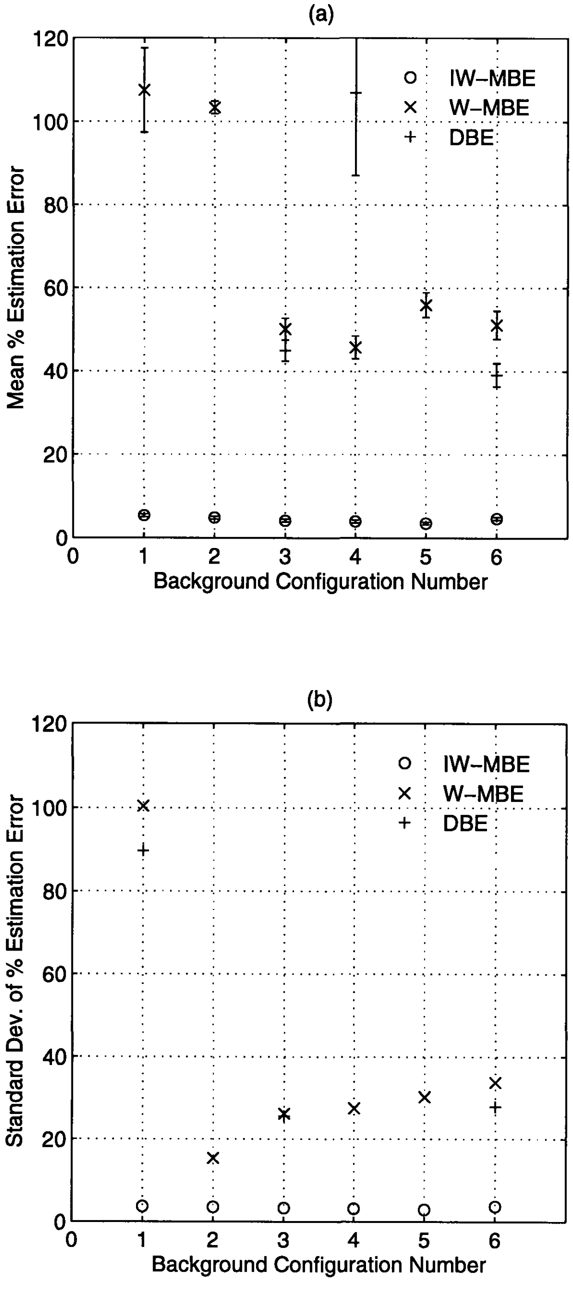

Figure 4-18: Close-up view of the measurement results shown in Figure 4-17 for a 0.5mm diameter vessel superimposed on varying background projections. The background intensity profiles associated with each background configuration number are shown in Figure 4-15. (a) Mean normalized diameter estimation error from IW-MBE, W-MBE and DBE for different backgrounds. (b) Standard deviation of the normalized diameter estimation errors under varying background conditions.

the measurement variability stayed approximately constant. DBE estimation quality was slightly poorer than W-MBE in terms of bias while the standard deviation in the normalized error was slightly greater than twice that of W-MBE. DBE estimation also showed performance sensitivity to background profile intensity variations.

The results for the 0.5mm vessel simulations show that the IW-MBE estimation bias and variability were the lowest of the estimators tested. The measurement bias of about 5% and standard deviation of approximately 4% were higher than observed in the large vessel studies, however this is expected because of the more favorable signal-to-noise conditions associated with the 3.0mm vessel. These bias and reproducibility values also appeared to be insensitive to the changes in background intensity that were examined. The results for W-MBE and DBE were significantly poorer. The W-MBE estimation bias and standard deviation were sensitive to the background profile shape — the bias values ranged between about 45% and 110%, whereas the the standard deviation values ranged between 15% and 90%. DBE performance was extremely sensitive to background profile shape. Its performance was comparable with W-MBE for a few backgrounds, and was significantly worse for others. The estimation error bias ranged from 40% to almost 850% of the true diameter, while the standard deviation in the estimates ranged from about 25% to 325%. The large estimation errors encountered by DBE may be explained by the fact that when the vessel profile is small and the variations in background intensity are relatively larger, the 'vessel edges' detected by DBE will actually be detected in the background rather than in at the real vessel borders.

These results indicate that under the conditions simulated, IW-MBE provides the best diameter estimates, especially for small vessel quantitation, in terms of low sensitivity to background profile shape and also in terms of the small magnitudes of the resulting estimation bias and variability.

4.5.4 Effect of imaging parameter mismatch

Having investigated the performance of diameter estimation when the imaging parameters are known precisely, we now consider the case where they are known (i.e. they are not estimated), but are incorrect. A study of modelling mismatch in this manner allows us to make quantitative statements about the robustness/sensitivity of IW-MBE to deviations of each imaging parameter, and may also provide insight into the maximum tolerable

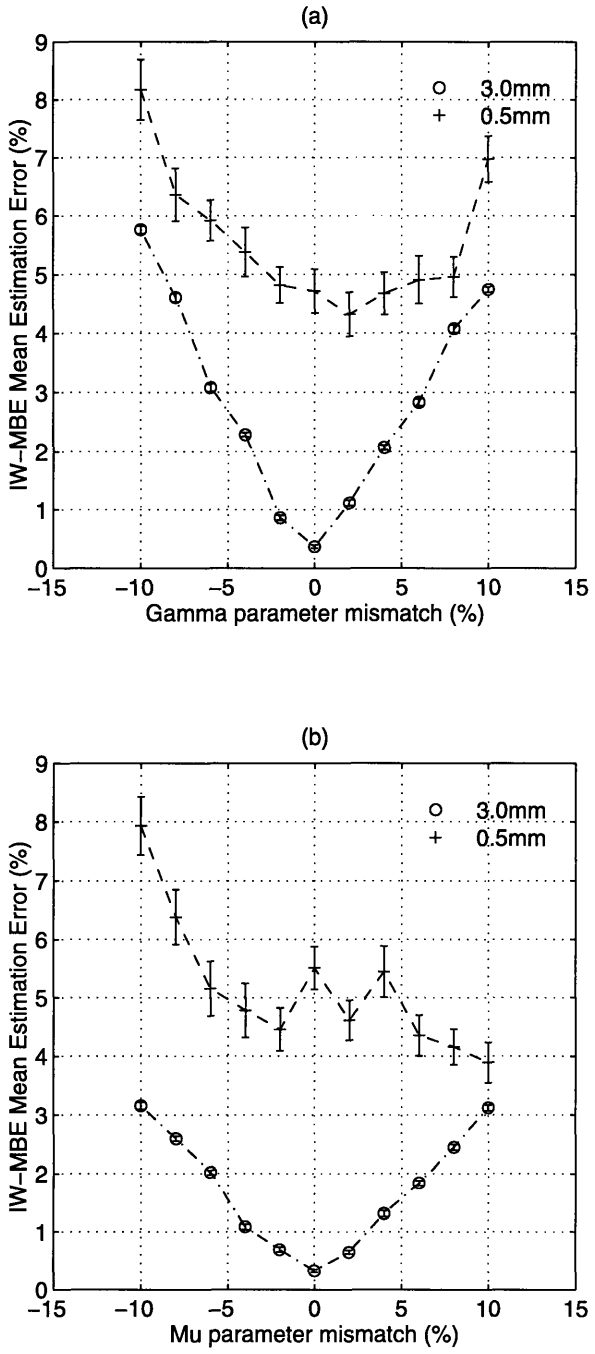

Figure 4-19: IW-MBE estimation performance in measuring a 3.0mm diameter vessel image and a 0.5mm diameter vessel image when the imaging system parameters were known, but incorrect. The error bars represent the size of one standard deviation in the measures. (a) Mean normalized estimation error as a function of the mismatch between the assumed value of the imaging system scaling, Γ, and its true value. (b) Mean normalized estimation error as a function of the mismatch between the assumed value of the imaging system attenuation, μ, and its actual value.

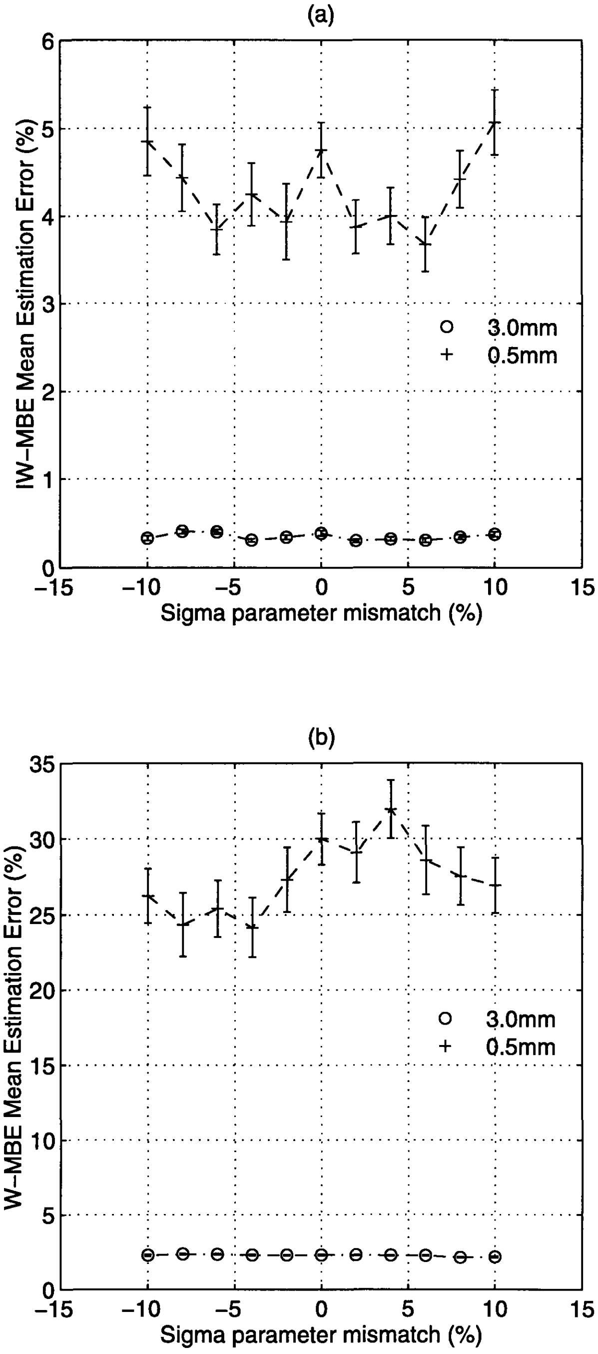

Figure 4-20: Diameter estimation performance in measuring a 3.0mm diameter vessel image and a 0.5mm diameter vessel image when the imaging system parameters were known, but incorrect. The error bars represent the size of one standard deviation in the measures. (a) IW-MBE mean normalized estimation error as a function of the mismatch between the assumed value of the imaging system blur, σ, and its true value. (b) W-MBE mean normalized estimation error as a function of the mismatch between the assumed value of the imaging system blur, σ, and its actual value.

perturbations which still result in acceptable estimator performance.

In these experiments, vessel projections were simulated corresponding to a 3.0mm and a 0.5mm diameter artery. The imaging parameters were $\Gamma = 36$, $\mu = 0.3$, and $\sigma = 0.2$mm. The background was constant across all images ($b_0 = -1.0$, with higher-order coefficients set to zero), and the vessel centerlines were positioned at $c_n = 4.0$mm. The noise intensity used was $\Lambda_\nu = 9$, resulting in SNR values of 23.4dB and -1.2dB respectively for the 3.0mm and 0.5mm diameter vessel projections. These signal-to-noise conditions are roughly comparable to those from actual x-ray images. The vessel and background parameters were estimated for each vessel diameter, using 100 noisy intensity scanlines for each case. Unlike the simulation experiments described previously, the imaging system parameters provided to the intensity-width estimation step were systematically perturbed between $\pm 10\%$ of their true values. Only one imaging parameter, Γ, μ, or σ was perturbed at a time, leaving the other two imaging parameters fixed at their correct values. In addition, we investigated the effect of perturbing the blurring σ used for W-MBE, to compare the resulting performance with that of IW-MBE for identical perturbations in this parameter. The initialization of the unknown vessel and background parameters for the model-based estimators was carried out in the same way as outlined in previous experiments. Figures 4-19 and 4-20 show the means and standard deviations of the performance metric in Equation 4.17 as functions of imaging parameter mismatch.

From the Γ mismatch results in Figure 4-19a, we can see that as the magnitude of the perturbation away from the true Γ parameter value increased, the mean normalized errors in measuring the 3.0mm and 0.5mm diameter vessels increased (these error curves are roughly convex in shape). For both vessel sizes, the corresponding measurement variability, as reflected by the error bar lengths, stayed relatively constant as a function of the perturbation. The results for the 3.0mm vessel showed a steeper curvature as perturbation magnitude increased than those for the small 0.5mm vessel. This indicates greater sensitivity of measurements in large diameter vessels to errors in the Γ value that is used. As expected, the normalized mean estimation errors for the large 3.0mm vessel (associated with higher SNR) were lower than those for the 0.5mm vessel (associated with low SNR). It is important to note that even at the extremes of Γ perturbation, the IW-MBE estimation bias for the 0.5mm vessel was lower than 10%, which is about 3 times smaller than the bias from W-MBE, and almost 4 times lower than that from DBE. Furthermore, our

3.0mm diameter vessel simulations suggest that the Γ mismatch must not exceed $\pm 5\%$ if large diameter measurement performance is to be comparable with that of W-MBE or DBE (these other estimators produced mean estimation errors of approximately 3% for this large vessel diameter, as shown in Figure 4-14).

Figure 4-19b shows the mean percent diameter measurement error as increasing mismatch is introduced into the value of attenuation μ used in IW-MBE. As expected, measurement errors were lower for large vessel measurement than for small vessel measurement. Interestingly, as μ mismatch increased from 0% towards remained relatively level. This was an unexpected result since increasing the attenuation above its true value should lead to diameter underestimation and therefore to an increasing mean estimation error. The 0.5mm measurement error for increasingly negative parameter perturbations led to rising estimation errors as was expected. The range and perturbation sensitivity of the estimation bias observed in these attenuation mismatch simulations on a narrow vessel were comparable to those found earlier for the same range of percentage mismatch in the scaling parameter Γ. Measurement results from the 3.0mm vessel showed increasing error for increasing percentage perturbations in the attenuation. The curvature of this curve is shallow compared to that observed for the Γ mismatch results, indicating a lower sensitivity of IW-MBE performance in large vessels to mismatch in the attenuation parameter μ. Unlike for the Γ mismatch simulations, the mean measurement errors from IW-MBE were lower than those from W-MBE and DBE for the entire range of μ perturbations introduced.

IW-MBE and W-MBE mean estimation error results as functions of mismatch in the blurring parameter σ are shown respectively in Figures 4-20a and 4-20b. The range of percentage mismatch studied for the blurring parameter corresponds to σ values between 0.18mm and 0.22mm when its actual value is 0.2mm. Over this range, the point spread function width does not change very significantly. As a result, both model-based techniques showed relatively constant performance as a function of the σ mismatch. Diameter estimation quality was better in the large 3.0mm vessel than the narrow 0.5mm vessel. These results also reinforce our earlier findings which show lower estimation error for model-based estimation using both profile intensity and width than that using width information alone. These model-based results are better than those found for derivative-based estimation in Figure 4-13.

4.5.5 Remarks

These experiments have explored IW-MBE estimation performance issues assuming *a priori* knowledge of either the exact or slightly mismatched parameter values of the imaging system model. The results suggest that IW-MBE outperforms W-MBE and DBE over the entire range of vessel sizes tested. The performance improvement is particularly obvious in small vessel quantitation. These simulations also show that this new approach is robust to a variety of different imaging noise conditions and background intensity profiles. Our findings thus far represent the best possible performance of IW-MBE when the estimation model and reality are perfectly matched. Our imaging parameter mismatch experiments demonstrate that IW-MBE is sensitive to the imaging parameter values used in estimation. Since the true imaging parameter values are never known *a priori* in any given clinical setting, it is essential that we probe the accuracy with which they can be estimated. We shall explore this issue in the following set of simulation experiments which treat the imaging system parameters as a set of unknowns which must be estimated from a calibration structure of known shape and diameter, under a variety of simulated imaging conditions.

4.6 Estimation of imaging parameters alone

4.6.1 Effect of imaging parameter initialization

Since the imaging system parameters have not, to our knowledge been previously treated as an additional set of unknowns, it is important to characterize the sensitivity of our intensity-width dependent estimator to the choice of initial conditions used. In these experiments, we systematically perturbed the initial conditions for scaling Γ, attenuation μ and blurring σ between +100% and -90% of their actual values used in calibration image generation.

The simulated datasets used were scanlines of a 5.0mm (r = 2.5mm) and a 2.0mm (r = 1.0mm) diameter cylindrical calibration structure, and were generated using the same procedure as that for simulating arterial vessel projections. The true imaging parameters used in the synthesis step were $\Gamma = 36$, $\mu = 0.3$, and $\sigma = 0.2$mm. The simulated backgrounds were flat ($b_0 = -1.0$, with the other background coefficients set to zero), and the calibrator centerline positions were fixed at $c_n = 4.0$mm. The noise intensity was fixed at $\Lambda_\nu = 9$, which corresponds to an SNR of 28.8dB for the 5.0mm structure and 18.5dB

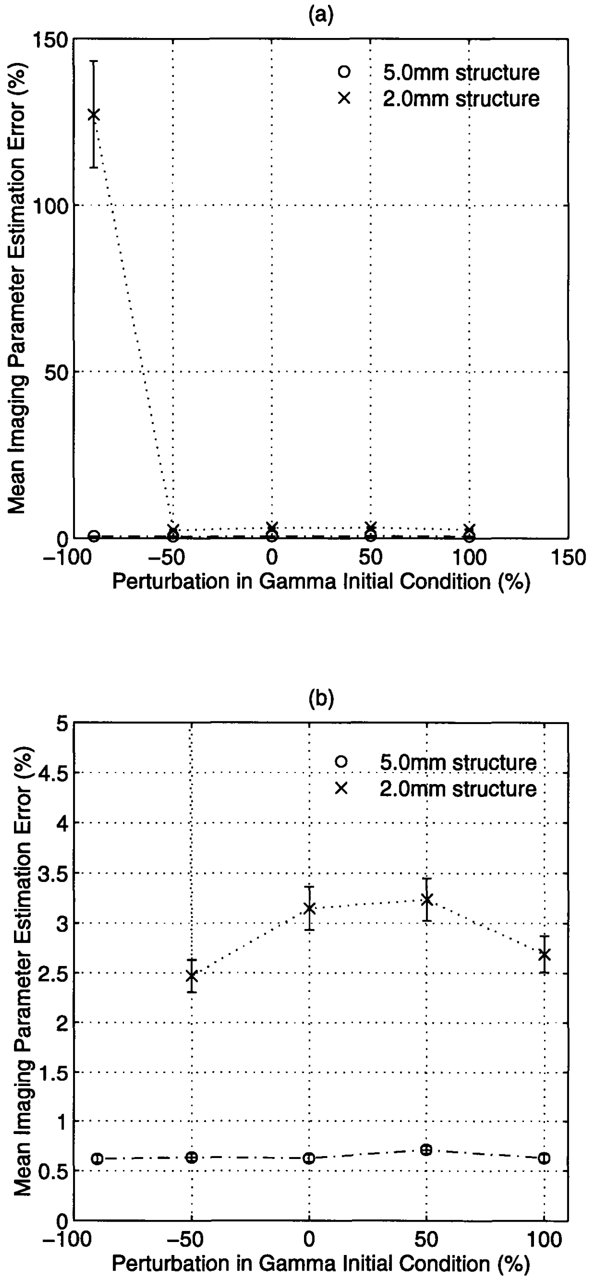

Figure 4-21: (a) Imaging parameter estimation performance as a function of mismatch between the scaling, Γ, initial condition and the actual value used for image synthesis. Calibration performance was assessed using both a large 5.0mm diameter structure and a smaller 2.0mm structure. (b) Close-up of (a) to show greater detail in the results. The error bars represent the size of one standard deviation in the measures.

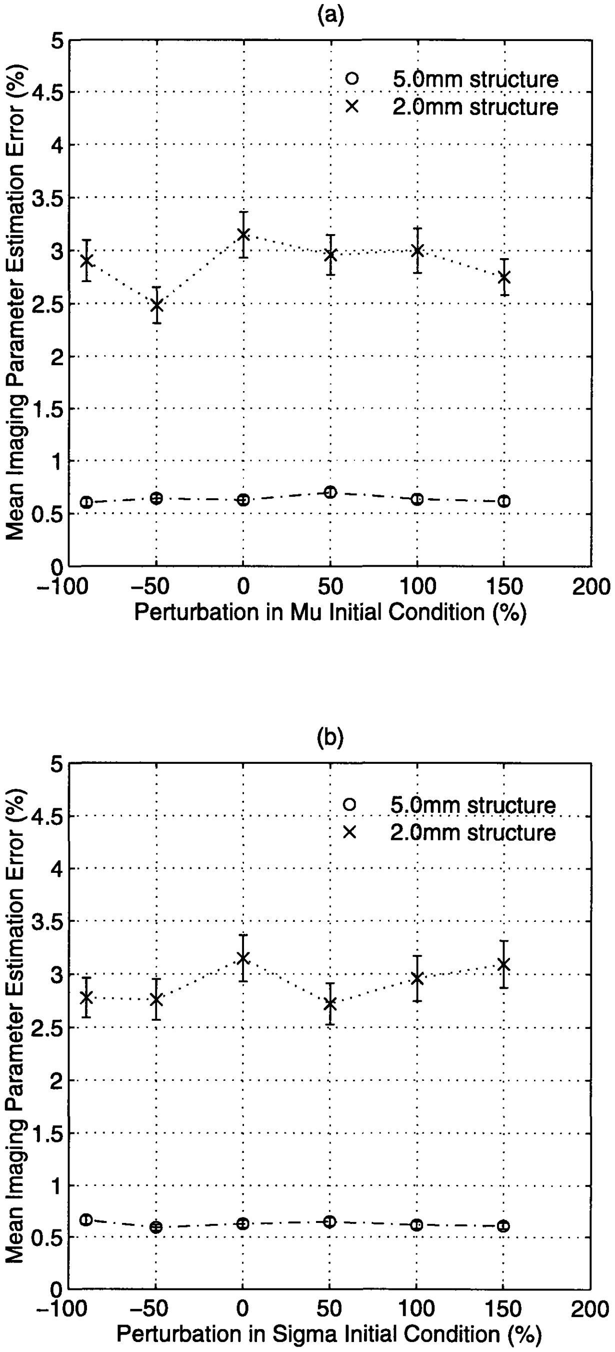

Figure 4-22: (a) Imaging parameter estimation performance as a function of mismatch between the attenuation, μ, initial condition and the actual value used for image synthesis. (b) Imaging parameter estimation performance as a function of mismatch between the blur, σ, initial condition and the actual value used for image synthesis. For both (a) and (b), the calibration performance was assessed using a large 5.0mm diameter structure and a smaller 2.0mm structure. The error bars represent the size of one standard deviation in the measures.

for the 2.0mm structure. The resulting calibration dataset consisted of 100 noisy scanlines representing image intensity cross-sections, each of which were 200 elements in length (this translates into a calibration dataset with physical dimensions of about 5.0mm in length and 10.0mm in width).

Unlike vessel diameter measurements where estimation is performed on a scanline by scanline basis to determine the diameter evolution as a function of vessel length, the estimation of the imaging system parameters is performed by using multiple calibration intensity scanlines simultaneously. This is possible since the imaging parameters are spatially invariant over the image. Treating multiple intensity scanlines as a single calibration dataset provides a more reliable measure of the imaging system than would be possible by averaging together imaging parameter vectors estimated from single image scanlines.

The known calibration structure size and center position in each dataset was provided, and the initialization of background parameters was the same as that described in previous experiments. Only one imaging parameter initial value was perturbed at a time — the initial conditions for the other two imaging parameters were fixed at their correct values. For each initial condition studied, we estimated the imaging parameters corresponding to 100 noise-corrupted calibration datasets. The performance metric used to assess the quality of imaging parameter estimates was the Euclidean norm of the vector whose elements are the normalized estimation error of each imaging parameter (Γ, μ, and σ). This is given by the following equation:

$$\|\hat{\mathbf{I}}\| \times 100 \tag{4.18}$$

where $\hat{\mathbf{I}} = \left[\frac{(\hat{\Gamma}-\Gamma_{true})}{\Gamma_{true}} \;\; \frac{(\hat{\mu}-\mu_{true})}{\mu_{true}} \;\; \frac{(\hat{\sigma}-\sigma_{true})}{\sigma_{true}}\right]$.

Figure 4-21 shows the IW-MBE sensitivity to mismatch in initial conditions for the scaling parameter, Γ. The plotted points represent the mean imaging parameter estimation error given in Equation 4.18. Each error bar deflection represents one standard deviation of the mean estimation error and reflect the variability in the imaging parameter estimates. The results show that calibration on a large 5.0mm diameter structure produced lower imaging parameter estimation error than that from calibration on a smaller 2.0mm diameter structure, over a very wide range of Γ initial conditions tested. Estimation in the presence of the level of noise intensity simulated, produced a mean estimation error of about 0.6% that was approximately constant as a function of the Γ initial condition for the large 5.0mm diameter calibration structure. For the 2.0mm calibration datasets, a very large mean estimation error of about 130%±20% was observed when the initial condition was only 10% of the true Γ value used. This indicates that large underestimates of the Γ initial condition, to be used for calibrating on a 2.0mm diameter structure, are highly detrimental to the quality of the resulting imaging parameter estimates. For the remaining range of initial condition perturbations studied, the mean estimation error from using the small diameter dataset resulted in a roughly constant error at 2.8%.

IW-MBE sensitivity to mismatch in initial conditions for the attenuation parameter, μ, and the blurring parameter, σ, are respectively shown in Figures 4-21a and 4-21b. Unlike for the Γ initial condition sensitivity experiments on the 2.0mm diameter calibration datasets, these results suggest that there are no obvious regions of initial condition values for either μ or σ over which significant estimation errors can result. The estimation errors were approximately constant as a function of initial condition value, with those for calibration on a 2.0mm dataset being about 5 times higher (mean estimation error of about 2.8%) than those that resulted from using a 5.0mm diameter dataset (mean estimation error of about 0.6%).

These simulations suggest that the estimation of imaging parameters is more accurate and reliable when using a 5.0mm diameter structure as opposed to a narrower 2.0mm diameter structure. The sensitivity of IW-MBE to a wide range of imaging parameter initial conditions seems to be relatively low. The exception to this is calibration on a narrow structure while using an initial Γ value that is very much smaller than the true quantity. These results suggest that conservative initial conditioning of Γ, μ and σ using typical quantities (which also lie in the middle of the range of possible values) should produce reliable imaging parameter estimates.

From our earlier mismatch simulations which assumed that the imaging parameters were known, only one of which was incorrect, imaging parameter estimation errors on the order of 3% would translate into relatively small errors in vessel diameter measurement. In these simulations however, none of the estimated parameters was precisely correct, thus it will be necessary to study how the observed imaging parameter estimation errors propagate into the vessel parameter estimation step. We will consider all such 'end-to-end' scenarios in Section 4.4.5.

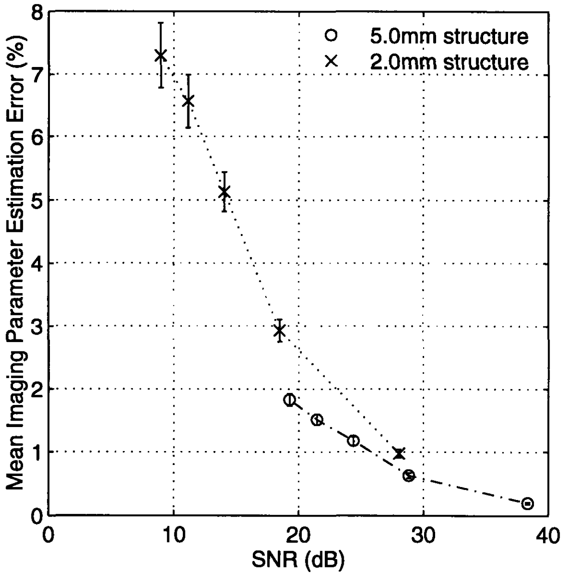

Figure 4-23: Imaging parameter estimation performance as a function of varying signal-to-noise conditions. Calibration performance was assessed using both a large 5.0mm diameter structure and a smaller 2.0mm structure. The error bars represent the size of one standard deviation in the mean imaging parameter estimation error.

4.6.2 Effect of noise level

In these simulations, we investigated the effects of increasing noise intensity on the resulting imaging system parameter estimates from IW-MBE. The calibration images were generated using the same modelling parameters: $\Gamma = 36$, $\mu = 0.3$, $\sigma = 0.2\text{mm}$, $b_0 = -1.0$ (all higher-order background coefficients set to zero), and $c_n = 4.0\text{mm}$. Two calibration datasets corresponding to 5.0mm and 2.0mm diameter structures were tested. The noise intensity applied to these datasets was varied from 1 to 81, which translates into SNR values between 19.3dB and 38.4dB for the 5.0mm calibration structure, and between 8.9dB and 28.0dB for the 2.0mm structure. Under typical noise intensity levels ($\Lambda_\nu \sim 9$), the SNR for a 5.0mm calibration dataset would be about 28dB, and that for a 2.0mm calibration structure would be approximately 18dB. At each level of noise intensity considered, we examined 100 noise-corrupted calibration datasets, and estimated the imaging parameters from each of these realizations. Initialization of the estimation step was performed in the same manner as earlier described in our investigation of IW-MBE initial condition sensitivity.

The noise sensitivity results for these simulations are shown in Figure 4-23. Over the range of noise intensities simulated, the mean and standard deviations of the imaging parameter estimation error were higher when using a 2.0mm calibration dataset than when using the 5.0mm dataset. Over the range of SNR values for which data was available from both calibration datasets (SNRs between 16dB and 27dB), the mean error curve for calibration on a 2.0mm structure was steeper as a function of decreasing SNR than that for calibration on a 5.0mm structure. This indicates that the noise sensitivity of imaging parameter estimation will increase when smaller calibration structures are used. The trend of decreasing estimation performance as a function of decreasing SNR comes as no surprise. However, it is encouraging that even under the most adverse noise conditions simulated (which is far worse than we would expect from a typical angiogram), the estimation error, even for calibration on the 2.0mm dataset, was less than 8%. Judging from our earlier mismatch simulations in Section 4.4.3, and from the relatively low imaging parameter estimation error observed here, we have a reasonable hope of favorable performance from the subsequent vessel diameter estimation step, when the IW-MBE algorithm is carried through from beginning to end.

4.6.3 Effect of imaging system operating points

In this set of experiments we were interested in determining the sensitivity of estimation quality to variations in the imaging system operating points. In practice, such changes in imaging operating points would occur if different imaging equipment is used, or if the imaging conditions during an angiographic session change. As before, calibration datasets were simulated for a 5.0mm and for a 2.0mm diameter structure. The background intensities were flat ($b_0 = -1.0$) and the centerline positions were fixed for all images ($c_n = 4.0$mm). The noise variance was fixed at $\Lambda_\nu = 9$, corresponding to SNR values of 28.8dB for the 5.0mm diameter calibration datasets, and 18.5dB for the 2.0mm diameter datasets. The imaging parameter operating points used in image synthesis were varied one at a time, and the default imaging parameter values were $\Gamma = 36$, $\mu = 0.3$ and $\sigma = 0.2$mm. The Γ operating points examined were 32.1, 45.0, and 51.4; the μ values investigated were 0.15, 0.2, and 0.4; the σ operating points were 0.20mm, 0.25mm, and 0.3mm. The values for each operating point studied are also reflected in the abscissa of the corresponding result plot in Figure 4-24. Under each operating point condition, we estimated the imaging parameters from 100 noisy calibration datasets. The initialization of the IW-MBE algorithm was performed as previously described.

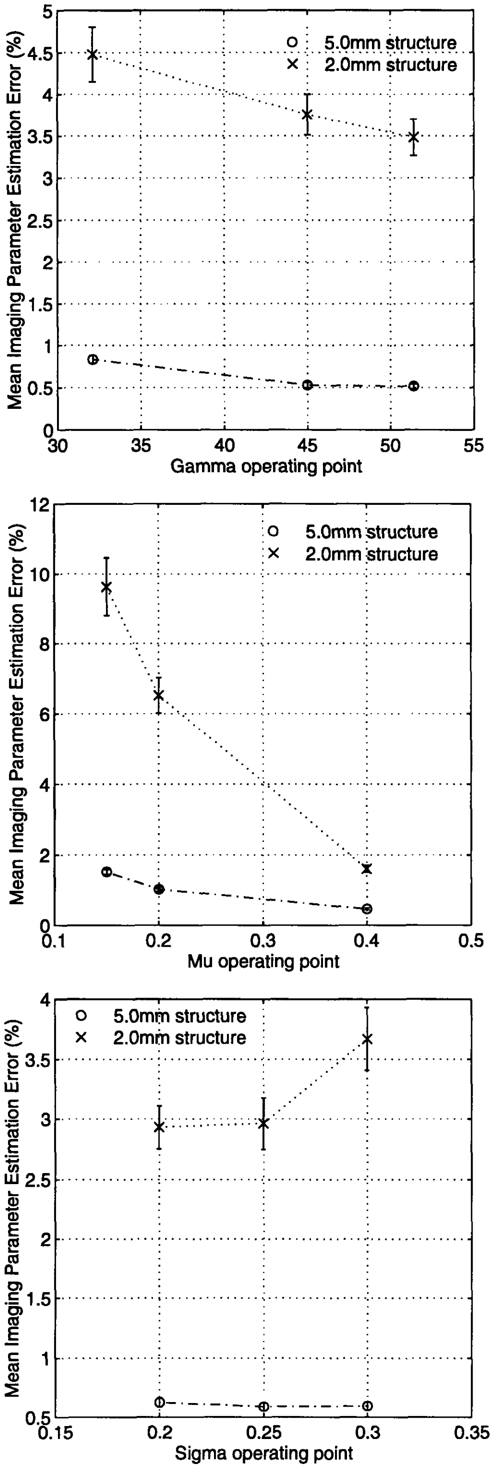

Figure 4-24: Imaging parameter estimation performance as a function of varying operating point parameters. The imaging parameter operating point varied in each plot is indicated in the abscissa. Calibration performance was assessed using both a large 5.0mm diameter structure and a smaller 2.0mm structure. The error bars represent the size of one standard deviation in the measurements.

Figures 4-24a, 4-24b, and 4-24c respectively show the variation in estimation performance as the Γ, μ and σ operating points are varied. As in previous plots, the plot points represent the mean imaging parameter estimation error and the error bar deflections denote one standard deviation of the mean estimation error. The results for the Γ operating point experiment showed little change in the mean error as Γ increased from 32.1 to 51.4. The total change was less than 0.5% when calibration was performed using a 5.0mm dataset, and was only about 1.0% for calibration on a 2.0mm diameter structure. The trend of increasing error for decreasing values of Γ was expected since reduction of the scaling parameter decreases the size of the signal (the intensity of the calibration structure projection), which worsens the SNR and makes parameter estimation more difficult. As in previous experiments, calibration on a large 5.0mm structure produces more accurate estimates than that on a narrower 2.0mm structure.

The data in Figure 4-24b showed degrading estimation performance as the operating point for the attenuation, μ, decreased, for both the 5.0mm and 2.0mm calibration datasets. This trend is explained by decreasing μ producing smaller signal intensities and poorer SNR conditions. Over the wide range of μ operating point values simulated, the change in mean estimation error for the 5.0mm calibration dataset was about 1%, while that for the 2.0mm dataset was roughly 8%. The average and standard deviation of the estimation error was greater in the 2.0mm dataset than in the 5.0mm one. The slope of the mean error curves suggests that greater sensitivity to the attenuation parameter operating point occurs when calibrating on the 2.0mm diameter structure.

The σ operating point appeared to have little effect on estimation quality over the range of values explored (as shown in Figure 4-24c). The mean error was level at 0.6% for the 5.0mm calibration dataset estimates, while that for the 2.0mm dataset showed slightly greater sensitivity, rising from about 3.0% to 3.6% as σ increased from 0.2mm to 0.3mm. As expected, the overall estimation error was larger for calibration on the 2.0mm structure than for the 5.0mm structure.

IW-MBE sensitivity to variations in imaging parameter operating points appear to depend upon the effect that these changes have on signal-to-noise conditions. Of the operating points studied, the mean estimation errors observed were highest for the attenuation parameter μ. This is due in part to the wide range of attenuation values used, which in turn had significant effects on signal amplitude. The results from these simulations (from both calibration datasets) suggest that imaging parameter estimation errors remain relatively low even when the imaging conditions are varied. These results also indicate that IW-MBE may be reliably used for different angiographic imaging systems, and that it may be robust to fluctuations in imaging conditions which occur during an angiographic session.

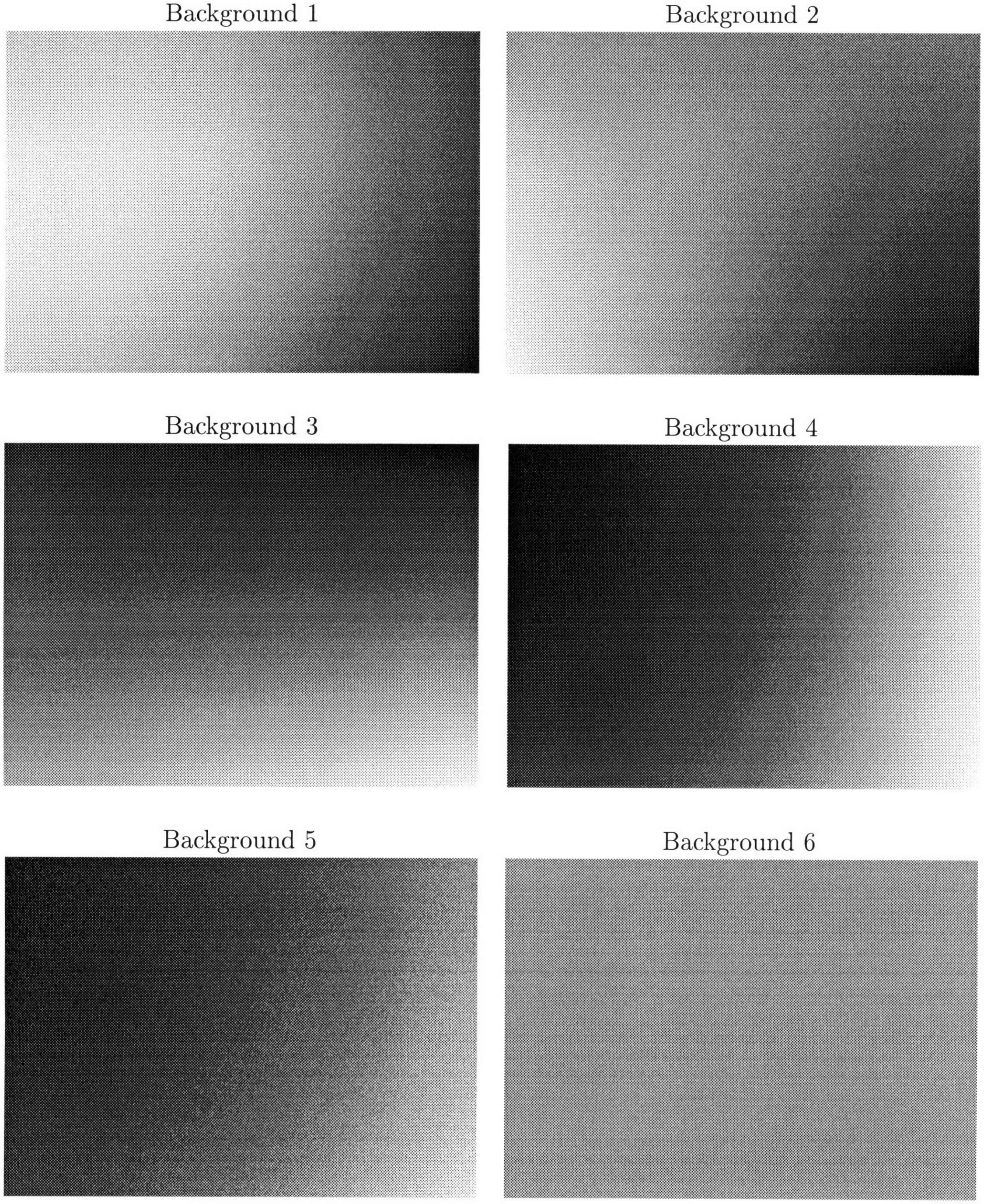

Background 1

Background 2

Background 3

Background 4

Background 5

Background 6

Figure 4-25: Simulated angiographic background projections used to investigate the effect of background variation on imaging parameter estimation when the true imaging parameters are unknown.

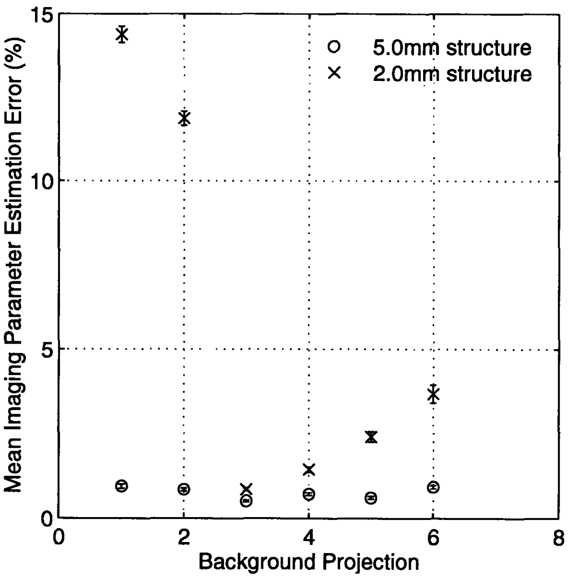

Figure 4-26: Imaging parameter estimation performance as the background projection intensities are varied according to the configurations shown in Figure 4-25. Calibration performance was assessed using both a large 5.0mm diameter structure and a smaller 2.0mm structure. The error bars represent the size of one standard deviation in these measures.

4.6.4 Effect of simulated angiographic backgrounds

Recall that for imaging parameter estimation, we can simultaneously use multiple consecutive image scanlines since the parameter values are spatially invariant. These scanlines consitute a two-dimensional calibration dataset, and we can treat the background in this dataset as a continuous two-dimensional polynomial function (which improves estimation performance). Thus, the background parameters in this experiment correspond to the coefficients of a two-dimensional second-degree polynomial function. This is different from our earlier vessel parameter estimation experiments in which the datasets were one-dimensional profiles, and the background parameters correponded to 1D polynomial functions.

In these experiments, the angiographic background intensities for the calibration images were varied. The 2D backgrounds studied are approximations to those observed in clinical angiograms. These configurations are shown in Figure 4-32. The calibration datasets were simulated for 5.0mm and 2.0mm diameter structures. The modelling parameters used were the same for these images: $\Gamma = 36$, $\mu = 0.3$, $\sigma = 0.2$mm, $c_n = 4.0$mm, and $\Lambda_\nu = 9$. Initializing the imaging parameter estimation step as before, we calibrated on 100 noisy datasets under each of the simulated background projections.

The data in Figure 4-26 shows that overall, imaging parameter estimates from the noisy 5.0mm datasets were more accurate and more reproducible than those values from the noisy 2.0mm calibration datasets. By virtue of their larger diameter, the 5.0mm diameter datasets possess higher SNR than the 2.0mm data. This results in the higher quality of estimates observed when using these larger calibration structures. The mean estimation errors were slightly less than 1% for calibration on the 5.0mm structure, and were also insensitive to the background configuration. The mean estimation errors from the 2.0mm calibration datasets showed greater sensitivity to the background intensity, ranging from slightly below 1% to almost 15%. These findings reinforce our earlier findings that a large diameter calibration structure should be used in order to obtain accurate measurements of the imaging system parameters.

4.6.5 Remarks

Our simulation results thus far suggest that the unknown imaging chain parameters may be reliably extracted from calibration structures of known size and shape. Such estimation is reasonably robust to varying initialization points, noise levels, operating points, and background intensity configurations. Calibration on larger diameter structures also yields more accurate imaging parameter estimates than calibration using narrower diameters. Since imaging parameter estimates are only a stepping stone to realizing the real goal of obtaining accurate arterial diameter measurements, it is essential that we investigate how errors from the imaging parameter estimation step affect the subsequent vessel diameter estimation step. This is the topic of the following section.

4.7 Estimation of vessel parameters given unknown imaging parameters

For these simulations, we investigated the 'end-to-end' IW-MBE estimation problem when both the imaging characteristics and the vessel related parameters are unknown. We used each set of imaging parameter estimates obtained in Section 4.4.4 (under varying imaging conditions), to measure simulated vessel diameters from noisy intensity profiles of a wide 3.0mm diameter artery, and a narrow 0.5mm diameter artery. This was repeated for each of the initialization, noise, operating point and background configuration imaging system calibration results. The 3.0mm and 0.5mm vessel profiles were simulated using the same imaging, position, and background model parameters as those outlined in the description of each of these calibration experiments. The noise variances in these vessel profiles were also identical to those in the calibration datasets. For most simulations, the noise intensity level was fixed at $\Lambda_\nu = 9$, which corresponds to SNRs of 23.3dB for the 3.0mm vessel and -1.2dB for the 0.5mm vessel (when the background parameter $b_0 = -1$ and the higher order terms are zero).

4.7.1 Effect of imaging parameter initialization

Figure 4-27 shows mean estimation errors that resulted from vessel diameter measurements as the Γ initial condition was varied for the calibration step. The results for calibration on a 5.0m structure are shown in Figure 4-27a. Here we see that the means and standard deviations of the diameter estimation errors, when measuring both the large 3.0mm vessel and the small 0.5mm vessel, were low, and relatively insensitive to the Γ initialization value. The mean error was about 4.25% for the 0.5mm diameter vessel measurements, and roughly 0.4% for those from the 3.0mm vessel profiles. This result was expected since the SNR for the 0.5mm vessel was -1.2dB whereas that for the larger 3.0mm vessel was 23.4dB (the simulate noise variance, Λ_ν, was 9 for both vessel sizes). The good diameter estimation performance was unsurprising since the imaging parameter estimation errors for this simulation (Figure 4-21b) were low to begin with (the mean imaging parameter estimation error was only $\sim$ 0.6%).

The diameter measurement results in Figure 4-27b, obtained after calibration on a 2.0m diameter structure, show enormous estimation errors of about 120% ± 25% for the 3.0mm vessel, and about 250% ± 50% for the narrow 0.5mm vessel, when Γ is initialized at 10% of its true value. For this initialization point, the corresponding imaging parameter estimates were extremely poor (Figure 4-21a); these large errors propagated into the vessel measurement step to produce the large diameter estimation errors that were observed. For the other Γ initial values tested, the mean diameter errors were similar, hovering about 4.5% for the small 0.5mm profiles and about 0.5% for the large 3.0mm vessel data.

Figure 4-28 and 4-29 illustrate the vessel diameter estimation results obtained respectively for varying initial values of attenuation parameter, μ, and blurring parameter, σ. These data show similar diameter estimation errors for calibration on a 5.0mm dataset.

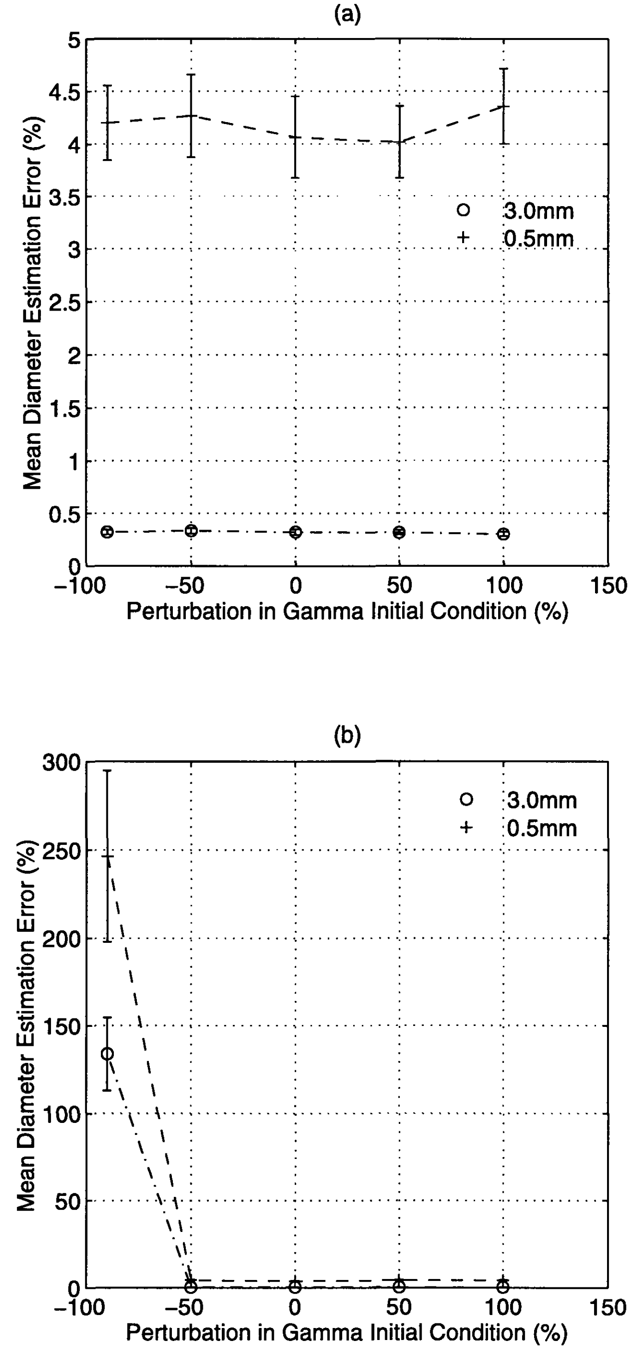

Figure 4-27: Diameter estimation performance in 3.0mm and 0.5mm diameter vessel images as a function of mismatch between the scaling, Γ, initial condition and the actual value used in image synthesis. (a) Diameter measurement results using imaging parameter calibration on a large 5.0mm diameter structure. (b) Diameter measurement results using imaging parameter calibration on a smaller 2.0mm structure. The error bars represent the size of one standard deviation in these measures.

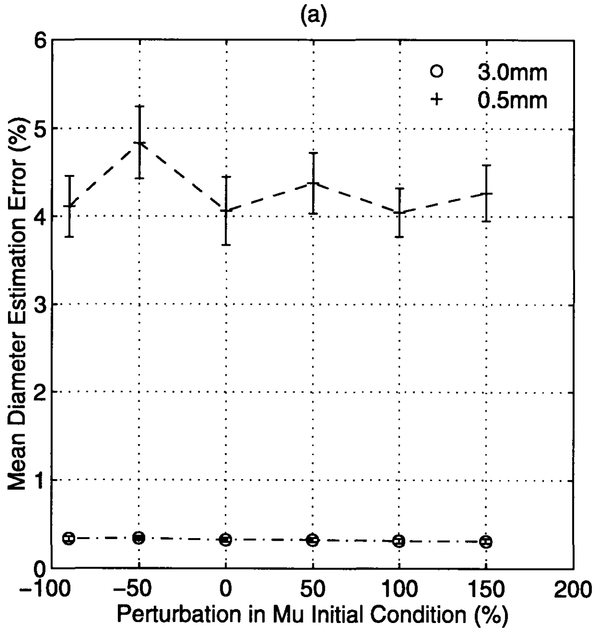

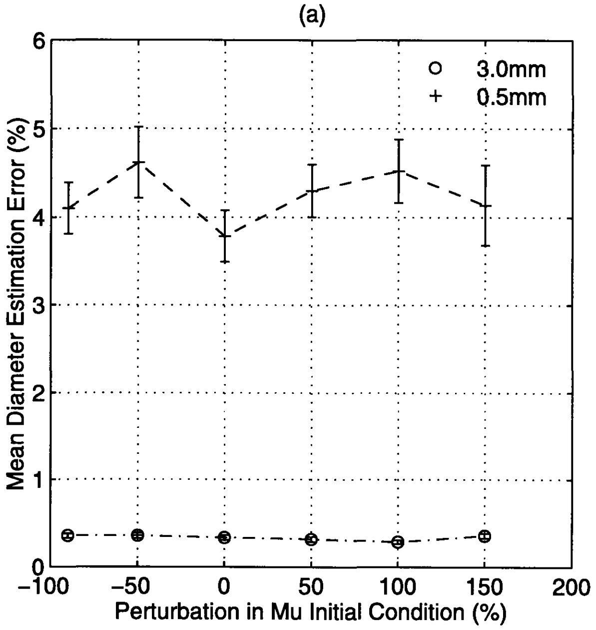

Figure 4-28: Diameter estimation performance in 3.0mm and 0.5mm diameter vessel images as a function of mismatch between the scaling, μ, initial condition and the actual value used in image synthesis. (a) Diameter measurement results using imaging parameter calibration on a large 5.0mm diameter structure. (b) Diameter measurement results using imaging parameter calibration on a smaller 2.0mm structure. The error bars represent the size of one standard deviation in the measures.

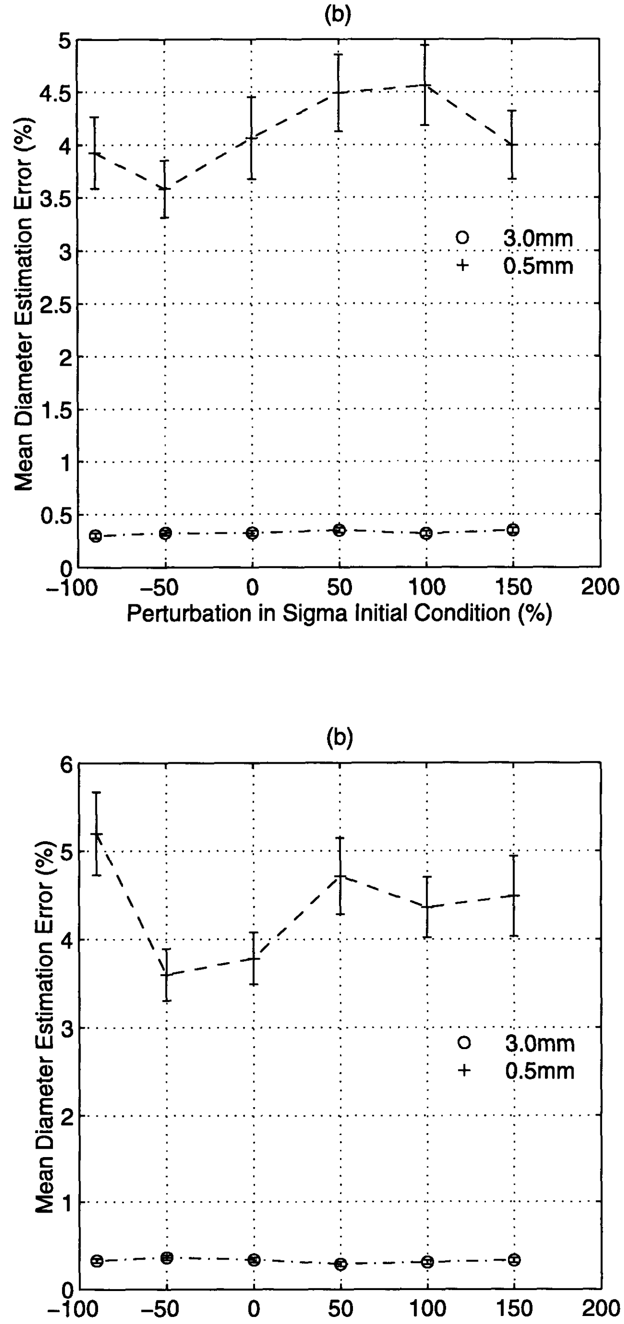

Figure 4-29: Diameter estimation performance in 3.0mm and 0.5mm diameter vessel images as a function of mismatch between the scaling, σ, initial condition and the actual value used in image synthesis. (a) Diameter measurement results using imaging parameter calibration on a large 5.0mm diameter structure. (b) Diameter measurement results using imaging parameter calibration on a smaller 2.0mm structure. The error bars represent the size of one standard deviation in the measures.

The average measurement error for a 3.0mm vessel was slightly less than 0.5% over the range of μ and σ initial conditions studied. The error was higher and more variable when measuring the 0.5mm diameter profiles. The mean error was slightly over 4%, and appeared to be relatively insensitive to initial value variations for either the attenuation or the blurring. The vessel diameter estimation error observed after calibration on a 2.0mm dataset were comparable to those obtained when using a 5.0mm calibration structure. The average error was low (less than 0.5%) , and the variability was small when measurements of a 3.0mm vessel were made. The mean errors resulting from the 0.5mm profile measurements were roughly level at slightly over 4%, and the variability in these measurements was similar to that observed when using imaging parameters estimated from the 5.0mm calibration dataset.

4.7.2 Effect of noise level

In these experiments, we used a wide range of noise variances (Λ_ν between 1 to 81), which corresponded to SNRs ranging from 32.9dB to 13.8dB for the 3.0mm vessel and from 8.3dB to -10.8dB for the 0.5mm vessel. Figure 4-30a shows the diameter measurement results for calibration on 5.0mm datasets, while Figure 4-30b shows the diameter estimation performance for 2.0mm calibration datasets. These data show that diameter estimation errors increase for increasing noise intensities, and that small vessel measurement is particularly sensistive to noise (as reflected in the steeper rise in mean estimation error as SNR falls for the 0.5mm diameter measurement results). Increasing noise levels not only obscure the vessel profile signals, making them more difficult to measure, but also increase the error in the imaging parameter estimates upon which the vessel diameter measurements are dependent.

Diameter estimates of the 3.0mm vessel using the 5.0mm calibration datasets compared against those using the 2.0mm calibration datasets showed similar results. The mean estimation error increased slightly from near 0% at the highest SNR value, to about 1% at the poorest SNR condition. Comparing the 0.5mm vessel measurement results from using a 5.0mm calibration structure against those from using a 2.0mm structure, it is interesting to observe that the diameter estimates that result are roughly comparable in terms of bias and variability. This is notable since the mean imaging parameter estimation error was significantly higher for the 2.0mm calibration datasets than for the 5.0mm calibration data

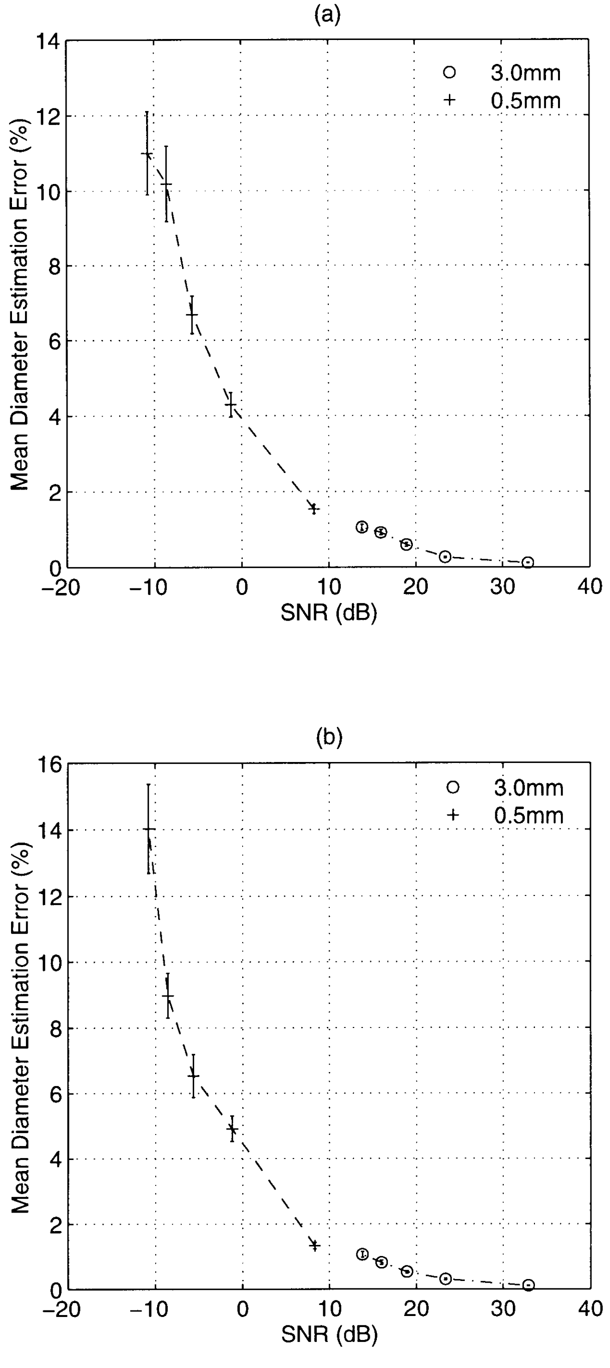

Figure 4-30: Diameter estimation performance in 3.0mm and 0.5mm diameter vessel images as a function of varying signal-to-noise conditions. (a) Diameter measurement results using imaging parameter calibration on a large 5.0mm diameter structure. (b) Diameter measurement results using imaging parameter calibration on a smaller 2.0mm structure. The error bars represent the size of one standard deviation in the measurements.

(Figure 4-23). This therefore indicates that significant errors in the imaging parameter estimates do not necessarily translate into comparable errors in diameter estimation from the vessel measurement step. It must also be noted that even under the most adverse simulated noise conditions (worse than in typical angiograms), the mean diameter estimation error for the simulated 0.5mm vessel does not exceed 16%. This therefore suggests that IW-MBE performance is significantly improved over that from W-MBE or DBE, which show mean diameter estimation errors of about 38% and 314% respectively (Figure 4-12a).

4.7.3 Effect of imaging system operating points

Figure 4-31 illustrates the vessel diameter estimation results for varying imaging system operating points. Comparing the estimation results for calibration on a 5.0mm structure against those from using a 2.0mm calibration dataset, there appears to be no significance difference between them. In both cases, measurement of the large 3.0mm vessel resulted in extremely low bias and variability. These measurements were also relatively invariant to changes in the imaging system operating points. Measurement errors for the narrow 0.5mm vessel resulted in variations in no more than 3% over the range of Γ and σ parameters investigated. The mean measurement error changed most for the range of attenuation μ values simulated. This is due to the very wide range of attenuation values studied, and also to the importance of the attenuation parameter in determining the vessel signal intensity. Increasing values of Γ and μ result in larger vessel profile intensities, and improved SNR, explaining the observed trend of decreasing mean estimation error as these imaging parameters rise. The diameter estimation error bias and variability is low for the operating point ranges investigated. Significantly, our simulation results suggest that estimation performance, particularly in narrow vessels, is significantly better than existing diameter estimators, despite variations in the simulated imaging conditions.

4.7.4 Effect of simulated angiographic backgrounds

Figure 4-32 shows the mean diameter estimation errors resulting from variation in background intensity configuration. Vessel estimates based on the use of a 5.0mm calibration dataset showed little sensitivity to background intensity changes. The average estimation error was slightly less than 0.5% for the 3.0mm diameter vessel, while that for the 0.5mm vessel was about 3.8%. The measurement variabilities as reflected by the one standard

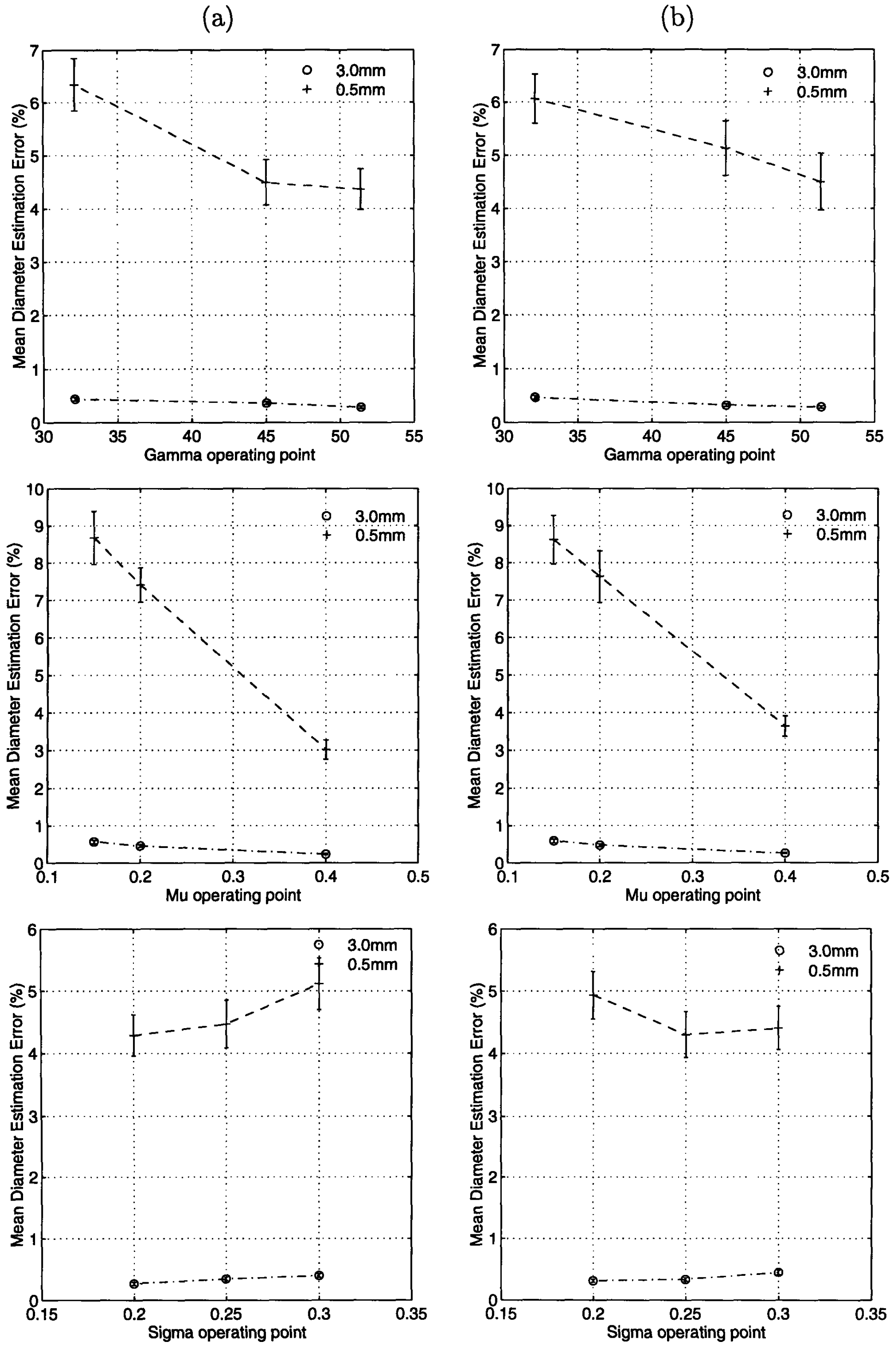

Figure 4-31: Diameter estimation performance in 3.0mm and 0.5mm diameter vessel images as a function of varying imaging system operating points. The imaging parameter operating point varied in each plot is indicated in the abscissa. (a) Diameter measurement results using imaging parameter calibration on a large 5.0mm diameter structure. (b) Diameter measurement results using imaging parameter calibration on a smaller 2.0mm structure. The error bars represent the size of one standard deviation in the measures.

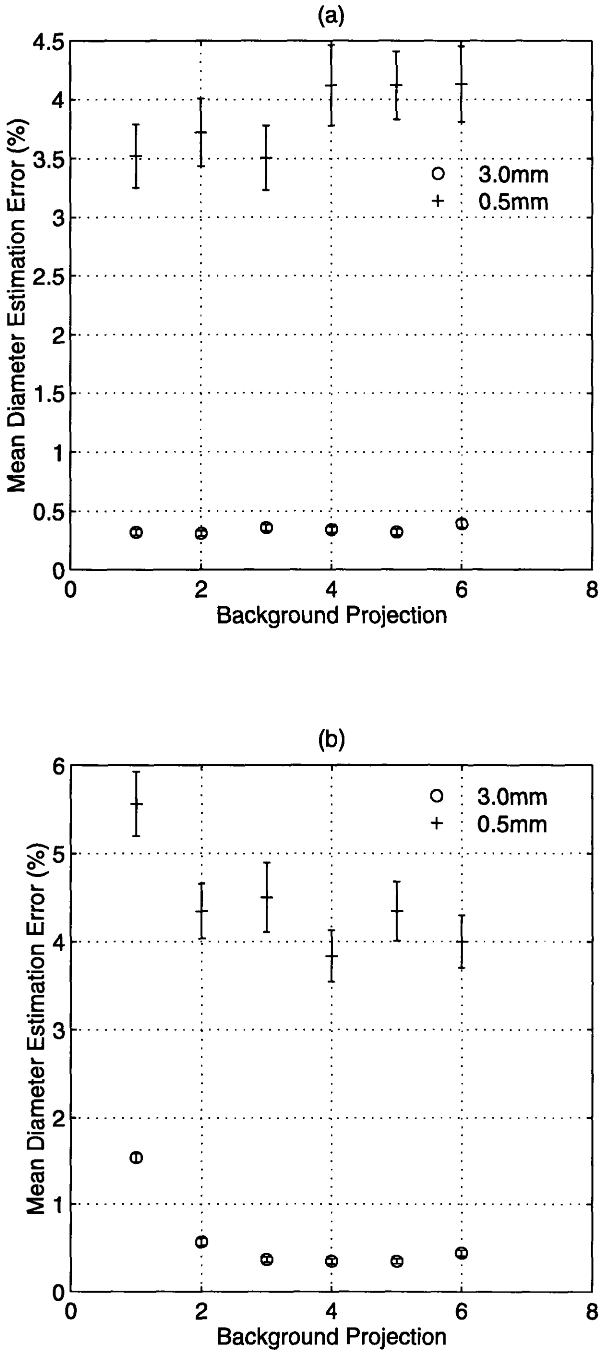

Figure 4-32: Diameter estimation performance in 3.0mm and 0.5mm diameter vessel images as a function of varying background projection intensity. (a) Diameter measurement results using imaging parameter calibration on a large 5.0mm diameter structure. (b) Diameter measurement results using imaging parameter calibration on a smaller 2.0mm structure.

deviation error bars were also larger for the narrow vessel. Comparison of these data with that obtained using calibration on a 2.0mm structure showed only slight differences; the mean diameter estimation error was slightly higher for both the 3.0mm and 0.5mm diameter vessels, and the measurement variability under each background configuration was similar. There appeared to get greater variability in the estimation performance across background configurations when the 2.0mm calibration dataset was used. It is important to note that while the imaging parameter estimation error can vary over a large range when using a 2.0mm calibration dataset (Figure 4-26), the variations in diameter estimation error from the subsequent vessel measurement step are not very big. It is also significant to note that the IW-MBE estimation quality, under the various background configurations tested, was better than that from W-MBE and DBE, particularly when measuring narrow vessels.

4.7.5 Effect of vessel diameter

Now that we have explored the performance of imaging parameter estimation under varying imaging conditions, it is of interest investigate the quality of vessel estimates for a number of different vessel diameters falling between the small and large extremes of width. These simulation results should reflect the best possible performance improvement of IW-MBE over W-MBE and DBE, that can be expected from the 'end-to-end' two-stage estimation process. A 5.0mm calibration dataset was simulated, using a flat background ($b_0 = -1.0$) and the following modelling parameter values: $\Gamma = 36$, $\mu = 0.3$, $\sigma = 0.2$mm, $c_n = 4.0$mm, and $\Lambda_\nu = 9$. The vessel projections were synthesized using the same modelling parameters with the exception of the parameter, r. The vessel diameters simulated were: 0.4mm, 0.5mm, 0.6mm, 0.8mm, 1.0mm, 2.0mm, and 3.0mm. For the fixed level of noise intensity used ($\Lambda_\nu = 9$), the SNR values for these vessels range from 26.5dB for the 4.0mm vessel, down to -4.8dB for the 0.4mm vessel. As in the earlier calibration experiments, we estimated imaging parameter vectors from 100 noisy realizations of the 5.0mm calibration datasets, which were then used to measure diameters from 100 noisy intensity profiles for each of the simulated arterial sizes. The initialization of IW-MBE and W-MBE in this experiment was performed as described in earlier simulations.

Figure 4-33 compares the diameter estimation results from the 'end-to-end' application of IW-MBE, W-MBE, and DBE. Figure 4-34 is an expanded view of the results which focuses on values of mean and standard deviation lying between 0% and 40%. Overall,

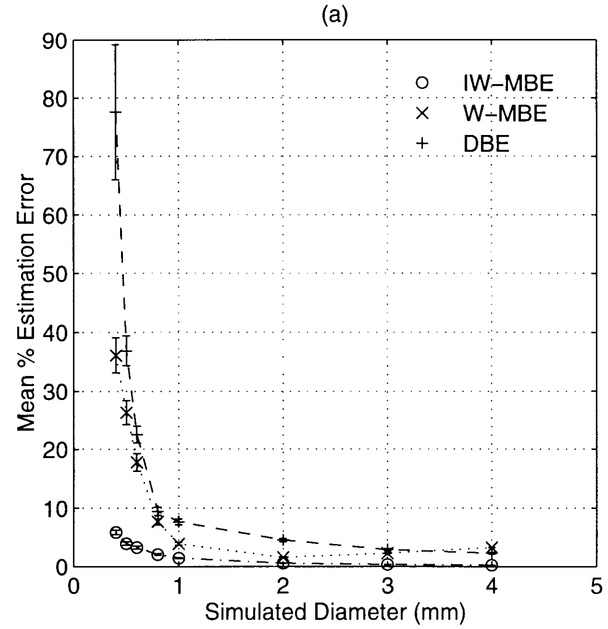

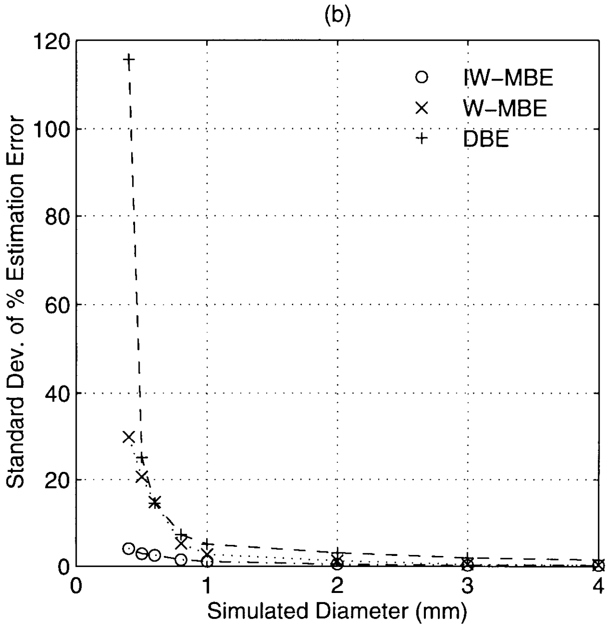

Figure 4-33: Diameter estimation performance as a function of varying vessel diameter and constant noise intensity. Both the system imaging parameter vector and vessel parameter vector were unknowns in these simulations. (a) Mean normalized diameter estimation error as a function of vessel size. The error bars represent the size of one standard deviation in the measures. (b) Standard deviation of the normalized measurement error.

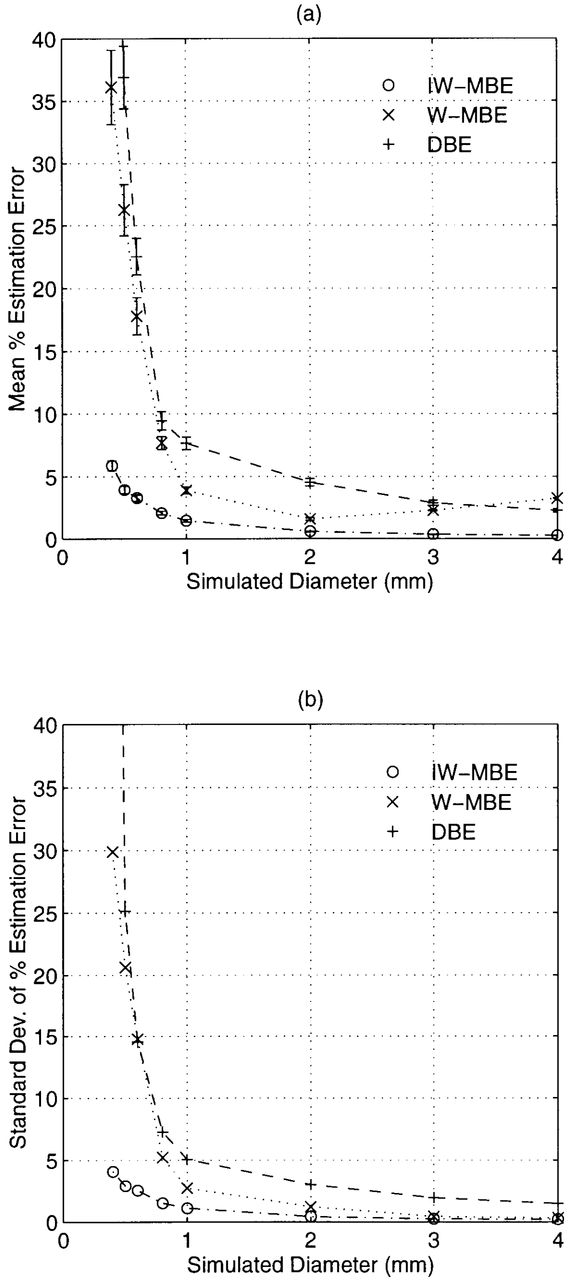

Figure 4-34: Close-up view of Figure 4-33 to show greater detail in the results: (a) Mean normalized diameter estimation error The error bars represent the size of one standard deviation in the measures. (b) Standard deviation of the normalized errors.

these simulation results show marked improved in estimation bias and variability over both W-MBE and DBE, especially for the critical range of vessel diameters smaller than 1.0mm. The means and standard deviations of the estimation error for 'end-to-end' IW-MBE were very similar to those observed in our earlier simulations which assumed known imaging parameter values. This is probably attributable to the very high quality of the imaging parameter estimates that is possible with calibration on a large 5.0mm diameter structure. Focusing on the results for the narrowest simulated vessel (with a diameter of 0.4mm), the observed bias was almost 5 times smaller than that from W-MBE, and about 10 times lower than that from DBE. For this vessel size, the standard deviation of the estimates from IW-MBE was also significantly smaller: almost 4 times lower than that of W-MBE and roughly 15 times lower than that of DBE.

4.7.6 Remarks

These 'end-to-end' investigation indicate that model-based estimation combining information from profile intensity and width leads to robust vessel diameter estimates even when the actual imaging parameters are unknown to begin with. This is an important result since the imaging parameters are not known *a priori* for a typical clinical environment, and are also variable over the course of an angiographic session. The vessel diameter estimation error also appears to be relatively insensitive to changes in imaging noise, background configuration, imaging operating points and initialization points. The most significant simulation result is that IW-MBE is a dramatic improvement over the W-MBE and DBE methods, particularly in the range of small vessel widths which cannot currently be measured reliably. These results are however from simulated experiments. We must now test this new diameter estimator in actual x-ray images of structures whose characteristics are similar to *in vivo* coronary arteries, and whose dimensions are known *a priori.* We will compare the performance of IW-MBE, W-MBE, and DBE on real x-ray images, which typify those obtained clinically, in the following section.

4.8 Assessment of IW-MBE using x-ray ciné-images

4.8.1 Experimental Overview

Since it is not currently possible to determine *a priori* the true diameter of a coronary

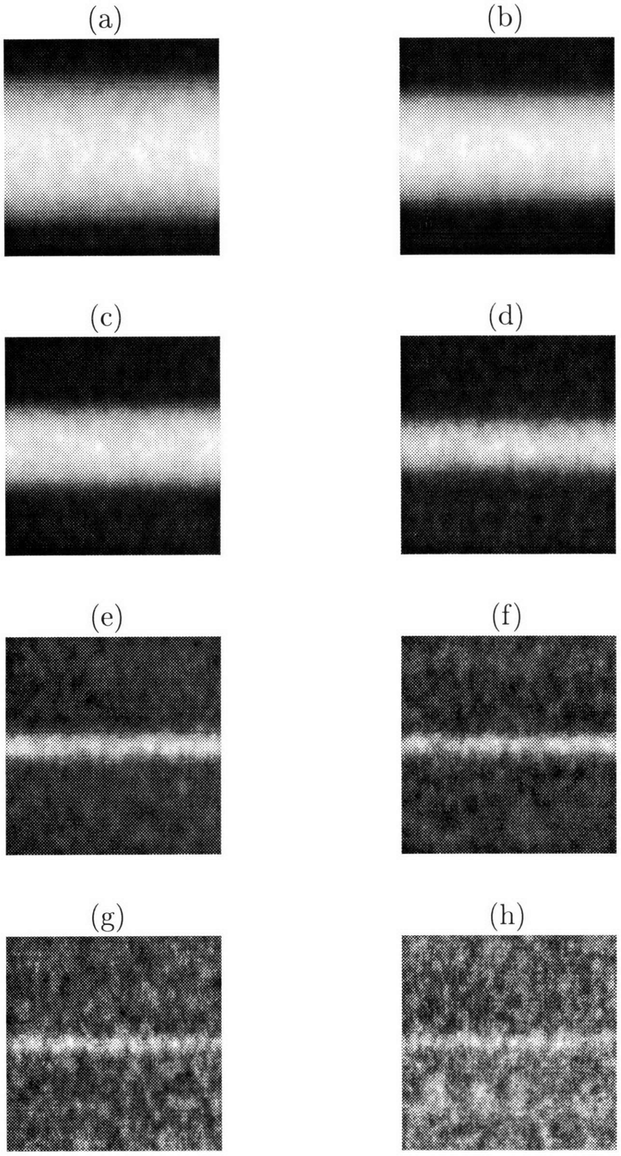

Figure 4-35: X-ray images of contrast-filled vessel phantoms with the corresponding diameters: (a) 5.0mm, (b) 4.0mm, (c) 3.0mm, (d) 2.0mm, (e) 1.0mm, (f) 0.8mm, (g) 0.6mm and (h) 0.4mm. Intensities in each image were scaled so that the entire colormap from [0-255] was used.

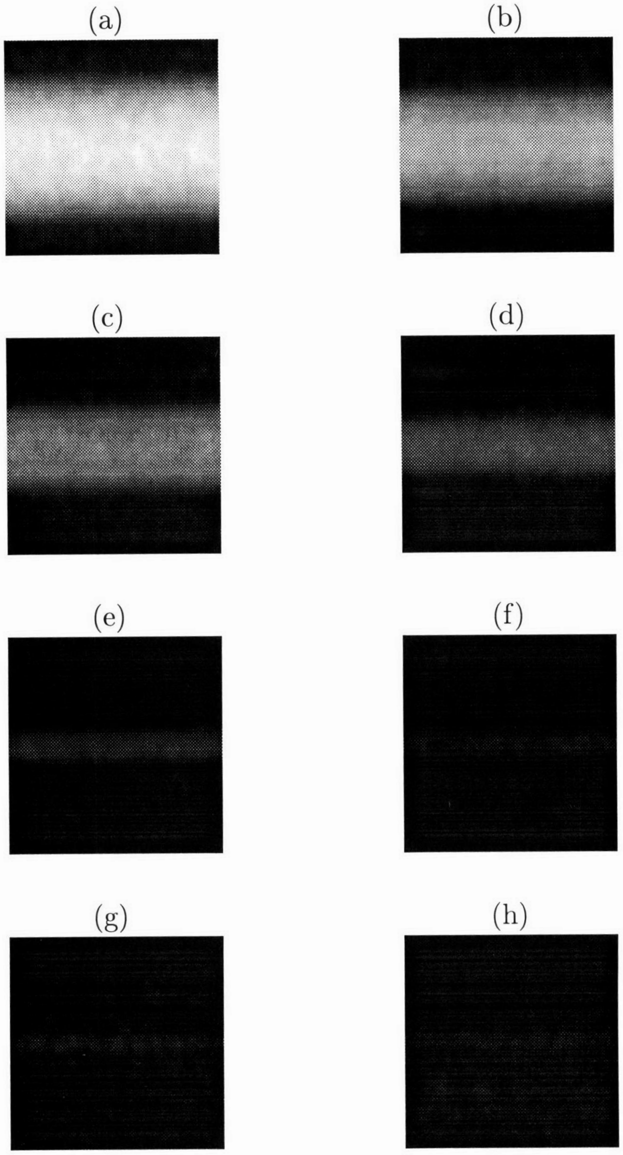

Figure 4-36: X-ray images of contrast-filled vessel phantoms with the corresponding diameters: (a) 5.0mm, (b) 4.0mm, (c) 3.0mm, (d) 2.0mm, (e) 1.0mm, (f) 0.8mm, (g) 0.6mm and (h) 0.4mm. Image intensities in this figure share the colormap used for the 5.0mm diameter vessel image was used.

artery that appears in an x-ray angiogram, vessel phantoms with known cross-sectional diameter are used instead. The vessel phantom used in our investigations consisted of cylindrical bores of known diameter drilled into a lucite block (lucite is relatively transparent to x-rays). These bores were filled with contrast medium and placed over a homogeneous x-ray attenuator which has comparable, though constant, attenuation over the x-ray field, to the average attenuation produced by a human chest. Angiographic filming of these contrast-filled bores over the homogeneous attenuator results in x-ray images which are similar to coronary angiograms. While phantom images have the distinct advantage of possessing 'vessel' diameters that are already known prior to quantitative analysis, the imaging conditions (adjusted automatically by the imaging system equipment) are usually slightly more benign than coronary angiograms in terms of the imaging noise and background.

The phantom diameters used in this study were: 5.0mm, 4.0mm, 3.0mm, 2.0mm, 1.0mm, 0.8mm, 0.6mm, and 0.4mm. The phantom ciné-film frames were projected using a Sony SME-3500 ciné-projector under 4 times optical magnification, and a user-defined region of interest was captured using an Epix framegrabber (quantization at 8 bits/pixel) with a spatial resolution of 0.037 pixels/mm. The resulting vessel phantom images were sampled along their centerlines to produce the 'vessel' data shown in Figures 4-35 and 4-36. The initialization of the calibration and vessel measurement steps was performed in the same manner as in our simulation experiments. Calibration was performed on the noisy 5.0mm diameter dataset. The resulting imaging parameter estimates were then used to estimate vessel diameters in 100 consecutive noisy intensity profiles from the other 7 phantom images (whose SNRs ranged from approximately 32dB for the 4.0mm diameter phantom, down to about -1dB for the 0.4mm vessel). A fifth-degree background polynomial was used in the estimation of the vessel background parameters.

4.8.2 Results

The diameter estimation performance of IW-MBE compared against that for W-MBE and DBE are shown in Figure 4-37. Figure 4-38 shows a close-up view of the estimation performance in vessels 1.0mm in diameter and smaller. For the radiographic and background conditions that were present in the image data, it is apparent that for larger vessels i.e. those greater than 1.0mm in diameter, IW-MBE produced the lowest overall diameter estimation bias and variability when compared against W-MBE and DBE results for the same set

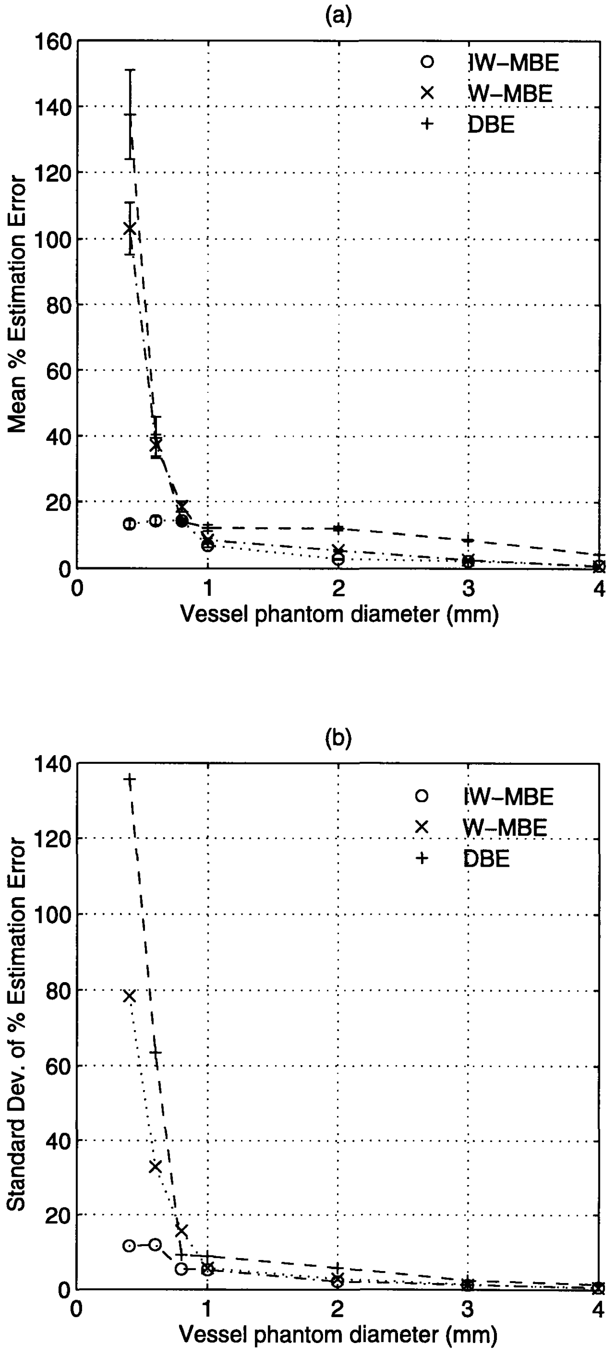

Figure 4-37: Diameter estimation performance in actual x-ray images of the contrast-filled vessel phantoms shown in Figure 4-35. The imaging system parameters and vessel parameters are unknown in this clinically realistic situation. SNR values ranged from about -1dB for the 0.4mm diameter phantom to 32dB for the 4.0mm diameter phantom. (a) Mean normalized diameter estimation error as a function of vessel phantom size. The error bars represent the size of one standard deviation in the measures. (b) Standard deviation of the normalized measurement error.

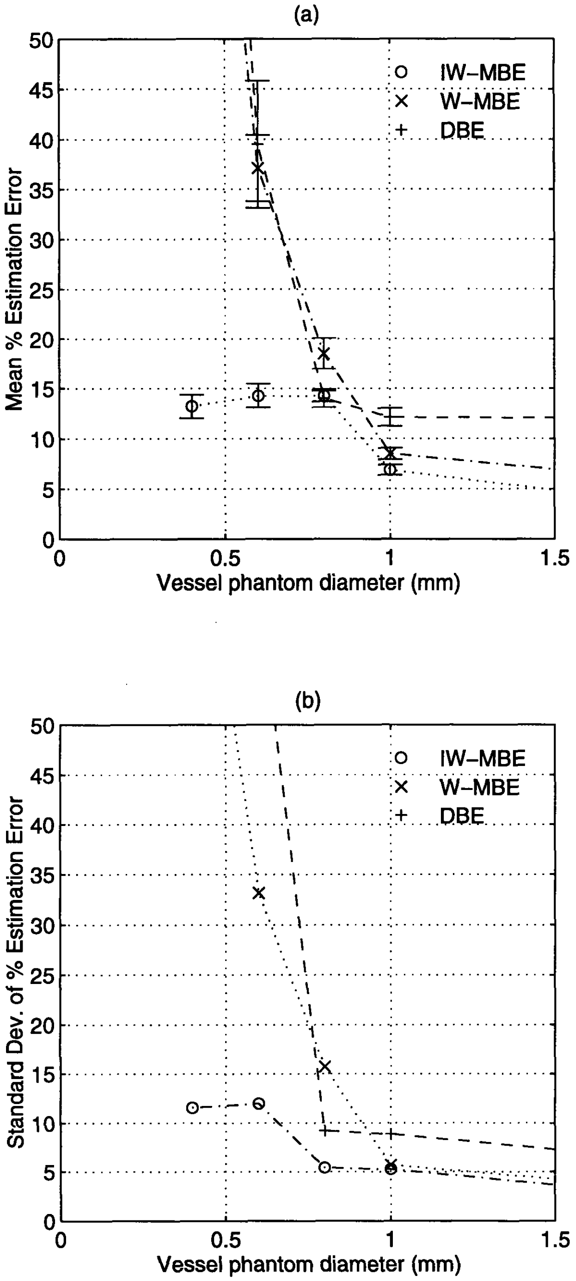

Figure 4-38: Close-up view of Figure 4-37 to show greater detail in the small vessel estimates (diameters $\leq$ 1.0mm): (a) Mean normalized diameter estimation error. The error bars represent the size of one standard deviation in the measures. (b) Standard deviation of the normalized errors.

of data. The estimation bias and variability was smallest for IW-MBE, then W-MBE, followed by DBE. The normalized errors observed from the measurement of these larger vessel phantoms were smaller for the model-based techniques (mean estimation errors were much lower than 10%) than for derivative-based diameter measurement (mean estimation errors reaching almost 13%). These gains were modest, however, since IW-MBE, W-MBE and DBE perform well for large vessel diameters.

In small vessels (i.e. diameters $\leq$ 1.0mm), the gains are significant. Focusing on the small vessel measurement results in Figure 4-38, we see that for the 1.0mm diameter phantom, the mean and standard deviation of the estimation error for IW-MBE were half that for DBE. The IW-MBE results were comparable with those from W-MBE for this vessel size. For vessel diameters much smaller than 1.0mm, the errors from W-MBE and DBE escalate sharply to error values over 100%, whereas those from IW-MBE level off at approximately 14%.

An interesting observation is that for the 0.8mm diameter phantom, the DBE estimates are better than those from W-MBE. Our results suggest that while the estimation performance for derivative-based estimation does not change much between 1.0mm and 0.8mm, the performance of W-MBE is quite sensitive to this diameter change. In fact, for this particular vessel size, the quality of the W-MBE estimates was the poorest of the three estimators implemented, followed by DBE, and then by IW-MBE, which showed similar estimation bias to that of DBE, but only about half the standard deviation (which means that the IW-MBE measurement variability was the lowest of the three). Unlike in the case of the 0.8mm diameter phantom, the W-MBE estimates in the 0.4mm and 0.6mm 'vessels' were better than those from DBE in terms of bias and variability (possibly resulting from the more rapid degradation of DBE performance, when compared against that of W-MBE, as vessel diameter decreases from 0.8mm down to 0.6mm). Without more phantom data for diameters around 0.8mm, it is difficult to explain exactly why DBE estimates are better than those for W-MBE for the 0.8mm vessel, and then return to being worse relative to W-MBE for smaller diameters.

In the 0.4mm and 0.6mm phantoms, the IW-MBE measurements were significantly better than those from both W-MBE and DBE. The mean normalized error for IW-MBE was approximately 14% for these phantom diameters, while the standard deviation of the errors was about 12% for both 'vessels'. The W-MBE mean error in the 0.4mm 'vessel' of 103%

was about 7 times larger than that for IW-MBE, while the W-MBE error standard deviation of 79% was about 5 times larger. The DBE mean error of 138% and error standard deviation of 136% were roughly 10 times higher than the corresponding values for IW-MBE in the 0.4mm phantom. These remarkable performance improvements by IW-MBE over W-MBE and DBE are similar in magnitude to those observed from our earlier simulation results. Interestingly, not only are the improvements similar between our simulations and our investigations in actual x-ray data, but the magnitudes of the errors are also quantitatively comparable. This suggests that our synthetic datasets are similar to real x-ray vessel phantom images, at least in terms of capturing the image characteristics that are important for the problem of QCA.

4.8.3 Remarks

The measurements from real x-ray ciné-images validate our earlier findings based on Monte-Carlo simulation. These results demonstrate that it is indeed possible to use actual x-ray images to estimate an unknown set of imaging parameters, which can then be used to exploit vessel profile intensity as an additional source of vessel diameter information. By taking advantage of both profile intensity and width, it appears that the estimation quality that is possible for narrow vessel diameters is several fold better than existing model-based and derivative-based methods. The magnitude of this improvement is such that reliable estimates of vessel diameters narrower than 1.0mm may now be possible where they were not prior to this work. While our simulations and vessel phantom results have established that this approach to diameter estimation can work, we recognize the limitations of computer modelling, and the limitations of imaging a simple arterial phantom over a homogeneous attenuator. Further testing of IW-MBE using a more exhaustive x-ray image dataset spanning the range of clinically relevant x-ray conditions is the logical next step.

Chapter 5

Conclusions and Future Work

5.1 Conclusions

In this thesis we developed a new model-based method for accurately and reliably estimating vessel diameter that outperforms existing estimators, particularly for narrow vessel widths which are typical of clinically significant stenoses. In characterizing the performance of this new estimator, we focused on non-branching, non-overlapping arterial segments with circular lumen, and which lay parallel to the imaging plane. These are the same criteria currently used for determining the eligibility of vessel segments for clinical evaluation using QCA.

We began with an analysis of the derivative-based diameter estimator and the width-dependent model-based estimator to gain insight into why they fail to accurately quantify narrow vessel diameters. We found that these existing techniques rely on the apparent vessel profile width as their source of information about the real vessel diameter. Because of the imaging blur and noise that are typical of coronary angiograms however, the apparent width of narrow profiles contains little information about the true vessel diameter. In our observations, we made a significant finding that there is a non-linear relationship between the intensity profile height and the true vessel diameter, and that this profile height/intensity remains sensitive to changes in vessel diameter smaller than 1.0mm. We recognized that this intensity relation could be exploited as an additional source of vessel diameter information which may potentially improve the quality of QCA measurements. However to date, this intensity relationship could only have been determined experimentally, using additional x-ray procedures which are clinically impractical to perform.

Taking advantage of existing parametric models describing the behavior of individual angiographic imaging components, we developed a model-based estimation procedure for determining the non-linear intensity function, which makes use of a structure (of known shape and size, e.g. a cardiac catheter or a large diameter circular vessel) that already exists within an angiographic image frame. Estimation of the unknown imaging model parameters directly from an angiogram entirely eliminates the need for separate x-ray experiments, making it a clinically feasible option.

Our work culminated in the novel intensity- and width-dependent model-based estimator (IW-MBE) which was implemented in two-stages. The first stage was the imaging parameter estima0tion step in which the unknown imaging parameter were determined. These estimates were then input into the second stage which estimated the unknown diameter associated with a vessel intensity profile of interest. In our implementation of these steps, the maximum-likelihood parameter estimates were obtained iteratively using the Nelder-Mead numerical algorithm for function minimization.

We tested IW-MBE against a derivative-based diameter estimator (DBE), and a width-dependent model-based estimator (W-MBE), under a variety of imaging conditions using Monte-Carlo computer simulations. We also tested the performance of these algorithms in real x-ray images of vessel phantoms. Our results from these investigations showed that particularly in vessels smaller than 1.0mm, IW-MBE performance is significantly better than that of DBE and W-MBE, in terms of both the normalized mean error magnitude and normalized standard deviation of the error magnitude. The bias and variability were in fact found to be several factors smaller for IW-MBE than for DBE or W-MBE in the narrowest vessel diameters examined. Both the imaging parameter estimation procedure and the vessel diameter estimation step appear to be robust to a variety of imaging noise conditions, angiographic backgrounds, and imaging system operating points. The performance improvement observed from using IW-MBE can be attributed to that fact that it truly uses all the information contained within the intensity and the width of a projection profile to estimate the unknown model parameters.

In addition to these findings, we have observed that the estimation error magnitudes from our simulations, and those from the real x-ray images are similar. This suggests that our synthetic image data captures the salient characteristics of real x-ray image data sets. This in turn points to the potential applicability of the image synthesis model in answering other related questions in x-ray angiography.

The results from our simulation and phantom data are certainly very encouraging. There are of course limitations to computer modelling, and to using x-ray image data based on a simple arterial phantom placed over a homogeneous attenuator (though this is currently the standard way for evaluating the performance of any diameter estimator). The use of a more exhaustive x-ray image dataset spanning a wider range of clinically relevant x-ray conditions, and testing on x-ray coronary angiograms from human subjects will be necessary next steps. The improvements in diameter measurement that appear to be possible using IW-MBE will in turn improve the quality of other physiological parameters based on this quantity. Furthermore, the robustness to noise that this approach possesses may indicate that lower x-ray dosage requirements for clinical angiographic procedures can be used, which will decease patient x-ray exposure. The higher estimation quality that is possible in small vessels as well as large ones will also benefit CAD intervention trials based upon QCA results.

5.2 Future Work

The most obvious direction for future work would be the testing of IW-MBE on x-ray coronary angiograms. While the real diameter of an *in vivo* coronary vessel cannot be determined exactly, the relative measures from IW-MBE versus W-MBE and DBE may be useful. Alternatively, an animal model may be used. In this case, vessel phantoms of known diameter may be implanted into the thorax and subsequently imaged. This has the benefit of providing a more realistic chest image and 'vessel' structures that are of known size.

Another issue that should be explored is the expansion of the vessel subset that we consider. This would require the extension of our model so that multiple angiographic projections (such as those from bi-plane imaging) can be used to reconstruct non-circular vessel lumen, as well as those that branch or overlap with other vessels. This extension would also allow quantitation of vessels lying non-coplanar with the imaging plane.

Yet another direction to explore is the incorporation of information from consecutive image frames to improve vessel parameter estimates, as well as to investigate the evolution of these parameters as a function of time. In this work, we have made no effort to combine intensity information from nearby profiles to improve diameter estimation. It is known that vessel diameters, at least locally, are highly correlated, and it should therefore be possible to use this information to achieve diameter smoothing between scanlines. In this manner, the achievable diameter estimation quality may be increased still further.

Finally, the concept of model-based estimation may be extended to the quantification of arterial lesion lengths. Existing methods for this are ad-hoc and edge-based algorithms (not unlike the prevailing method of diameter estimation). A healthy vessel segment may be modelled as a linearly tapering cylinder, whereas a diseased vessel will deviate from this model. Using change detection theory to analyze the error between the diameter predicted by the 'healthy' model and the actual vessel diameter observation, it will be possible to identify points on the arterial segment where significant deviations indicative of disease occur. In this manner, we should be able to detect the transition points associated with the two lesion boundaries in a vessel segment containing a single concentric stenosis.

Bibliography

[1] N. Alperin, K.R. Hoffmann, K. Doi, and K.G. Chua. Automated analysis of coronary lesions from cineangiograms using vessel tracking and iterative deconvolution techniques. *IEEE Conference Proceedings: Computers in Cardiology*, pages 153–156, 1990.

[2] Y. Bresler and A. Macovski. Estimation of 3D shape of blood vessels from x-ray images. *SPIE Conference Proceedings: Medical Images and Icons*, 515:251–258, 1984.

[3] M.J. Davies. *Advances in Quantitative Coronary Arteriography*, chapter 1, pages 3–14. Kluwer Academic Publishers, 1993.

[4] E.R. Griffith, J.B. Stonebridge, D. Piernak, and J.F. Lehman. Development of a method of x-ray densitometry for bone mineral measurement. *Amer. J. Phys. Med.*, 52:128, 1973.

[5] Y. Han, W.E. Snyder, and D.M. Herrington. Quantitative angiography: Densitometry guided edge detection using mean field annealing. *IEEE Conference Proceedings: Computers in Cardiology*, pages 105–108, 1993.

[6] K. Kitamura, J.M. Tobis, and J. Sklansky. Estimating the 3D skeletons and transverse areas of coronary arteries from biplane angiograms. *IEEE Transactions on Medical Imaging*, 7(3):173–187, 1988.

[7] W. Leung, W. Sanders, and E. Alderman. Coronary artery quantitation and data management system for paired cineangiograms. *Catheterization and Cardiovascular Diagnosis*, 24:121–134, 1991.

[8] J.S. Lim. *Two-dimensional signal and image processing.* Prentice Hall, 1990.

[9] T. Pappas. *Estimation of Coronary Artery Dimensions from Angiograms.* PhD thesis, Massachusetts Institute of Technology, 1987.

[10] T. Pappas and J.S. Lim. A new method for estimation of coronary artery dimensions in angiograms. *IEEE Transactions on Acoustics, Speech, and Signal Processing*, 36(9):1501–1513, 1988.

[11] J.H.C. Reiber. An overview of morphologic and densitometric approaches for the quantitation of coronary stenoses. *Automedica*, 10:171–200, 1989.

[12] J.H.C. Reiber, C.J. Kooijman, C.J. Slager, J.J. Gerbrands, J.C.H. Schuurbiers, A. den Boer, W. Wijns, P.W. Serruys, and P.G. Hugenholtz. Coronary artery dimensions from cineangiograms – methodology and validation of a computer-assisted analysis procedure. *IEEE Transactions on Medical Imaging*, MI-3(3):131–141, 1984.

[13] J.H.C. Reiber, C.J. Slager, J.C.H. Schuurbiers, J.J. den Boer, A.and Gerbrands, G.J. Troost, B. Scholts, C.J. Kooijman, and P.W. Serruys. Transfer functions of the x-ray-cine-video chain applied to digital processing of coronary cineangiograms. In P.H. Heintzen and R. Brennecke, editors, *Digital Imaging in Cardiovascular Radiology*, pages 89–104, Stuttgart, 1983. Georg Thieme Verlag.

[14] J.L. Ritchie, M.D. Cheitlin, M.A. Hlatky, T.J. Ryan, and R.G. Williams. Task force 5: Profile of the cardiovascular specialist: Trends in needs and supply and implications for the future. *Journal of the American College of Cardiologists*, 24(2):313–321, 1994.

[15] Ying S. Automated identification of vessel contours in coronary arteriograms by an adaptive tracking algorithm. *IEEE Transactions on Medical Imaging*, 8(1):78–88, 1989.

[16] K. Shmueli, W.R. Brody, and A. Macovski. Estimation of blood vessel boundaries in x-ray images. *Optical Engineering*, 22(1):110–116, 1983.

[17] M. Sonka, G. Reddy, M. Winniford, and S. Collins. Adaptive simultaneous coronary border detection: A method for accurate analysis of small diameter vessels. *IEEE Conference Proceedings: Computers in Cardiology*, pages 109–112, 1993.

[18] J.R. Spears. Rotating step-wedge technique for extraction of luminal cross-sectional area information from single plane coronary cineangiograms. *Acta Radiologica Diagnosis*, 22:217–225, 1981.

[19] S. Webb, editor. *The Physics of Medical Imaging.* Institute of Physics Publishing, 1992.